REPORT ONR-CR212-225-3

FURTHER STUDIES OF AERODYNAMIC LOADS
AT SPIN ENTRY

SELDEN B. SPANGLER
MICHAEL R. MENDENHALL

NIELSEN ENGINEERING & RESEARCH, INC.
MOUNTAIN VIEW, CALIFORNIA 94043

D D C
DEC 22 1977
F.

CONTRACT N00014-74-C-0344
ONR TASK 212-225

30 JUNE 1977

ANNUAL TECHNICAL REPORT FOR PERIOD I MAY 1976 TO I MAY 1977

APPROVED FOR PUBLIC RELEASE; DISTRIBUTION UNLIMITED

PREPARED FOR THE

OFFICE OF NAVAL RESEARCH ●800 N. QUINCY ST.●ARLINGTON●VA●22217

Change of Address

Organizations receiving reports on the initial distribution list should confirm correct address. This list is located at the end of the report. Any change of address or distribution should be conveyed to the Office of Naval Research, Code 211, Arlington, Virginia 22217.

Disposition

When this report is no longer needed, it may be transmitted to other authorized organizations. Do not return it to the originator or the monitoring office.

Disclaimer

The findings in this report are not to be construed as an official Department of Defense or Military Department position unless so designated by other official documents.

Reproduction

Reproduction in whole or in part is permitted for any purpose of the United States Government.

COPY NO. 18

Unclassified

REPORT DOCUMENTATION PAGE		READ INSTRUCTIONS BEFORE COMPLETING FORM
1. REPORT NUMBER ONR-CR212-225-3	2. GOVT ACCESSION NO.	3. RECIPIENT'S CATALOG NUMBER
4. TITLE (and Subtitle) FURTHER STUDIES OF AERODYNAMIC LOADS AT SPIN ENTRY.		5. TYPE OF REPORT & PERIOD COVERED Annual Report. 1 May 1976 to 1 May 1977
		6. PERFORMING ORG. REPORT NUMBER NEAR-TR-141
7. AUTHOR(s) S. B. Spangler and M. R. Mendenhall		8. CONTRACT OR GRANT NUMBER(s) N00014-74-C-0344
9. PERFORMING ORGANIZATION NAME AND ADDRESS Nielsen Engineering & Research, Inc. 510 Clyde Avenue Mountain View, CA 94043		10. PROGRAM ELEMENT, PROJECT, TASK AREA & WORK UNIT NUMBERS 62241N RF41-411-801,2-30 1411-801
11. CONTROLLING OFFICE NAME AND ADDRESS Office of Naval Research 800 North Quincy Street Arlington, VA. 22217 Attn: Code 211		12. REPORT DATE 30 June 1977
		13. NUMBER OF PAGES 156
14. MONITORING AGENCY NAME & ADDRESS(if different from Controlling Office)		15. SECURITY CLASS. (of this report) Unclassified
		15a. DECLASSIFICATION/DOWNGRADING SCHEDULE

16. DISTRIBUTION STATEMENT (of this Report)

Approved for public release; distribution unlimited

17. DISTRIBUTION STATEMENT (of the abstract entered in Block 20, if different from Report)

18. SUPPLEMENTARY NOTES

19. KEY WORDS (Continue on reverse side if necessary and identify by block number)

Aerodynamic Loads
Asymmetric Vortex Shedding
High Angle of Attack
Spin Entry

20. ABSTRACT (Continue on reverse side if necessary and identify by block number)

As part of a continuing investigation of the aerodynamic loads on a fighter-bomber aircraft at spin departure, a coordinated analytical and experimental program was undertaken on vortex shedding from noncircular nose shapes. The asymmetric loads induced by nose vortex shedding at zero and nonzero sideslip are a primary cause for adverse handling qualities at high angles of attack.

DD _{1 JAN 73} FORM 1473   EDITION OF 1 NOV 69 IS OBSOLETE

Block No. 20 (concluded)

A theoretical analysis for vortex shedding from noncircular nose shapes at combined angles of attack and sideslip was developed. Boundary layer separation is predicted in order to determine the rate of shedding of vorticity. Comparisons with separation data on two dimensional cylinders and with measured loads and flow field velocities in the wake for inclined ogive-cylinders give reasonable agreement.

Tests were conducted in the V/STOL tunnel at NASA Langley Research Center and the Nielsen Engineering & Research water tunnel on a fighter model and typical fighter nose shapes. The NASA data include simultaneous wake velocity and load measurements, and the Nielsen data include simultaneous vortex position and load measurements. Preliminary comparisons with the vortex shedding theory give reasonable agreement in most cases.
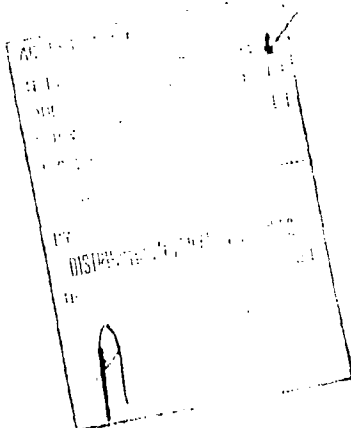
PREFACE

This technical report covers the work performed under Contract N00014-74-C-0344 from 1 May 1976 through 1 May 1977 and is the third report published under the program. Significant cooperation was furnished by the Langley Research Center, NASA in conducting a test program.

CDR P. R. (Bob) Hite and Mr. David S. Siegel, Office of Naval Research, were the Navy Scientific Officers.

1

TABLE OF CONTENTS

TABLE OF CONTENTS (CONCLUDED)

LIST OF ILLUSTRATIONS

LIST OF ILLUSTRATIONS (CONTINUED)

LIST OF ILLUSTRATIONS (CONTINUED)

8

LIST OF ILLUSTRATIONS (CONCLUDED)

LIST OF TABLES

FURTHER STUDIES OF AERODYNAMIC LOADS
AT SPIN ENTRY

by S. B. Spangler and
M. R. Mendenhall
Nielsen Engineering & Research, Inc.

1. INTRODUCTION

A program is being conducted by Nielsen Engineering & Research, Inc. (NEAR) for the Office of Naval Research to develop techniques for predicting the aerodynamic load distribution on a fighter-bomber type aircraft at incipient spin entry flight conditions. The problem considered is one in which the aircraft is in the range of angle of attack (generally 30° to 45°) in which flow separation occurs on the nose and a steady asymmetric vortex system is formed. The vortices induce a side force on the nose and pass over the wing and tail to induce a side force and rolling moment on these components. This vortex system is an important source of lateral aerodynamic effects causing spin departure for many aircraft, which can occur even at zero sideslip.

The general approach to an analytical description of the flow and the induced forces and moments is to characterize the separated flow region over the nose in terms of potential vortex filaments whose strength and position over the nose can be calculated. These filaments pass over the wing, body, and tail and induce further yawing and rolling moments. Classical wing-body-tail vortex inteference methods can be used to compute the positions of the vortex filaments aft of the nose and the vortex-induced loads. For greater flexibility and accuracy, a vortex-lattice lifting-surface program was developed which computes the asymmetric load distribution induced on the wing-body by the nose vortices.

In the first two years of the program, the work has been primarily analytical. Methods were developed to predict the asymmetric vortex shedding from a circular cross section nose and to follow these vortices aft over the wing/strake/body/tail to calculate their interference on these aircraft components. The methods involve a vortex-lattice program capable of treating asymmetric induced flows, slender-body methods for tracking the vortices over the aircraft, and body-tail interference methods for calculating vortex-induced loads on the tail and afterbody. The vortex-lattice program was subsequently modified to handle sideslip. This work is reported in references 1 and 2.

11

It was apparent in applying these methods to real aircraft that it would be necessary to consider more realistic nose shapes, since it was clear that tailoring the shape of the nose can improve the aerodynamic characteristics at high angles of attack. Since very little work has been done on vortex shedding from noncircular noses, a combined experimental and analytical program was formulated in the third year. The experiments involved tests in the V/STOL tunnel at Langley Research Center and in the NEAR water tunnel. The analytical work involved development of a vortex shedding analysis for noncircular nose shapes, including the effects of boundary layer separation prediction. This work is summarized in this report. The report takes the form of three sections describing the work and results and a final section discussing and comparing the results.

2. NASA TEST PROGRAM

The Langley Research Center of NASA has done a great deal of work on spin dynamics and aerodynamics and has produced some excellent results on many facets of this problem. On the basis of their interest, a joint program between the Dynamic Stability Branch and ONR was established in which an existing NASA model would be tested in the LRC V/STOL tunnel and simultaneous measurements of the loads and flow field would be obtained. Since LRC had no capability to measure flow fields in their tunnel, funds for a probe actuator were provided for these tests by ONR. NEAR designed the test program to provide data suitable for both the present ONR contract and NASA use. This section describes the tests and results.

2.1 Objectives

The principal objective of the program is to obtain simultaneous measurements of both the flow field above the model and the loads on the model for a research configuration having certain essential features of a modern fighter-bomber aircraft, since no such measurements exist (at least in the available literature). Specifically, a configuration exhibiting a noncircular nose and strakes (leading edge extension) was desired. The results were to be obtained at low speeds (no compressibility effects) and at high Reynolds numbers. The data were desired for evaluating a theory on vortex shedding from noncircular cross section, pointed noses at high angles of attack. Thus it was necessary to measure at least two components of velocity over a large enough grid to permit the vorticity field to be well defined.

2.2 Model

The model used is an existing NASA model developed for investigating high lift features on a fighter configuration. The principal characteristics are shown in Figure 1. The body has a pointed nose and a cross section consisting of two circular arcs and straight sides. The wing is a clipped delta planform with a slightly swept forward trailing edge, a taper ratio of 0.228, aspect ratio of 2.5, and a circular arc airfoil section varying from 6 percent thick at the root to 4 percent at the tip. The model is geometrically similar to that described in reference 3 but approximately 2.4 times larger.

The NASA model is designed to have canards, which were not used in these tests. The canard mounts were used to support strakes, as shown by the dashed lines. The strakes have sharp leading edges and uniform
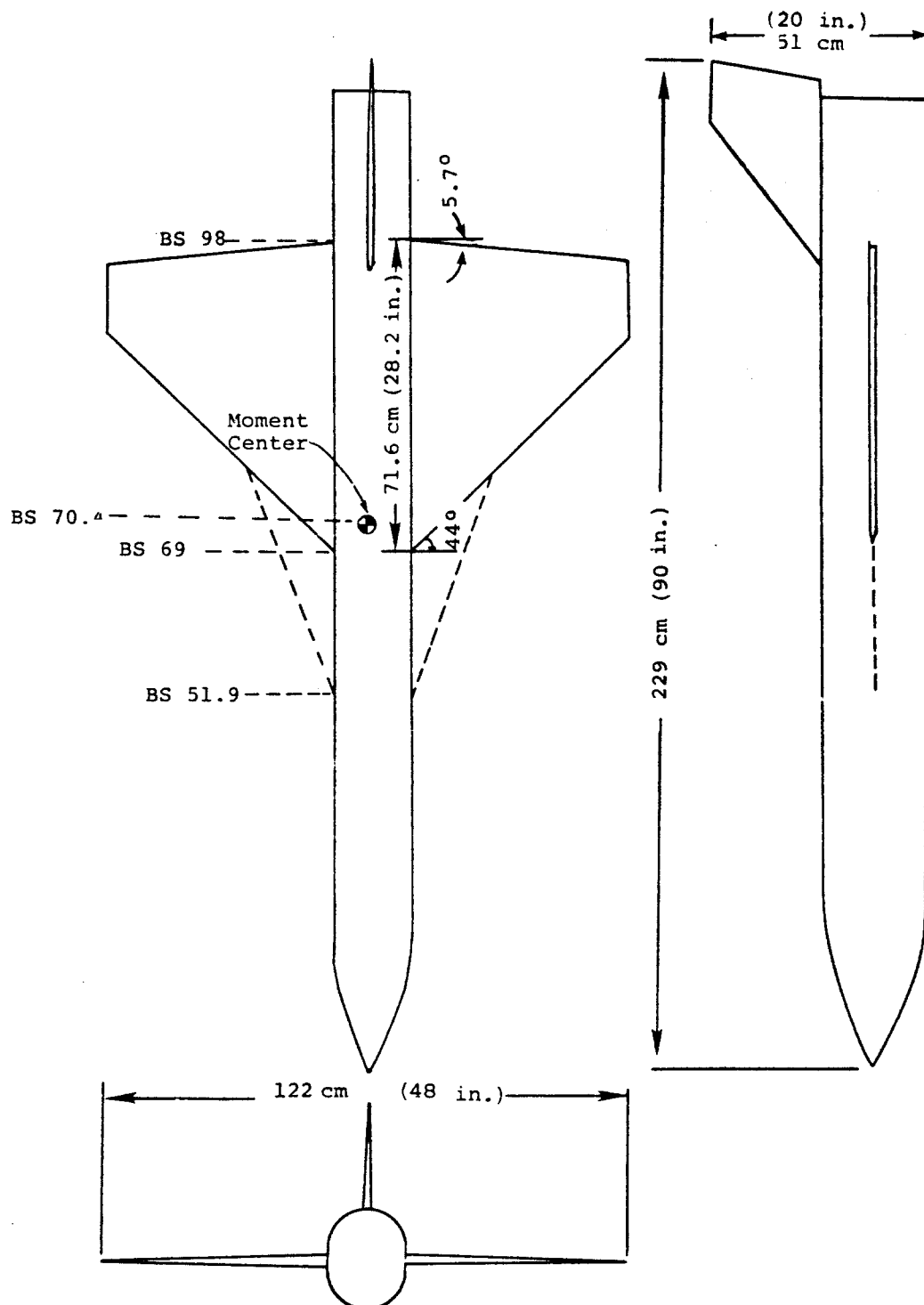
Figure 1.- Langley Research Center V/STOL fighter model.

14

thickness. An internal 6 component strain gage balance is mounted within the body to measure loads.

A seven-probe rake was used to measure the flow field above the body and wing. This rake was mounted on an actuator located on the sting behind the model, as shown in Figure 2. On the hemispherical nose of each probe are located a central hole, four holes 90 degrees apart approximately 45 degrees off the axis of the probe, and a static hole aft on the cylindrical part of the probe, as shown below.

The probes were individually calibrated to measure the magnitude and direction of the onset flow up to flow angles of 60 degrees from the probe axis (or alternately three velocity components; one along and two perpendicular to the probe axis).

The preliminary design of the actuator was done by NEAR, and the actuator was procured by LRC with ONR funds. The actuator is an r, θ type with a remotely actuated drive in angle and a manual setting of radius. Scanivalves were located on the sting just aft of the actuator to record the 42 pressures measured by the probes.

2.3 Test Conditions

The V/STOL tunnel is an atmospheric closed-return tunnel with a maximum speed capability of about 100 m/sec (200 kts). The sting support system has an angle of attack range of about 28° and a translation capability to place the model in the center (vertically) over the angle range. A knuckle was used to obtain an angle of attack range of 12° to 40°.

Force and moment tests were conducted initially over the range from 20° to 40° to find angles of attack at which the forces were repeatable and the nose separation vortex system appeared stable. These tests were conducted at speeds of 19 m/sec and 60 m/sec. Based on these results, angles of attack of 20° and 35° and sideslip angles of 0° and 10° were
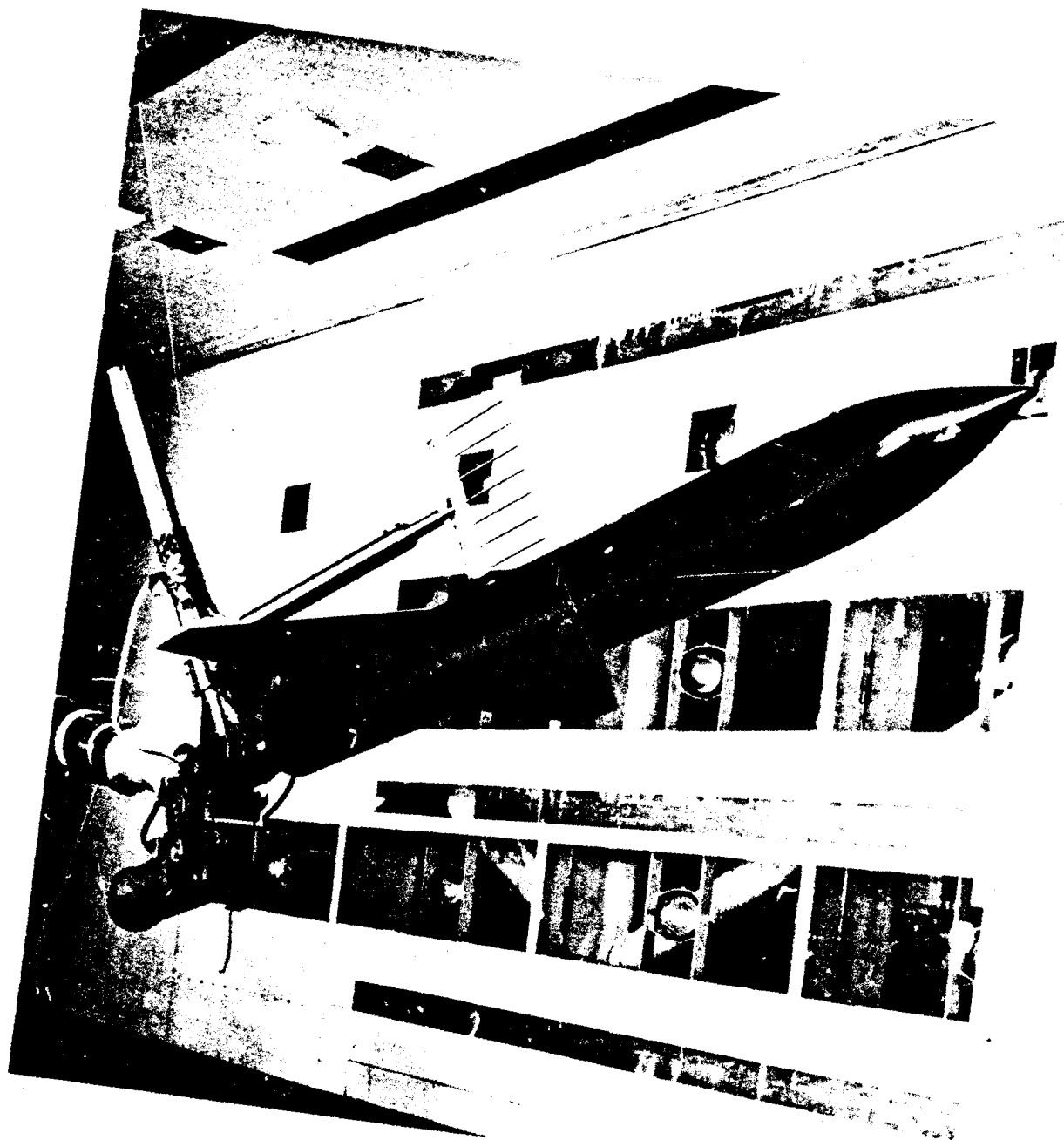
Figure 2.   V/STOL Fighter Model and Rake Mounted
in V/STOL Wind Tunnel.

16

selected for the flow field testing. The 20° case gives a symmetric vortex pattern with little side force and the 35° case gives an asymmetric vortex system with considerable side force. The flow field measurments were all obtained at speeds of about 60 m/sec (200 ft/sec).

In addition to force and moment testing and flow field measurements, some initial testing was done at about 15 m/sec with a helium bubble flow visualization apparatus to attempt to locate the extent of the vortex flow field so the rake apparatus could be located to cover all regions of interest.

2.4 Measurements

The measurements consisted of six components of forces and moments on the body, some photographs of the helium bubble flow, and the flow field measurements. The latter were taken at 3 axial stations, shown on Figure 1. The first, at Body Station BS 51.9, corresponds to the inter-section of the strake leading edge and the body. The second, BS 69, corresponds to the intersection of the basic wing leading edge and the body. The third, BS 98, corresponds to the intersection of the wing trailing edge and the body.

At the two forward stations, the rake was initially set so that the innermost probe was approximately 2.5 cm (1 inch) above the body. The probe was then swept through a ±72 degree arc about the vertical plane. Readings were taken every 3 degrees of arc. The rake was then moved radially outward 2.5 cm (1 inch) and the process repeated. Since the probes are 5 cm (2 inches) apart on the rake, this procedure provided data along arcs every 2.5 cm from 2.5 cm above the body to 32.5 cm above the body.

At the rear station, the process was repeated over a 130 degree of arc. In addition, the probe was moved radially outward to cover a second band ranging from 35 cm to 67.5 cm above the body and ±50 degrees in arc.

It should be noted that the probe measurements turned out to be extremely time consuming. Even though the V/STOL tunnel staff granted three additional days over the 10 originally scheduled for the tests, less than half the data originally anticipated was actually obtained. The NEAR staff engineers received excellent cooperation from NASA in these tests.

2.5 Results

The results of the tests are shown in the figures of Appendix A. There are four sets of results. They are the force and moment results, the influence of the rake on the forces and moments, repeatability of the flow field measurements, and vector plots of the flow field velocities.

The forces and moments with no rake present are shown in Figures A-1 through A-10. The normal force and pitching moment, Figures A-1 and A-2, show relatively little influence of Reynolds number. There is a large increase in normal force when the strakes are added. The center of pressure shifts forward, as would be expected, and changes with angle of attack such that little change in pitching moment occurs with increasing angle. These figures also show the data from reference 3 on a geometrically similar but smaller model and indicate good agreement between the two sets of data.

The side force and yawing moment results for various combinations of strakes off and on and vertical tail off and on are shown in Figures A-3 through A-10. Generally there is a greater influence of Reynolds number on these results, particularly at the higher angles of attack. Since the viscous effects are more important in side force and yawing moment, this is to be expected. Figures A-3 and A-4 show the smaller scale results from reference 3 and indicate reasonably good agreement for side force at the lower angles of attack, but poor agreement at high angles for side force and at all angles for yawing moment. The repeatability tests made throughout this angle of attack range indicated considerable unsteadiness in the forces and moments (and by implication the separation vortex system) in the angle of attack range from about 25 to 32 degrees.

The addition of the strakes to the body-wing with no tail (Figures A-5 and A-6) did not change the magnitudes of the force and moment appreciably but considerably decreased the influence of Reynolds number on the results.

The addition of a vertical tail without strakes (Figures A-7 and A-8) had a large influence on the side force and yawing moment. The Reynolds number effects were considerably greater with the tail on than off. This illustrates the importance of the nose vortex system in influencing the loads on the complete configuration.

18

Finally, the addition of the vertical tail with strakes on (Figures A-9 and A-10) had its most significant effect at low angles of attack. For yawing moment, the addition of the vertical tail (compare Figures A-6 and A-10) had the effect of reversing the sign of the yawing moment at angles of attack above 27 degrees, with a large Reynolds number dependency on some of the results.

The next set of results, Figures A-11 and A-12, show probe interference effects. These are plots of the variation of side force, yawing moment, and rolling moment with rake position angle, with the rake innermost probe located 2.5 cm above the body. Noted on the figures are the values of the forces and moments with the probe not present.

For the forward axial station (Figure A-11), the probe interference is small in a small angle region around 90 degrees (the probe directly on top of the model). The interference loads increase as the probe is moved either direction away from 90 degrees in an antisymmetric fashion, due to the lift interference of the airfoil section supporting the probes (see Figure 2). At the rear station (Figure A-12), the variation of loads from the no-probe values is about half that of the previous case, except for C_n, and does not exhibit the same antisymmetric behavior.

It is not possible to assess the importance of these interference loads on the vortical flow field measurements. The measurements of greatest interest are in a small angle region around 90 degrees where the interference loads are the smallest, and this plus the repeatability of the results, discussed next, lend confidence to the measurements.

The next set of results (Figures A-13 and A-14) show repeatability of the rake velocity measurements at two axial stations. At the forward station (Figure A-13), two sets of the three velocity components are given for a rake angle such that the innermost probes (nos. 6 and 7) are very near the vortex core. The agreement is excellent except for probe no. 7 closest to the vortex, and is quite good at this point. For the rear station (Figure A-14), the innermost probe is 35 cm (14 inches) above the body. The agreement again is very good. These results lend some confidence to the assumptions that the vortex flow over the model is stable and the interference effects of the probe on the flow are not inducing any large instability of the vortical flow.

The final set of results (Figures A-15 through A-30) are velocity vector plots prepared by computer from the probe data. Each figure is identified by model configuration, axial station, and flow condition. The vectors are drawn to scale according to the magnitude of the component in the cross flow plane (normal to the model longitudinal axis), and the axial component is given by the number at the end of each vector. The scale is dimensional, with the top of the body at 4.6 inches.

Figures A-15 through A-18 show results at the most forward axial station. For 20 degrees angle of attack (Figures A-15 and A-16), the vortex cores are very close to the body and are not well defined. At 35 degrees angle of attack (Figures A-17 and A-18), the vortex cores are further out than the first row of probe data and are reasonably well defined. One can note the asymmetry at zero sideslip (Figure A-18) from the directions of the velocity vectors along the vertical axis. Although with the reduction in the figures, it is difficult to read the axial velocity magnitudes, it is characteristic of the vortices at 35 degrees that a high axial velocity exists in the core region. Values as high as 82 m/sec (268 ft/sec) occur near the core, whereas the typical values away from the core are 49 (160) to 55 m/sec (180 ft/sec). The vortices tend to resemble a classical concentrated vortex pair.

At the next aft station (Figures A-19 through A-22), a similar pattern exists at 20 degrees angle of attack as occurred at the more forward station at 35 degrees, except the vortex pattern is symmetric (see Figure A-21 in particular). At 35 degrees angle of attack (Figures A-19 and A-20), the vorticity is more diffuse in the region above the body and is quite asymmetric.

At the station behind the wing, there are four sets of data with strakes on (Figures A-23 through A-26) and four without strakes (Figures A-27 through A-30). Unfortunately data were not obtained for a portion of the outer rake position, because of tunnel time limitation and because the strake vortex was more diffuse than was anticipated.

In general, there are significant differences between strake on and strake off. For example, comparison of Figures A-23 and A-27 indicates that the strake has a large organizing effect on the flow. A strong downwash occurs over the body due to the strake vortices and there is little indication of the presence of the nose vortex system, which is probably merged with the strake vortices. There is a low velocity region

20

in the core of the strake vortex, whereas without the strake, there is a
large unorganized "dead water" region over the wing. The probe readings,
in fact, in these low axial velocity regions are unreliable because the
angles of the flow approaching the probe exceed the range for which the
probe is calibrated. Without the strake, there is some indication of the
presence of the nose vortex system at 10 degrees sideslip. For example,
in Figure A-28 there is an indication of concentrated vorticity near the
vertical axis about 28 inches above the body axis and in Figure A-30
there is a similar indication just to the left of the vertical axis about
9 inches above the body axis. In order to define the vorticity field more
precisely, one would have to make detailed vorticity contour integrations,
which have not been done at this point.

Further comments are made regarding these data in Section 5.

3. WATER TUNNEL STUDIES

An experimental investigation was made in the NEAR water tunnel to obtain information on vortex shedding from noncircular nose shapes. The program and results are described in this section.

3.1 Objectives

The principal objective of these tests is to obtain simultaneous force and flow field data on a series of noncircular noses characteristic of real airplane noses. The nose shapes were selected to complement other parts of the overall investigation as well as to be representative of aircraft nose sections. Because of limited data acquisition capability, flow visualization was used to determine the vortex locations, and no velocity or vortex strength measurements were made. The purpose of the measurements is to check other data, to check the theory described in the next section, and to gain some understanding of the way in which nose shape affects the formation and location of the vortices shed from the nose.

3.2 Models

Three models were fabricated and tested. All were made to the same base area (equivalent base diameter of 6.25 cm (2.5 inches)). Two have length-to-diameter ratios of 5 and the third is slightly less. The model characteristics are shown in Figure 3.

The first model is the nose of the LRC V/STOL Fighter Aircraft model tested in the V/STOL tunnel, as described in the previous section. This model was selected to provide some data for comparison with the LRC data.

The second model is a tangent ogive with an elliptical cross section having a major-to-minor axis ratio of 1.44. The elliptical cross section is typical of many fighter aircraft and is used on a portion of the F-5 nose. This model is also identical to one of the models tested at Ames Research Center, on which considerable force and moment data exist (reference 4).

The third model is an F-5 aircraft nose. The length to equivalent base diameter is 4.4. The cross section area shape distribution was obtained from Langley Research Center, NASA, and is identical to that of the model of reference 5. As a part of the investigation of reference 5, a nose alone model was tested, but the NASA model is somewhat shorter (in terms of percent length of the overall fuselage) than the NEAR model. This model is of interest for two reasons. First, the aircraft is highly

22

V/STOL Nose

z

x

7.11 cm
(2.8 in)

19.81 cm (7.80 in)

31.75 cm (12.5 in)

5.3 cm
(2.09 in)

$S_b = 16.39$ cm^2
$(4.91$ in$^2)$

$d_{eq} = 6.35$ cm
$(2.50$ in$)$

ELLIPTIC OGIVE

z

x

7.62 cm
(3.0 in)

21.48 cm (8.46 in)

31.75 cm (12.5 in)

5.54 cm
(2.18 in)

$S_b = 16.39$ cm^2
$(4.91$ in$^2)$

$d_{eq} = 6.35$ cm
$(2.5$ in$)$

F-5 NOSE

z

x

6.27 cm
(2.47 in)

18.18 cm (7.16 in)

28.45 cm (11.2 in)

5.28 cm
(2.08 in)

$S_b = 32.5$ cm^2
$(5.04$ in$^2)$

$d_{eq} = 6.43$ cm
$(2.53$ in$)$
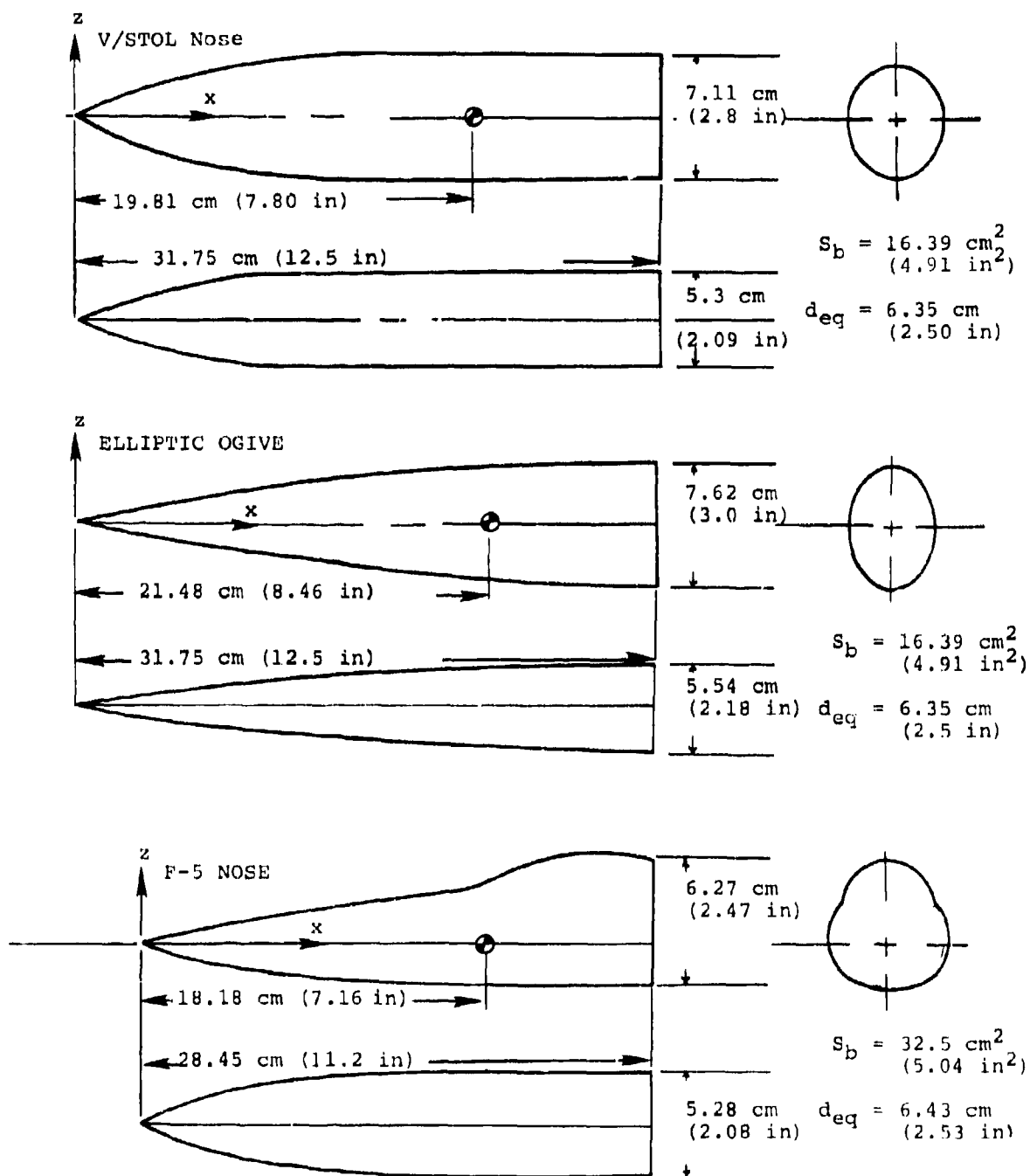
Figure 3. Water Tunnel Model Characteristics.

spin resistant due to the shape of the nose and is thus a very interesting configuration. Secondly, there are considerable force and moment data on this configuration from reference 5.

All models were constructed with a central steel support tube fashioned to hold a NEAR 3/4 inch, 5 component strain gage balance. Aluminum template sections were located at a number of stations along the axis, and the intermediate regions filled with an epoxy material, with the outer surface hand finished and painted black.

3.3 Test Conditions

The models were tested in the water tunnel at speeds from about 1.6 to 6.1 m/sec (5 to 20 ft/sec). The angle of attack range is 15 to 40 degrees, and sideslip angles of 0, ±5, and ±10 degrees were tested. Flow visualization was all done at a water speed of about 1.8 m/sec (6 ft/sec).

The models were tested in the 0.35 by 0.5 meter (14 by 20 inch) test section of the tunnel. A photograph of the arrangement is shown in Figure 4 with the water partially drained from the tunnel. The maximum blockage was about 7.7 percent. No corrections were made for blockage effects.

3.4 Measurements

Two kinds of measurements were made: force and moment and flow visualization. Initially, force and moment measurements were made in the absence of any flow visualization probes or other disturbances. The measurements were made with an internally mounted three-quarter inch diameter, 5 component strain gage balance (all components except drag). The instrumentation is shown in Figure 4 in the rack on the right. The system is capable of sampling the balance output at about 3 samples per second (limited by the printer) and, depending on the degree of unsteadiness, up to 25 samples were taken and averaged to obtain a balance reading.

After the force and moment tests were completed, flow visualization tests were conducted to determine the location of the vortex cores on the leeward side of the body. Initially a hydrogen bubble technique was tried. This involved cementing two 5 mil platinum wires along the pressure side of the body about 45 degrees around the curve of the body from the windward meridian. The wire was faired into the body with epoxy and scraped clean over the location where bubbles were wanted. This method worked only to show the separation line on the body, because the bubbles
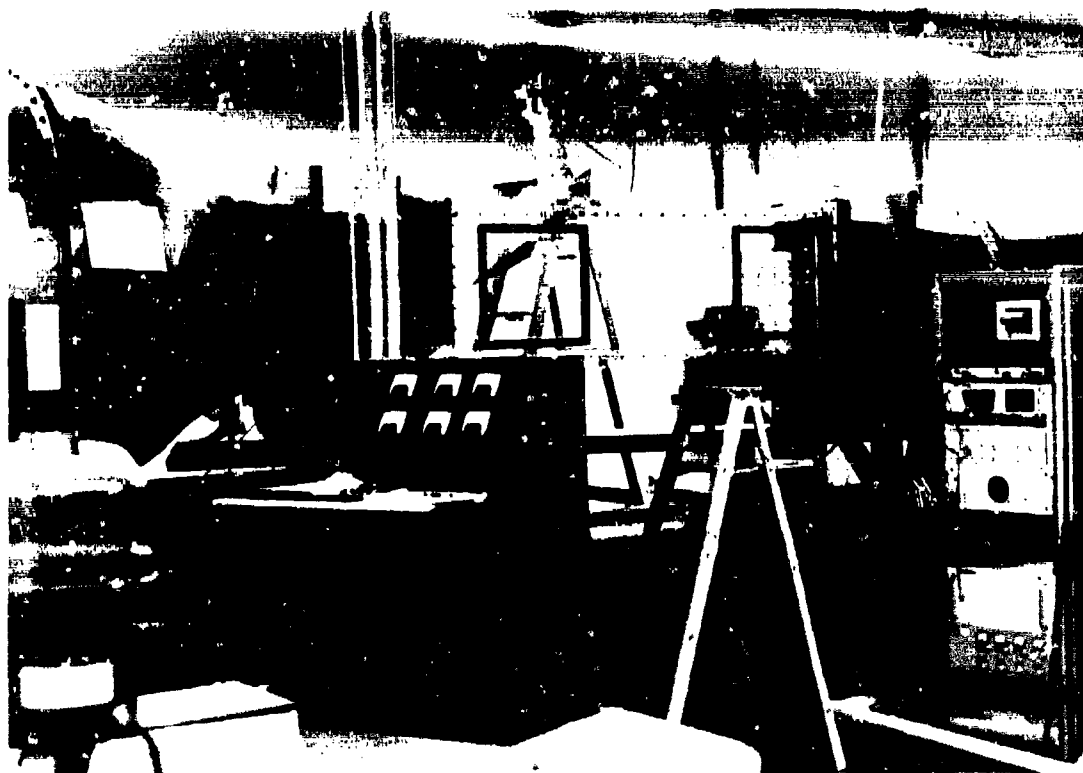
Figure 4. Arrangement of Model and Instrumentation
in the Tunnel.

25

would move along the body to the separation line, accumulate there, and ultimately break off to follow the vortex core. The bubble density was insufficient to show the vortex cores, and the method was limited to water speeds of the order of 0.6 m/sec (2 ft/sec).

The method used is one in which a probe was placed upstream of the model and used to supply air bubbles to the vicinity of the model. The probe consists of an L-shaped 1/8 inch diameter tube entering the tunnel on the sidewall upstream of the test section. An 0.028 inch tube was soldered to the large tube just downstream of the bend of the large tube. The end of the small tube was soldered and drilled to 0.016 inch. By sliding the probe through the fitting at the tunnel wall and rotating the probe, the tip of the small tube could be moved relative to the model to cause the bubble stream to impinge the model just aft of the nose tip. The model sting support system was used to position the model approximately correctly relative to the bubble stream. This system was operated at tunnel speeds up to about 3 m/sec (10 ft/sec) and was limited primarily by the structural integrity of the probe.

The probe was placed so the bubble stream impinged on the model just downstream of the nose tip. The bubbles followed and showed extremely well the vortex core locations. Photographs were obtained of the bubbles from the side and bottom (leeward model side) of the tunnel through the plexiglas test section. Examples of the photographs are shown in Figures 5-10. Measurements were made from the photographs to obtain vortex positions at 10 positions along the model length.

3.5 Results

The results of the water tunnel tests are presented in Appendix B. Included in these data are the basic forces and moments, an assessment of air bubble probe interference, and vortex position data on the four models (the elliptical cross section ogive was tested with major axis both horizontal and vertical).

The force and moment data with no probe present are shown in Figures B-1 through B-16. The Reynolds number is based on the tunnel test section velocity and the equivalent base diameter (the diameter of a circle having the base area). In some cases where the forces were unsteady, a range of force measured is shown. This occurred only with side force and yawing moment at the higher angles of attack. No corrections were made for water tunnel wall effects.

26
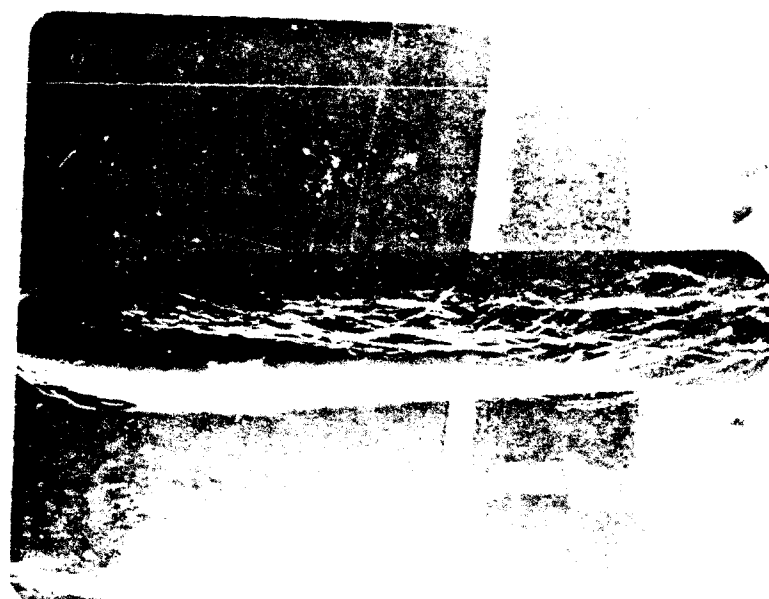
Figure 5. Air Bubble Photographs of V/STOL Nose
at $\alpha = 35°$, $\beta = 10°$.

27
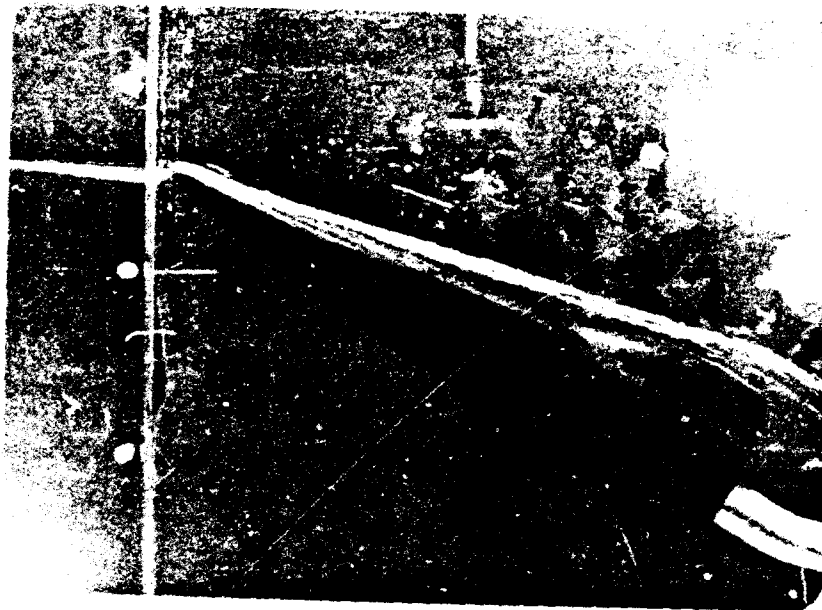
Figure 6. Air Bubble Photographs of F-5 Nose
at $\alpha = 30°$, $\beta = 10°$.

28
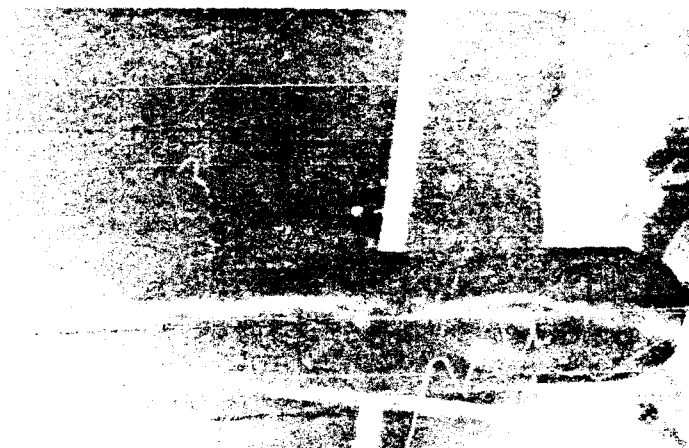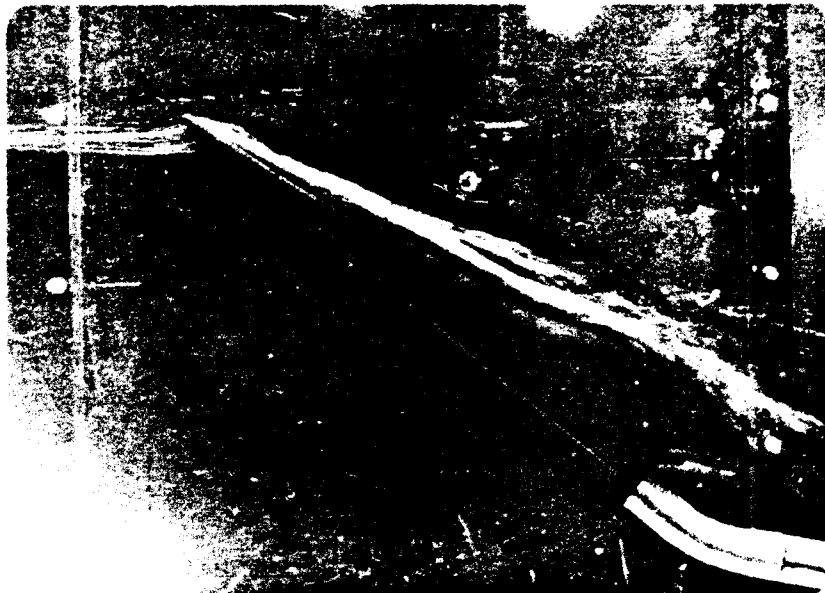
Figure 7.   Air Bubble Photographs of F-5 Nose
at α = 40°, β = 10°.
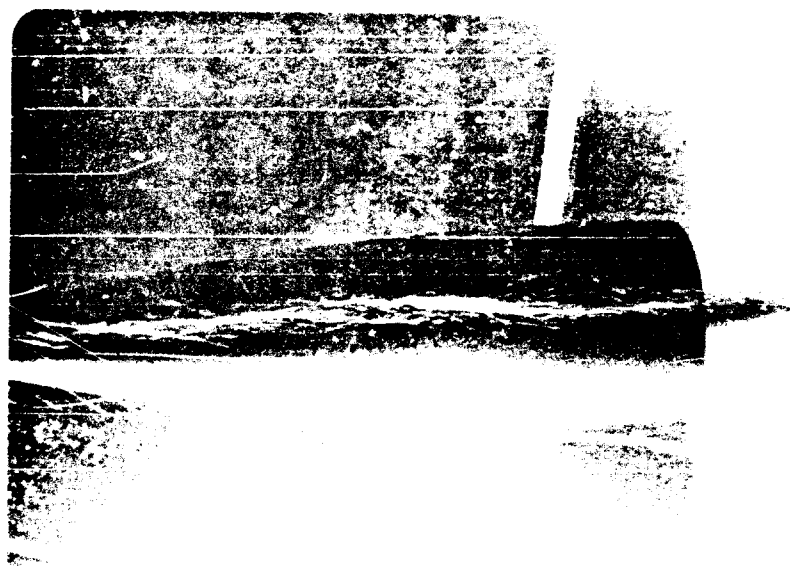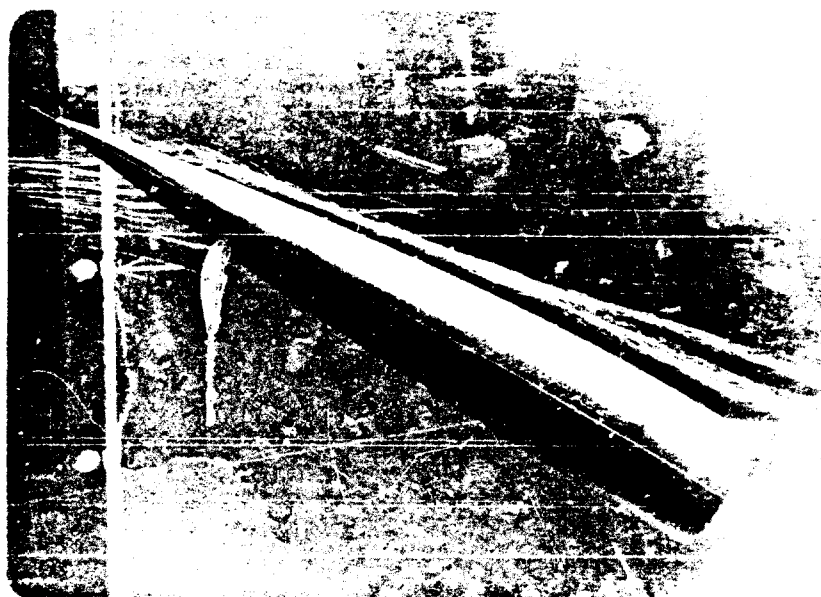
Figure 8. Air Bubble Photographs of Elliptical Ogive
with Major Axis Horizontal at $\iota = 30°$, $\beta = 10°$.

30
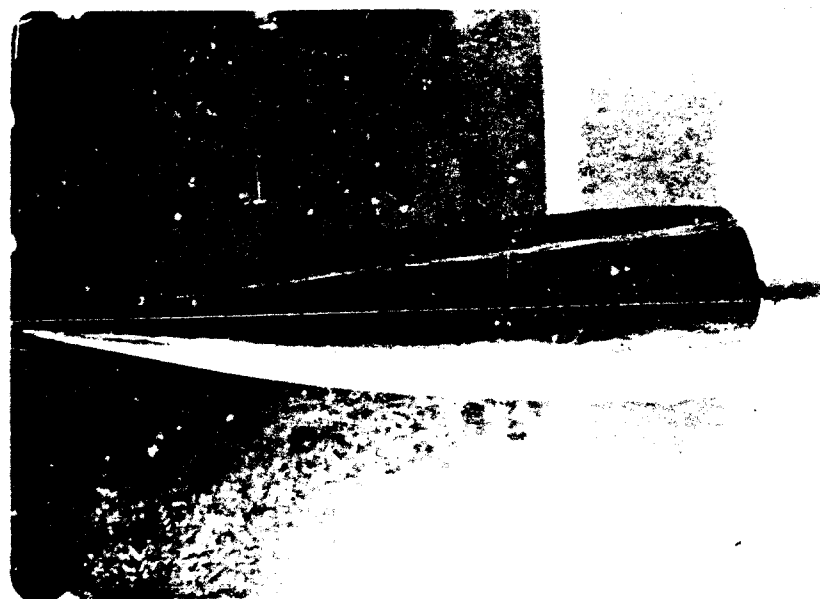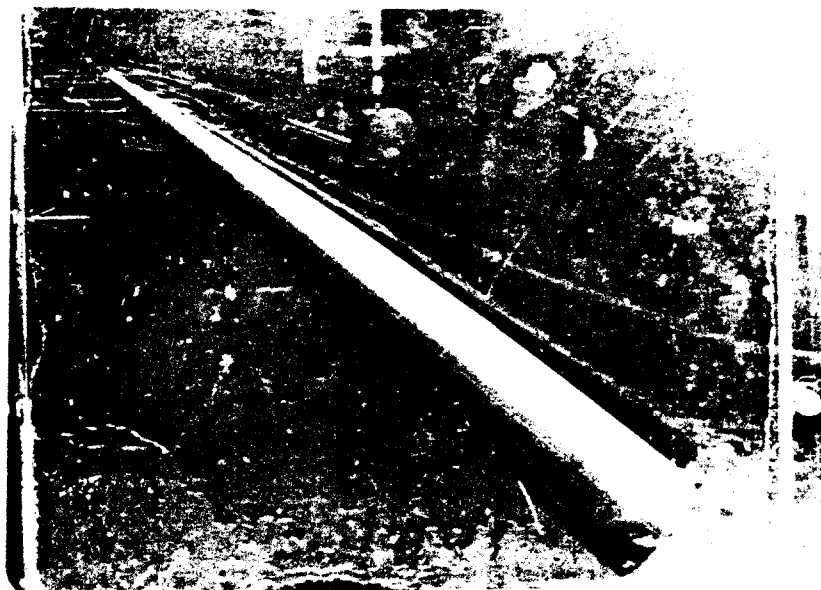
Figure 9. Air Bubble Photographs of Elliptical Ogive
with Major Axis Horizontal at $\alpha = 40°$, $\beta = 0°$.

31
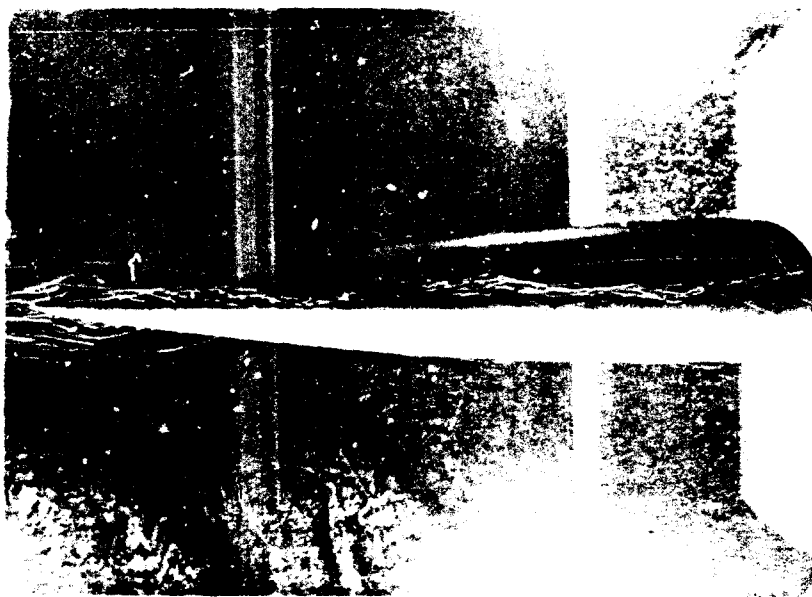
Figure 10. Air Bubble Photographs of Elliptical Ogive
with Major Axis Vertical at $\alpha = 40°$, $\beta = 0°$.

The results for the LRC V/STOL fighter model nose are shown in
Figures B-1 through B-4. There is a considerable Reynolds number influ-
ence, particularly on lateral effects. At the high Reynolds number,
there is very little side force, whereas the side force and yawing moment
are appreciable above 30° angle of attack at the lower Reynolds number.
The sideslip results show a linear behavior at 20° angle of attack and at
the higher Reynolds number at 35° angle of attack. At the lower Reynolds
number, Figure B-4 shows a reversal in sign of the sideslip derivative of
yawing moment. If the moment center were well aft of the nose base (as
would be the case in a complete aircraft configuration), rather than
forward of the base (Figure 3), the reversal would not occur, but the
results still show a significant effect of the nose vortex system on the
center of pressure of side force on the nose.

The results for the elliptical ogive with major axis horizontal are
shown in Figures B-5 through B-8. There is some Reynolds number effect,
but not as pronounced as in the V/STOL nose case. The flow becomes very
unsteady at 40 degrees angle of attack, as shown by the range of C_Y and
C_n data in Figures B-5 and B-6. The side-force and yawing-moment varia-
tions are reasonably linear with sideslip angle, as shown in Figures B-7
and B-8.

NASA side-force and yawing-moment data from reference 4 are shown in
Figures B-5 and B-6. These data show an opposite sign to the NEAR data,
which is not unexpected, in that at zero sideslip, the "hand" of the
asymmetric flow is determined by small asymmetries in the model or tunnel
flow. The magnitudes in the side-force data agree reasonably well. Both
sets of data show small C_n values below 25° (note the NEAR data is plotted
at ten times the scale values), but the NASA data show higher values at
the higher angles. The Reynolds numbers for the tests are different, but
there are insufficient data to establish the trend with Reynolds numbers.

With the major axis vertical (Figures B-9 through B-12), there are
considerable Reynolds number effects at zero sideslip. The lateral
effects appear at a lower angle of attack than was the case for the major
axis horizontal, and the flow is steadier at high angles of attack. The
NASA data show the same behavior as the NEAR data and are reasonably close
in magnitude, considering the size of the Reynolds number effects. The
variations with angle of sideslip are essentially linear.

33

The data for the F-5 nose are shown in Figures B-13 through B-16. The zero sideslip data show little influence of Reynolds number. It is remarkable that this nose configuration shows little side force or yawing moment over the entire range of angle of attack.

Figure B-13 shows NASA normal and side-force data from reference 5. The NASA model is somewhat shorter than the NEAR model, in that it represents 32 percent of the total fuselage length, whereas the NEAR model is 41 percent of the length. Although there is that difference, the forces shown in Figure B-13 agree well with the NEAR tunnel data. NASA moment data are not presented because of an uncertainty in the center of moments used, which could not be resolved.

The side-force data in Figure B-15 show a remarkable reversal in sign at about 34 degrees angle of attack for both Reynolds numbers tested. Below 34 degrees, the nose force is away from the sidewash velocity, whereas above 34 degrees, the side force is towards the sidewash. For a typical complete aircraft configuration with a center of gravity aft of the nose, the directional stability C_{n_β} also changes sign. The data of Figure B-16 do not show this effect because the center of moments for the water tunnel tests is well forward of the model base. The NASA side force data show the same trends as the NEAR data and the same crossover near $\alpha = 34°$.

The next group of data (Figures B-17 through B-25) present the results of the flow visualization studies. Examples of the photographs obtained with the air bubbles are shown in Figures 5 through 10. Figure 5 shows air bubble flow over the V/STOL nose, Figures 6 and 7 show the F-5 nose, and Figures 8-10 show the ogive.

The influence of the probe on the forces and moments were investigated by taking concurrent measurements from the balance with the photography. Balance measurements were taken for the cases of probe inserted with no air and probe with air and compared to the measurements made with the probe withdrawn. The results of these measurements are shown in Figures B-17 through B-20. Generally these data show little influence of the probe presence on the normal force and pitching moment (mostly less than 10 percent change) and a considerably larger effect on the side force and yawing moment. Also the wake of the probe itself appears to have a much greater influence on the model loads than do the air bubbles, because the probe and probe-plus-air interference are generally very close.

34

The fractional changes in lateral loads would be expected to be higher than those in the vertical plane for two reasons. First, the lateral loads are smaller, particularly at the low angles of attack, and small differences result in larger fractional changes. Secondly, the lateral loads are caused by small asymmetries in the model or onset flow and are much more sensitive to changes in the flow asymmetry than the vertical plane loads.

On the basis of considerable experimentation with the probe and model in the water tunnel and moving the probe vertically with respect to the model to cause the probe wake and bubbles to impinge on the model at different locations, it is felt that the photographs obtained represent the actual vortex system quite well. In all cases, the vortex system visualized by the bubbles was quite stable and did not jitter or appear to be on the verge of shifting "hand". In all cases except possibly the elliptic ogive with major axis vertical at the highest angle of attack, there was a two vortex system completely visualized by the bubbles flowing over the model near its nose, as shown in Figure 6, for example. In all cases except the V/STOL nose, the vortex cores were well defined, as in Figures 6 and 7, and the core positions could be read to within about ±0.10 of the local body radius. The vorticity in the leeward side flow over the V/STOL nose appeared more diffuse (Figure 5), and the cores were more difficult to define.

Measured vortex positions for all cases in which data were obtained are presented in Table B-1. Selected data for each of the four nose shapes are presented in Figures B-21 through B-25. The lateral and vertical coordinates are nondimensionalized by the equivalent base diameter. Also shown are outlines of the model to place the vortex positions relative to the model.

The results for the V/STOL nose in Figure B-21 are typical in that the vortices lay close to and over the body surface, even at 10 degrees of sideslip. The lower case of Figure B-21 corresponds to the photograph of Figure 5, and there is some indication of a second vortex forming on the right side near the 80 percent station as the first vortex bends away from the body, although it is difficult to tell precisely. The diffuseness of the vorticity is evident by comparing Figures 5 and 6.

The elliptic ogive results of Figures B-22 and B-23 indicate a large vertical height difference between the right and left vortices, even at

35

30 degrees angle of attack, with the major axis vertical showing the greatest differences. The vortex that rises the greatest distance vertically also moves the greatest distance outboard for zero sideslip.

The F-5 results shown in Figure B-24 for zero sideslip indicate small vertical position differences and lateral asymmetries for both 30 and 40 degrees angle of attack, which is consistent with the small lateral forces developed on this configuration. The results at 10 degrees of sideslip (Figure B-25) bracket the angle of attack at which the side force direction changes sign. It is interesting to note that for the smaller angles of attack, the vortex system is sufficiently close to the body that when sideslip is introduced, the windward vortex position is strongly influenced by the canopy. It is possible that this effect is responsible for the reversal in sign of side force in going from 30° to 40°.

4. ASYMMETRIC VORTEX SHEDDING ANALYSIS

Numerous prediction methods have been developed in an attempt to understand the separated flow field and induced forces associated with bodies at high angles of attack. Generally, these methods consider a body of revolution and represent the wake as a series of discrete vortices in crossflow planes. Typically, empiricism is used to specify the strength and initial position of the shed vortices, and potential flow methods are used to track the vortices as they move downstream. One prediction method which eliminates the need for much of this type of empiricism is that developed by Marshall and Deffenbaugh (ref. 6).

In this reference, a three-dimensional steady flow problem is reduced to a two-dimensional unsteady separated flow problem for solution. Thus, the problem is reduced to that of the flow about a circular body in a crossflow plane in the presence of discrete vortices. The radius of the body is changing with time, and at each time step, corresponding to an interval of length on the body, a new vortex pair is shed into the flow field from the separation points. The location of each separation point is determined by solving the laminar boundary layer equations in two dimensions, and the strength of each vortex is determined by the vorticity flux in the boundary layer at separation during the time interval. Some initial results from this method indicate good prediction of the normal forces on bodies of revolution at moderate angles of attack. The analysis of reference 6 is restricted to the symmetric problem in which there are no induced side forces.

In reference 7, Deffenbaugh and Koerner extend the prediction method to asymmetric flow about bodies of revolution. This analysis considers the separation of turbulent boundary layers through the use of Stratford's criterion.

The purpose of the work described herein is to develop a method, based on the approach of references 6 and 7, to predict the asymmetric flow field and induced forces and moments on realistic aircraft nose shapes at high angles of attack. The method is applicable to noncircular cross section shapes, uses both laminar and turbulent separation criteria in a more simplified boundary layer treatment, adds a three-dimensional thickness solution, and adds consideration of the axial flow as well as crossflow component to improve the separation prediction. The method of analysis and some predicted results are presented.

37

4.1 Analysis

4.1.1 Geometry

The configurations considered in this study of vortex shedding are
bodies alone; that is, bodies without fins or control surfaces. Thus,
the method is suitable for use on long slender missile configurations as
well as shorter aircraft noses. The bodies need not be axisymmetric as
it is only necessary that the coordinates describing the cross-sectional
shape be defined at a number of axial stations. Neither top-bottom or
right-left symmetry is required, but there are some shape restrictions
imposed by the numerical methods used. Since a Fourier series representa-
tion of the transformation function is used, sharp corners and long flat
body panels in the cross section are to be avoided. Discontinuous axial
distributions of cross-sectional areas should also be avoided because of
resulting numerical difficulties.

4.1.2 Noncircular bodies

The solution for the two dimensional potential flow around a circle
in the presence of a uniform flow and external vortices is well known and
is documented numerous places in the literature, for example, references
6 and 8. When the body cross-sectional shape is noncircular, the poten-
tial solution is not readily obtainable. The procedure used to handle
noncircular shapes is to find a conformal transformation which will map
every point on or outside the noncircular body to a corresponding point
on or outside a circular body. Thus, the potential flow solution can be
written for the circular body and transformed to the noncircular body.

For some simple shapes like an ellipse, the transformation to the
circle is relatively simple and can be carried out analytically. As the
noncircular shape becomes more complex, the transformation cannot be
done analytically and some numerical procedure must be used. The numer-
ical procedure chosen is a form of the Theodorsen's transformation given
by the relation

$$\frac{d\sigma}{d\nu} = \exp\left(\sum_{n=0}^{N} \frac{A_n - iB_n}{\nu^n}\right) \tag{1}$$

where

$$\nu = \tau + i\lambda \tag{2}$$

as illustrated in figure 11. For each point σ on the real body cross section there is a corresponding point ν on the circle.

The Fourier coefficients, A_n and B_n, in equation (1) are obtained from a numerical Fourier analysis procedure developed by A. Jameson for use in transforming arbitrary airfoil shapes to a circle (ref. 9). Given the Fourier coefficients, the mapping of known points in one plane to corresponding points in the second plane is carried out numerically as described in Appendix C.

4.1.3 Equations of motion

In this section, the equations of motion of a shed nose vortex in the presence of an arbitrary number of other free vortices in the vicinity of a noncircular body are derived. The transformation of the noncircular body to the circle is given by equation (1), and the mapping of corresponding points from one plane to the other is described in Appendix C.

In the circle (ν) plane, let the position of a vortex, Γ_n, be denoted as

$$\nu_{n_\Gamma} = \tau_n + i\lambda_n \tag{3}$$

and the image of Γ_n is located at

$$\nu_{n_{-\Gamma}} = \frac{r_0^2}{\bar{\nu}_n} \tag{4}$$

The complex potential in the circle plane is

$$W(\nu) = \phi + i\psi \tag{5}$$

and the velocity field in the circle plane is

$$v' - iw' = \frac{dW(\nu)}{d\nu} \tag{6}$$
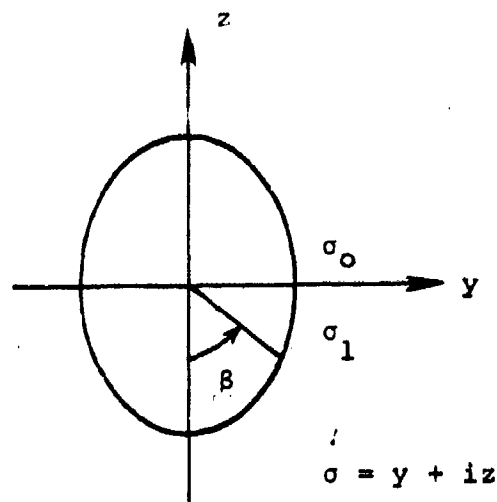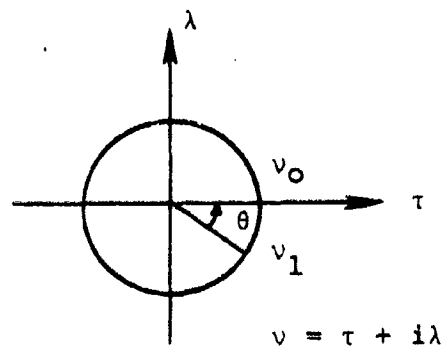
Real Plane

Circle Plane

Figure 11. Body Cross Section Nomenclature.

In the real plane, the position of the vortex Γ_n is

$$\sigma_{n_\Gamma} = y_n + iz_n \tag{7}$$

The complex potential in the real plane is

$$W(\sigma) = \phi + i\Psi \tag{8}$$

and the corresponding velocity field is

$$v - iw = \frac{dW(\sigma)}{d\sigma} \tag{9}$$

The complex potential of the flow in the circle plane is described by the following components:

(1) crossflow due to α,

$$W_\alpha(\nu) = - i\nu \, V \sin\alpha \tag{10}$$

(2) crossflow due to β,

$$W_\beta(\nu) = - \nu \, V \sin\beta \tag{11}$$

(3) cylinder in α-flow (doublet),

$$W_{r_\alpha}(\nu) = i\left(\frac{r_0^2}{\nu}\right) V \sin\alpha \tag{12}$$

(4) cylinder in β-flow (doublet),

$$W_{r_\beta}(\nu) = -\left(\frac{r_0^2}{\nu}\right) V \sin\beta \tag{13}$$

(5) expanding cylinder,

$$W_{\dot{r}_0}(\nu) = r_0 \frac{dr_0}{dx} (\ln \nu) V \cos\alpha \tag{14}$$

(6) vortex Γ_n outside cylinder,

$$W_{n_\Gamma}(\nu) = - i\frac{\Gamma_n}{2\pi} \ln(\nu - \nu_n) \tag{15}$$

(7) image of Γ_n,

$$W_{n_{-\Gamma}}(\nu) = i\frac{\Gamma_n}{2\pi} \ln\left(\nu - \frac{r_0^2}{\bar{\nu}_n}\right) \tag{16}$$

The total potential for the flow in the circle plane is the sum of equations (10) to (16) and may be written as

41

$$W(\nu) = -(V \sin \beta)\left(\nu + \frac{r_0^2}{\nu}\right) - i(V \sin \alpha)\left(\nu - \frac{r_0^2}{\nu}\right) + (V \cos \alpha)\, r_0 \frac{dr_0}{dx} \ln \nu$$

$$+ i \sum_{n=1}^{N} \frac{\Gamma_n}{2\pi} \ln\left(\frac{\nu - r_0^2/\bar{\nu}_n}{\nu - \nu_n}\right) \tag{17}$$

where N = total number of shed vortices.

The complex potential $W_m(\sigma)$ governing the motion of vortex Γ_m in the real (σ) plane can be written as

$$W_m(\sigma) = -(V \sin \beta)\left(\nu + \frac{r_0^2}{\nu}\right) - i(V \sin \alpha)\left(\nu - \frac{r_0^2}{\nu}\right)$$

$$+ (V \cos \alpha)\, r_0 \frac{dr_0}{dx} \ln \nu + i \sum_{n=1}^{N} \frac{\Gamma_n}{2\pi} \ln\left(\frac{\nu - r_0^2/\bar{\nu}_n}{\nu - \nu_n}\right)_{n \neq m}$$

$$+ i \frac{\Gamma_m}{2\pi} \ln\left(\nu - \frac{r_0^2}{\bar{\nu}_m}\right) - i \frac{\Gamma_m}{2\pi} \ln(\nu - \nu_m) + i \frac{\Gamma_m}{2\pi} \ln(\sigma - \sigma_m) \tag{18}$$

where the last term represents the potential of Γ_m in the σ-plane which has been removed from the potential to eliminate the singularity at Γ_m.

The velocity of Γ_m is

$$v_m - iw_m = \left.\frac{dW_m(\sigma)}{d\sigma}\right|_{\substack{\sigma = \sigma_m \\ \nu = \nu_m}} \tag{19}$$

Note that the last two terms in equation (18) are singular at $\sigma = \sigma_m$ and $\nu = \nu_m$. Combining the last two terms of (18) and taking the limit results in the following.

$$\lim_{\substack{\sigma \to \sigma_m \\ \nu \to \nu_m}} \frac{d}{d\sigma}\left[\ln\left(\frac{\sigma - \sigma_m}{\nu - \nu_m}\right)\right] = \left. -\frac{1}{2} \frac{d\sigma}{d\nu} \frac{d^2\nu}{d\sigma^2}\right|_{\sigma_m} \tag{20}$$

The details of this derivation are carried out in Appendix A of reference 8.

From (20),

$$-\frac{1}{2} \frac{d\sigma}{d\nu} \frac{d^2\nu}{d\sigma^2} = -\frac{1}{2} \frac{d}{d\nu}\left(\frac{d\nu}{d\sigma}\right) \tag{21}$$

and, from (1),

42

$$\frac{d\nu}{d\sigma} = \exp\left[- \sum_{\ell=0}^{L} \frac{A_\ell - iB_\ell}{\nu^\ell}\right] \qquad (22)$$

where L is the number of Fourier coefficients required to describe the transformation. Therefore, from (21) and (22)

$$\frac{d}{d\nu}\left(\frac{d\nu}{d\sigma}\right) = \left[\sum_{\ell=0}^{L} \ell \frac{A_\ell - iB_\ell}{\nu^{\ell+1}}\right] \exp\left[- \sum_{\ell=0}^{L} \frac{A_\ell - iB_\ell}{\nu^\ell}\right] \qquad (23)$$

The velocity at vortex Γ_m is found in the following manner.

$$v_m - iw_m = \frac{d}{d\nu}\left[W_m(\sigma)\right]\frac{d\nu}{d\sigma} \qquad (24)$$

We will assume the following form for equation (24):

$$\frac{v_m - iw_m}{V} = G_\alpha + G_\beta + G_{r_0} + G_n + G_m + G_T \qquad (25)$$

Each term in (25) represents a velocity component in the σ plane. The first term represents the flow about a body in an α-type crossflow.

$$G_\alpha = - i \sin \alpha \left[1 + \left(\frac{r_0}{\nu_m}\right)^2\right] \frac{d\nu}{d\sigma}\Bigg|_{\sigma = \sigma_m} \qquad (26)$$

The second term represents the flow about a body in a β-type crossflow.

$$G_\beta = - \sin \beta \left[1 - \left(\frac{r_0}{\nu_m}\right)^2\right] \frac{d\nu}{d\sigma}\Bigg|_{\sigma = \sigma_m} \qquad (27)$$

The third term is due to the change in body radius and is

$$G_{r_0} = \frac{r_0}{\nu_m}\frac{dr_0}{dx} \cos \alpha \; \frac{d\nu}{d\sigma}\Bigg|_{\sigma = \sigma_m} \qquad (28)$$

The next term represents the influence of all vortices and their images, with the exception of Γ_m.

$$G_n = i \sum_{n=1}^{N} \frac{\Gamma_n}{2\pi r_0 V}\left[\frac{1}{(\nu_m/r_0) - (r_0/\bar{\nu}_n)} - \frac{1}{(\nu_m/r_0) - (\nu_n/r_0)}\right]_{n \neq m} \frac{d\nu}{d\sigma}\Bigg|_{\sigma = \sigma_m} \qquad (29)$$

The next term is due to the image of Γ_m.

$$G_m = i \frac{\Gamma_m}{2\pi r_0 V}\left[\frac{1}{(\nu_m/r_0) - (r_0/\bar{\nu}_m)}\right]\frac{d\nu}{d\sigma}\Bigg|_{\sigma = \sigma_m} \qquad (30)$$

43

The last term in (25) represents the last two terms of (18) and is written, with (20) and (23) as

$$G_T = - i \frac{\Gamma_m}{2\pi V} \left(\frac{1}{2}\right) \left(\sum_{\ell=0}^{L} \ell \frac{A_\ell - iB_\ell}{\nu_m^{\ell+1}}\right) \exp\left(- \sum_{\ell=0}^{L} \frac{A_\ell - iB_\ell}{\nu_m^\ell}\right) \qquad (31)$$

Thus, equations (25) through (31) specify the complete velocity field at vortex Γ_m in the real plane.

The differential equations of motion for Γ_m are

$$\frac{d\bar{\sigma}_m}{dx} = \frac{v_m - iw_m}{V \cos \alpha_c} \qquad (32)$$

where

$$\bar{\sigma}_m = y_m - iz_m \qquad (33)$$

Therefore, the two equations which must be integrated along the body length to determine the trajectory of Γ_m are

$$\frac{dy_m}{dx} = \frac{v_m}{V \cos \alpha_c} \qquad (34)$$

and

$$\frac{dz_m}{dx} = \frac{w_m}{V \cos \alpha_c} \qquad (35)$$

There are a pair of equations like (34) and (35) for each vortex in the field. Thus, as new vortices are shed, the number of equations to solve increases.

The above differential equations of motion for the vortices are solved numerically using a method which automatically adjusts the step size to provide the specified accuracy.

4.1.4 Surface pressure distribution

The surface pressure distribution on the body is required for two purposes: to calculate the distribution of forces on the body and to calculate the separation points on the body. The surface pressure coefficient is determined from the unsteady Bernoulli equation as follows.

$$p_\infty + \frac{1}{2} \rho v^2 + \rho \frac{d\phi}{dt}\Big|_\infty = p + \frac{1}{2} \rho U^2 + \rho \frac{d\phi}{dt}\Big|_{r_0} \qquad (36)$$

Defining the pressure coefficient as

44

$$C_p = \frac{p - P_\infty}{\frac{1}{2} \rho V^2} \tag{37}$$

and U as the total local velocity (including V), equation (36) becomes

$$C_p = 1 - \left(\frac{U}{V}\right)^2 - \frac{2}{V^2} \frac{d\phi}{dt}\bigg|_{r_0} \tag{38}$$

A difficulty arises in handling the unsteady term on the left side of (36). In reference 6, the pressure coefficient was determined within an unknown constant as a result of this term, and a known pressure coefficient at one point on the body was used to evaluate the constant. In the present method, the two-dimensional doublet in the crossflow plane representing the expanding radius is replaced with a three-dimensional source-sink distribution representing the entire body (ref. 10). This modified velocity potential approaches zero at infinity, thus allowing calculation of an absolute pressure coefficient. The details of this derivation are presented in Appendix D.

The unsteady term in equation (38) is written as follows.

$$\frac{2}{V^2} \frac{d\phi}{dt}\bigg|_{r_0} = \frac{-4\tau}{r_0} \sin\beta \cos\alpha \frac{dr_0}{dx} + \frac{4\lambda}{r_0} \sin\alpha \cos\alpha \frac{dr_0}{dx}$$

$$+ 2\cos^2\alpha_c \sum_{j=1}^{J} \frac{Q_j^*[(x - x_j) + r_0 \, dr_0/dx]}{[(x - x_j)^2 + r_0^2]^{3/2}}$$

$$+ \sum_{n=1}^{N} \frac{\Gamma_n}{2\pi V} V^2 \cos\alpha_c \left\{ -\left[\frac{(\tau - \tau_n) \, d\lambda_n/dx - (\lambda - \lambda_n) \, d\tau_n/dx}{(\tau - \tau_n)^2 + (\lambda - \lambda_n)^2} \right] \right.$$

$$- \left[\frac{1}{(\tau r_n^2 - \tau_n r_0^2)^2 + (\lambda r_n^2 - \lambda_n r_0^2)^2} \right]$$

$$\times \left[(\tau r_n^2 - \tau_n r_0^2) \left(2\lambda\tau_n \frac{d\tau_n}{dx} + 2\lambda\lambda_n \frac{d\lambda_n}{dx} - r_0^2 \frac{d\lambda_n}{dx} - 2r_0\lambda_n \frac{dr_0}{dx} \right) \right.$$

$$\left. \left. - (\lambda r_n^2 - \lambda_n r_0^2) \left(2\tau\tau_n \frac{d\tau_n}{dx} + 2\tau\tau_n \frac{d\lambda_n}{dx} - r_0^2 \frac{d\tau_n}{dx} - 2r_0\tau_n \frac{dr_0}{dx} \right) \right] \right\} \tag{39}$$

where Q_j^* is the dimensionless source strength and J is the total number of sources describing the body.

The unsteady term of equation (39) is written in terms of the trans-
formed body; that is, the axisymmetric body. This is necessary because of
the use of a simple source-sink distribution on the axis to model the body
growth. We will assume that the unsteady term is unchanged between cor-
responding points on the circle and the real body. The velocity compon-
ents used in equation (38) are the actual surface velocities on the real
body.

4.1.5 Boundary-layer separation

The approach taken in this analysis requires that the separation
points on the body at each cross section be known in order to specify the
strength and initial position of the shed vortices. In reference 6, the
laminar boundary-layer equations are solved to determine the separation
points. In the present analysis, separation criteria based on the poten-
tial pressure distribution are utilized to predict both laminar and tur-
bulent separation.

Laminar separation—A separation criterion proposed by Stratford in
reference 11 states that the laminar boundary layer separates when

$$C_p^{1/2} \left[\xi \frac{dC_p}{d\xi} \right] \approx 0.087 \qquad (40)$$

This criterion, with a slightly different value of the constant (0.102),
is discussed in reference 12. For purposes of this analysis, the original
constant shown in equation (40) will be used. Also, ξ is the run length
of the laminar boundary layer measured from a false origin.

To apply equation (40) on the body surface in the crossflow plane,
some redefinition of the pressure coefficient is required. Stratford's
criterion is based on a flow in which the boundary layer develops on a
flat plate in a constant pressure region followed by an adverse pressure
region in which the boundary layer separates. This is illustrated in the
following sketch.
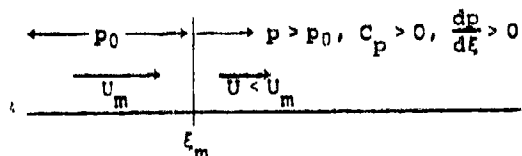
The point at which the local pressure starts to increase is denoted as ξ_m
which corresponds to the minimum pressure point on a body in a crossflow
plane. Defining a new surface pressure coefficient, C_p', which must be

46

zero at ξ_m and increases downstream, the surface pressure coefficient required in equation (40) can be written as

$$C_p' = 1 - (1 - C_p) \frac{v^2}{U_m^2} \tag{41}$$

where U_m is the potential velocity at the minimum pressure point.

The specification of the location of the false origin for a laminar boundary layer on a circular body in a crossflow is determined as follows. As shown in the sketch below
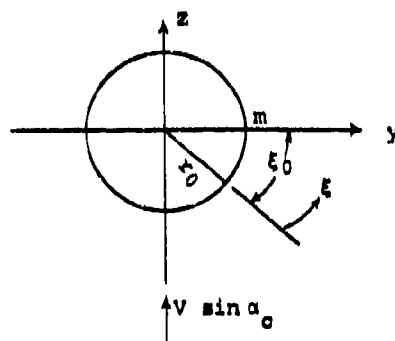
the minimum pressure point is denoted m and the false origin is a distance ξ_0 upstream of m. From figure 12.11 of reference 13, the displacement thickness of the laminar boundary layer at m, given by the von Karman-Pohlhausen solution, is

$$\frac{\delta^*}{\ell} \sqrt{\frac{V \sin \alpha_c \, \ell}{\nu}} = 0.6 \tag{42}$$

where ℓ is the diameter of the circle. The displacement thickness on a flat plate boundary layer with constant pressure equal to the minimum pressure at m on the cylinder is

$$\delta^* = \frac{1.721 \, \xi_0}{\sqrt{\dfrac{V \sin \alpha_c \, \xi_0}{\nu}}} \tag{43}$$

where ξ_0 is the flat plate run length. Assuming that δ^* from equations (42) and (43) are equal and that ξ_0 is the distance on the surface of the cylinder between m and the false origin, we get

$$\xi_0 = 0.49 \, r_0 \tag{44}$$

47

Thus, the run length, ξ, in equation (40) is measured from a point which is a length ξ_0 upstream of the minimum pressure point on the body.

It can be shown by a similar analysis that the false origin on an elliptic cross-sectional body is located about the same length upstream of the minimum pressure point as on a circular body. It will also be shown later, that the location of the false origin is not a critical factor in the prediction of laminar boundary-layer separation using equation (40); therefore, the length given by equation (44) will be used to specify the false origin on all shapes considered in the current work.

Turbulent separation—A separation criterion for turbulent boundary layers is proposed by Stratford in reference 11 which states that separation occurs when

$$C_p \left(\xi \frac{dC_p}{d\xi} \right)^{1/2} (10^{-6} Re_\xi)^{-0.1} = F(\xi) \tag{45}$$

where $0.35 \leq F(\xi) \leq 0.40$ at separation.

$$Re_\xi = \frac{U_m \xi}{\nu} \tag{46}$$

The false origin is specified by

$$\xi_0 = \int_0^{\xi_m} \left(\frac{u_e}{U_m} \right)^4 d\xi \tag{47}$$

assuming a fully turbulent boundary layer. In equation (47), u_e is the local surface velocity and the integration is carried out from the stagnation point to the minimum pressure point. In equation (45), C_p is the modified pressure coefficient, C_p', from equation (41), and as in the laminar criterion, ξ is measured from the false origin.

Three Dimensionality Effects—The Stratford criteria are based on two dimensional data and work well for circular bodies in crossflow; i.e. $90°$ angle of attack. For inclined bodies at angles of attack less than $90°$, an axial flow component is added to the crossflow component, the boundary layer run lengths are longer, and separation tends to occur a shorter distance beyond the minimum pressure points on the body. An approximate correction for this effect is obtained by multiplying the right hand sides of equations (40) and (45) by $\sin \alpha_c$; i.e., for the turbulent case

$$F(\xi) = 0.35 \sin \alpha_c \tag{48}$$

48

4.1.6 Separated wake

The potential model of the separated wake is made up of a large number of individual vortices, one shed from each separation point on either side of the body at each time step. The details of the specification of each individual vortex is described in the following sections.

Vorticity flux—In the same manner as in reference 6, the vorticity flux across the boundary layer at the separation point is

$$\gamma = \frac{U^2}{2} \qquad (49)$$

assuming no slip at the wall. In a given time step Δt, which is related to the distance between shedding points by the relationship

$$\Delta t = \frac{\Delta x}{V \cos \alpha_c} \qquad (50)$$

the vorticity flux is summed into a single point vortex whose strength is

$$\Gamma = \frac{U^2}{2} \Delta t \qquad (51)$$

Since the surface velocity, U, is dependent on position on the body, the strength of the shed vortex depends on the location of the separation point on each side of the body. The strength of a vortex, once determined from equation (51), is not changed at any point downstream; however, the net vorticity in the flow field is constantly changing because new vortices are shed at each interval of time. For the present work, the intervals between shed vortices are constant over the entire length of the body. The calculation procedure sheds a vortex from each side of the body at each time step if a separation point is found by the Stratford criterion described in a previous section.

In the calculation procedure, the vortex strength is referenced to the free-stream velocity and equation (51) is written as

$$\frac{\Gamma}{V} = \frac{1}{2}\left(\frac{U}{V}\right)^2 (V\Delta t) \qquad (52)$$

Initial position—As the vortices are shed into the outer flow, they must be given some initial position from which they begin their motion. In reference 6, the vortices are placed at

$$m_k = \frac{|U|\Delta t}{2\pi} \qquad (53)$$

which is illustrated in the sketch below.

49
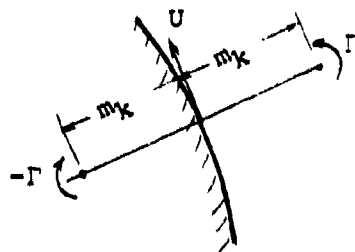
The vortex and its image are placed such that the surface velocity U is
exactly cancelled by the induced effect of the vortices. Equation (53) is
based on the assumption that $m_k \ll r_0$, which is why the vortex and its
image are equidistant from the body surface $(m_k = m_k')$. If the curvature
of the surface is considered, the initial vortex position outside a circu-
lar body is given by

$$m_k = \frac{2r_0 (\Gamma/V)}{2\pi r_0 (U/V) - (\Gamma/V)}\tag{54}$$

and the image position is specified by

$$m_k' = r_0 - \frac{r_0^2}{r_0 + m_k}\tag{55}$$

The positions given by equations (54) and (55) also satisfy the condition
that the net velocity on the surface at the separation point is zero.

It can be seen from either equation (53) or (54) that the initial
vortex position is a function of the location of the separation point and
the length of the time step. In the course of this investigation, it was
found that a reasonable length time step which would produce good detail
in the wake would also cause the initial vortex positions to be very close
to the body surface. The effect was that the vortex was "captured" by its
image and did not move out into the flow field away from the body. This
difficulty was overcome by arbitrarily placing the vortex at a point
specified by

$$m_k = 0.05 \, r_0\tag{56}$$

whenever m_k from equation (54) was less than 5 percent of the radius.

Vortex diffusion—The velocity induced by a point vortex in a cross-
flow plane can be written as

50

$$\frac{U}{V} = \frac{\Gamma/V}{2\pi r} F_D \tag{57}$$

where $F_D = 1$ for a potential vortex. The major difficulty with equation (57) occurs when r, the distance from the vortex to the point of interest, is small and the induced velocity is large. In the limit of trying to calculate the induced velocity at the center of the vortex ($r=0$), the result is singular. The induced velocity from a potential vortex is illustrated in figure 12.

Real vortices do not exhibit this singularity effect but tend to diffuse with time. A representation of this effect is to let

$$F_D = 1 - \exp\left(-\frac{r^2}{4t\nu}\right) = 1 - \exp\left(-\frac{r^2 R_e \cos\alpha}{4\Delta x}\right) \tag{58}$$

where

$$R_e = \frac{V}{\nu_e}\left(\frac{\nu_e}{\nu}\right)$$

$$\Delta x = x_{local} - x_{shed} \tag{59}$$

ν_e = effective kinematic viscosity

Equation (58) includes a viscous effect through the unit Reynolds number and an aging effect through the Δx term. The Reynolds number has been modified by use of an effective kinematic viscosity ν_e to permit larger viscosities to be used to increase the diffusion effect. In all the calculations made to date, however, this feature was not used, and the same unit Reynolds number was applied to equation (58) as was applied to calculationsof the boundary layer characteristics. The induced velocity from equation (57) with the F_D factor included is shown in figure 12.

Vortex reduction factor—It was shown in reference 6 that better agreement between experiment and theory would be obtained if only a fraction of the vorticity produced by boundary-layer separation is retained in the wake. The fraction that appears to give best agreement is 0.6. In the present investigation, the vorticity shedding factor is fixed at 0.6 unless otherwise noted. This factor is used in the right-hand side of equation (52).

Vortex coalescence—As the calculation proceeds, the number of vortices in the wake steadily increases, with an associated increase in computation time and costs. In an effort to decrease the computation time without sacrificing the accuracy of the predictions, certain pairs of vortices are combined into one vortex to reduce the total number of vortices
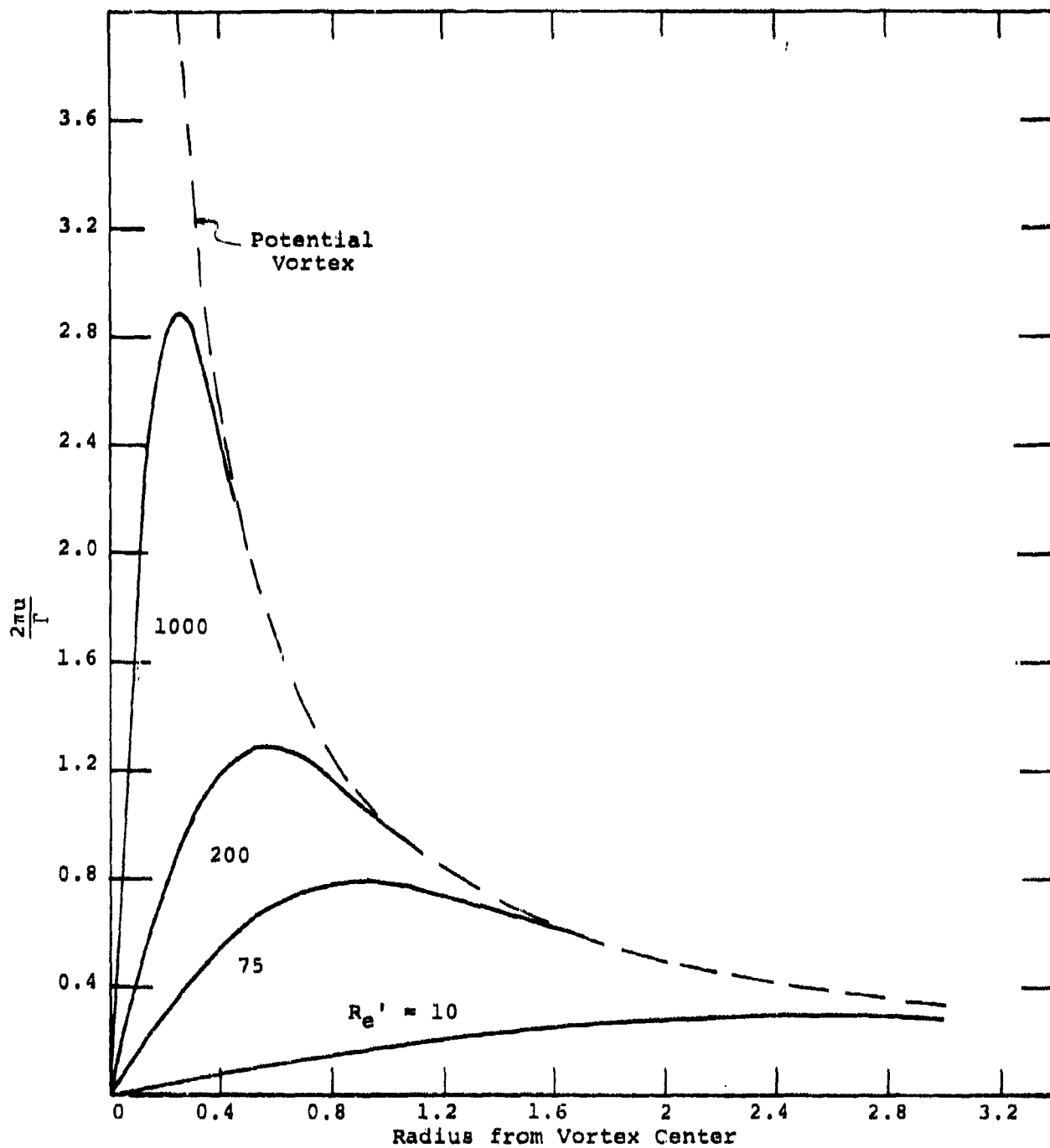
Figure 12. Viscous Vortex Model.

52

in the field. The combination of two vortices is carried out as follows.
The strength of the resulting vortex is

$$\Gamma_{1+2} = \Gamma_1 + \Gamma_2 \tag{60}$$

and the combined vortex is located at

$$y_{1+2} = \frac{|\Gamma_1|y_1 + |\Gamma_2|y_2}{|\Gamma_1| + |\Gamma_2|} \tag{61}$$

$$z_{1+2} = \frac{|\Gamma_1|z_1 + |\Gamma_2|z_2}{|\Gamma_1| + |\Gamma_2|} \tag{62}$$

The objective is to reduce the number of vortices without making an appreciable change in the flow field; in particular, without changing the induced flow field near the body surface.

In keeping with this objective, certain rules are considered in combining vortices. Only vortices of like sign are combined, and some effort is made to combine vortices which have about the same age. The vortices to be combined should be in close proximity. A rule of thumb is that vortices that are closer than the two most recently shed vortices are candidates for combination. Generally, combination of vortices is not considered until a large field of vorticity is developed, and then a second combination is not carried out until some point far downstream where another large field of vorticity has developed.

Combination of vortices has not been restricted to vortex pairs, and if three or four vortices are within the specified spacing, they are combined. In the present form of the program, the combination of adjacent vortices is done automatically with logic in the program. The user of the program may select the distance within which the two (or more) vortices must lie to be combined, and this distance is input to the program.

4.1.7 Forces and moments

The forces and moments on the body can be computed using two different procedures. The first is an integration of the pressure distribution around the body, and the second is a combination of slender-body theory and the vortex-impulse theorem. Since the pressures are calculated for purposes of determining the location of separation, the pressure integration method is used.

At a specified station on the body, the normal-force coefficient on a Δx length of the body is

$$c_n = \frac{\Delta n}{qd} = \frac{1}{d} \int_0^{2\pi} C_p \, r_0 \, \cos \beta \, d\beta \tag{63}$$

The total normal force on the body is

$$C_N = \frac{N}{qS} = \frac{d}{S} \int_0^{\ell} c_n \, dx \tag{64}$$

The pitching-moment coefficent is

$$C_m = \frac{M}{qS\ell_{ref}} = \frac{d}{S} \int_0^{\ell} c_n \left(\frac{x_m - x}{\ell_{ref}} \right) dx \tag{65}$$

and the center of pressure is located at

$$\frac{x_{CP_N}}{\ell_{ref}} = \frac{x_m}{\ell_{ref}} - \frac{C_m}{C_N} \tag{66}$$

Similarly, the side force on an element of length Δx is

$$c_y = \frac{\Delta s}{qd} = \frac{-1}{d} \int_0^{2\pi} C_p \, r_0 \, \sin \beta \, d\beta \tag{67}$$

The total side force is

$$C_y = \frac{Y}{qS} = \frac{d}{S} \int_0^{\ell} c_y \, dx \tag{68}$$

The yawing-moment coefficient is

$$C_n = - \frac{d}{S} \int_0^{\ell} c_y \left(\frac{x_m - x}{\ell_{ref}} \right) dx \tag{69}$$

and the center of pressure of the side force is located at

$$\frac{x_{CP_y}}{\ell_{ref}} = \frac{C_n}{C_y} + \frac{x_m}{\ell_{ref}} \tag{70}$$

54

4.2 Results

A number of results were obtained on circular or near-circular bodies to check the methods. These include two-dimensional and three-dimensional configurations. Typical results are described in this section.

4.2.1 Two-dimensional cases

The discussion in the previous section pointed out the dependence of the predicted results on the separation location. Since the predicted separation points are obtained from two different criterion by Stratford for either laminar or turbulent flow, the validity of these criterion and the manner in which they are applied were investigated.

The Stratford laminar separation criterion was applied to the potential pressure distributions on two, two-dimensional cylinders. The first cylinder is circular in cross section and the second is a 2:1 ellipse in cross section. Applying the Startford criterion from the minimum pressure point without including a false origin results in separation points as noted on Figure 13. When the false origin is included, the predicted separation points move upstream approximately 2^O of arc on the circular cylinder (Figure 13a) and approximately 3° of arc on the ellipse (Figure 13b). The computed separation points taken from reference 13 (Figure 12.11) are about 2^O of arc upstream of these latter Stratford results.

Next, Stratford's turbulent separation criterion was applied to a two-dimensional circular cylinder from reference 14. A measured pressure distribution indicated separated flow on the back side of the cylinder. The measured pressure distribution was extrapolated through the separated region to approximate a potential pressure distribution for use in the Stratford criterion. The criterion indicated separation ($F_g = 0.40$) at $\beta = 100^O$. As noted in reference 14, separation was predicted to occur at $\beta = 101^O$ and separation was observed at $\beta = 110^O$.

4.2.2 Three-Dimensional cases

The Stratford turbulent separation criterion was applied to an ogive-cylinder at $\alpha = 20^O$ (ref. 15). Using the measured pressure distribution at an axial station on the cylinder 6 diameters aft of the nose, which indicated separation at $\beta = 120^O$, the Stratford factor was computed through the separation point. The value at separation was $F_g = 0.127$ which is approximately equal to 0.37 sin α_c. This result tends to verify the suggested modification of the separation factor by the sine of the angle of attack, as shown in equation (48).
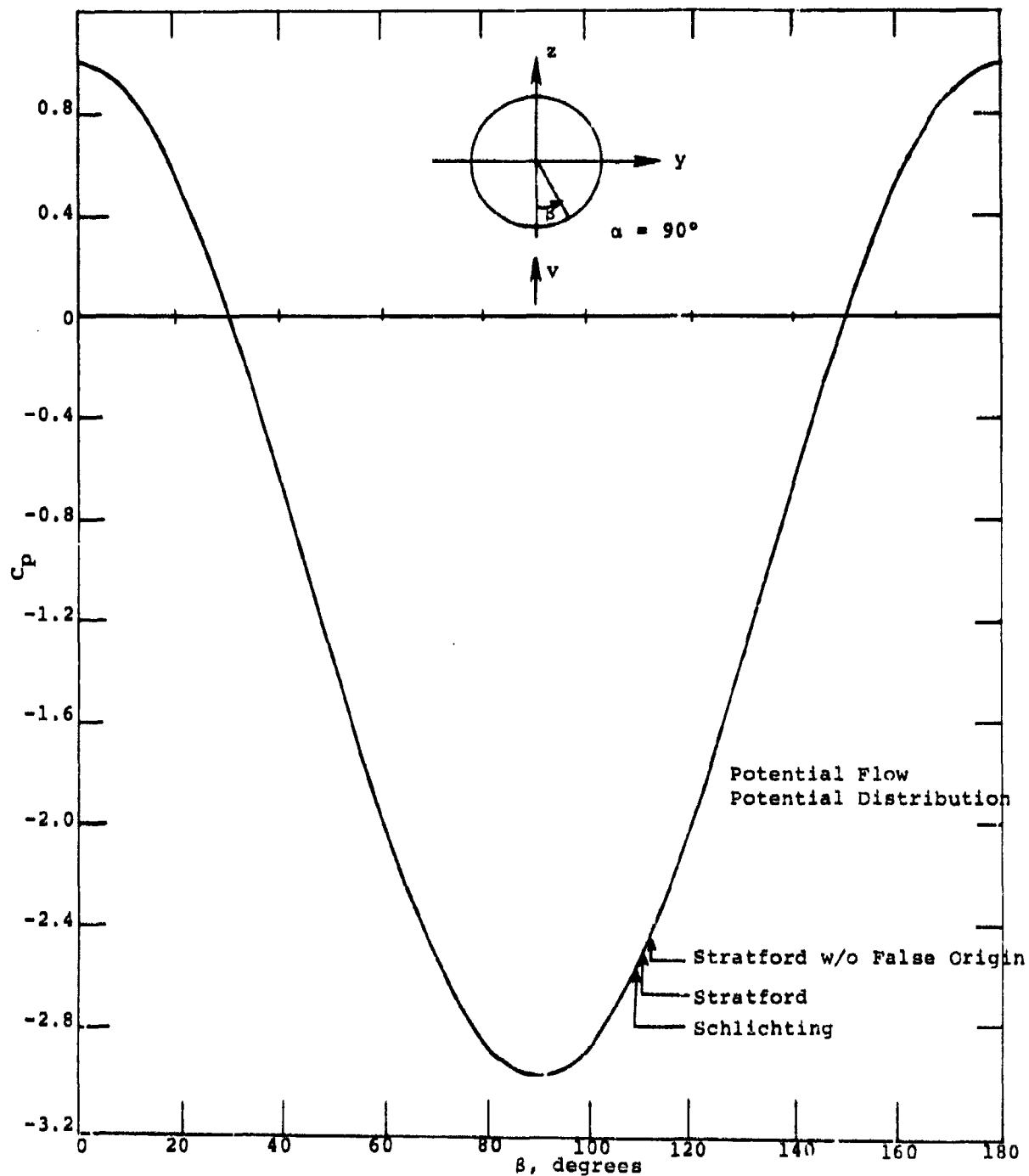
Figure 13. Comparison of Stratford's Laminar Separation Criterion
with Approximate Solution of Laminar Boundary Layer Equation.
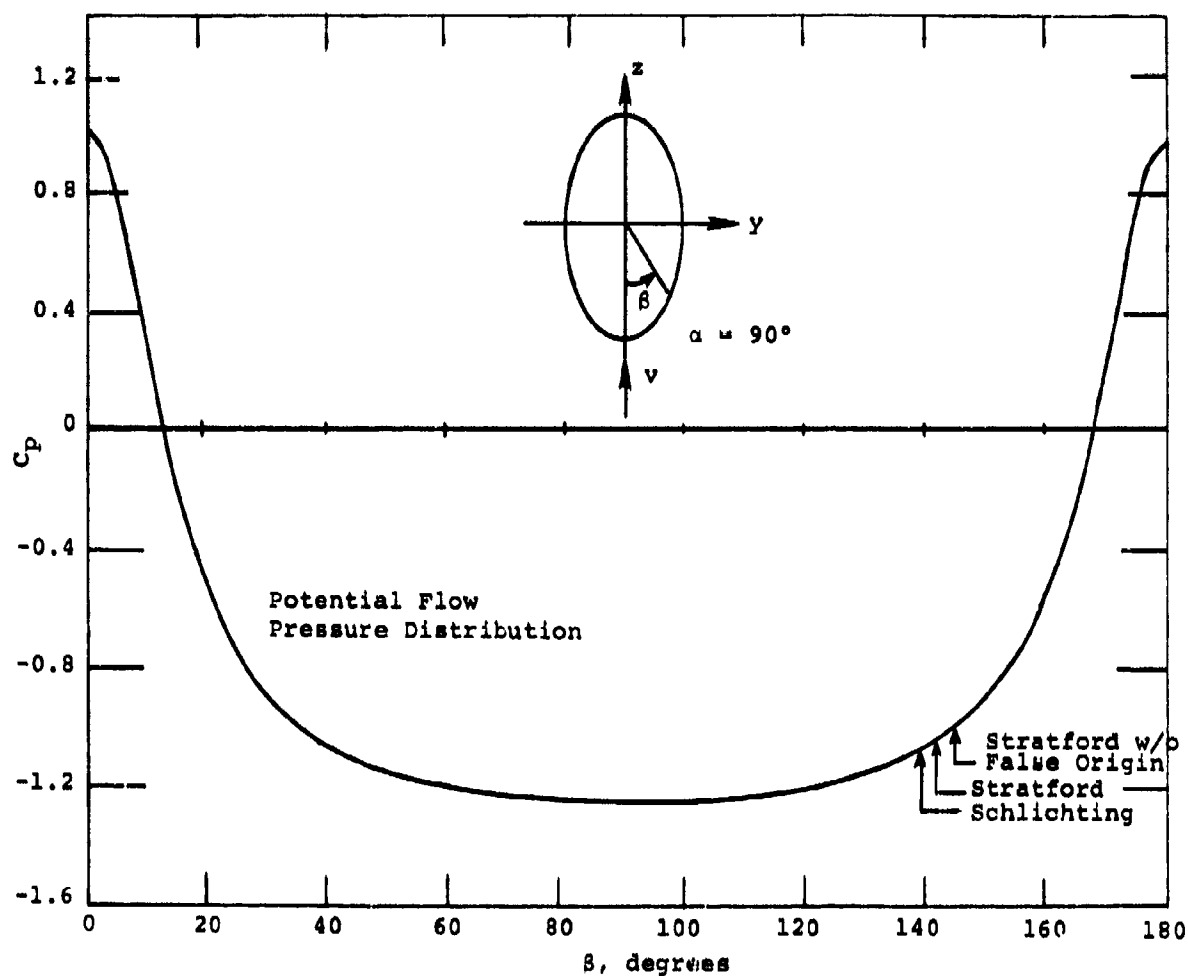a) Circle

Figure 13.   Comparison of Stratford's Laminar Separation Criterion
with Approximate Solution of Laminar Boundary Layer Equation.
b) 2:1 Ellipse

57

The prediction method was applied to the three-dimensional case of
the ogive-cylinder of reference 15 to evaluate pressure distributions,
vortex positions, and loads. The configuration has a circular cross sec-
tion and a three-caliber ogive nose followed by a 7.7-caliber cylindrical
afterbody. The calculations were made for an angle of attack of 20° and
a free stream Reynolds number based on diameter of 4.4×10^5.

The predicted pressure distributions at two axial stations on the
body are compared with measured pressure distributions in Figure 14. The
agreement near the nose is excellent. It should be noted that, in this
region, the "unsteady" portion of the predicted pressure coefficient has
a large effect on the predicted pressure distribution; therefore, the good
agreement exhibited near the nose indicates that the chosen approach for
predicting the unsteady part is reasonable. The agreement between measured
and predicted pressure distributions on the cylindrical section of the body
is not as good as nearer the nose. The irregular behavior in the predicted
curve near $\beta = 160^\circ$ is caused by interference from shed vortices. The
lack of a corresponding dip in the data may indicate that the shed vortices
are not allowed to diffuse at the correct rate. The predicted results were
obtained assuming laminar separation at $F_s = 0.025$.

The comparison on vortex position is shown in Figure 15 at a station
7.5 diameters aft of the nose. The right side of the figure shows the
positions of the individual vortices shed from the separation line along
the body. The left side shows the predicted center of vorticity, together
with a measured value. The two are in reasonably good agreement.

Figure 16 shows the results for section normal force coefficient.
There is little vortex-induced effect on the ogive nose, and the load in
this region is primarily due to the expanding nose cross section. The
load distribution on the cylindrical portion of the body is due entirely
to separation. The predicted values are generally low except for the
first 2 calibers of length behind the shoulder.

Finally, the prediction method was applied to an ogive-cylinder for
which laser velocimeter data are available to compare velocity fields in
the separated region over the body. The tests were conducted in the Ames
Research Center 7- by 10-foot low speed tunnel on a six inch diameter model
having a 3.5 caliber ogive nose and a 3.5 caliber cylindrical afterbody.
The freestream Reynolds number based on diameter was 1.9×10^5. The test
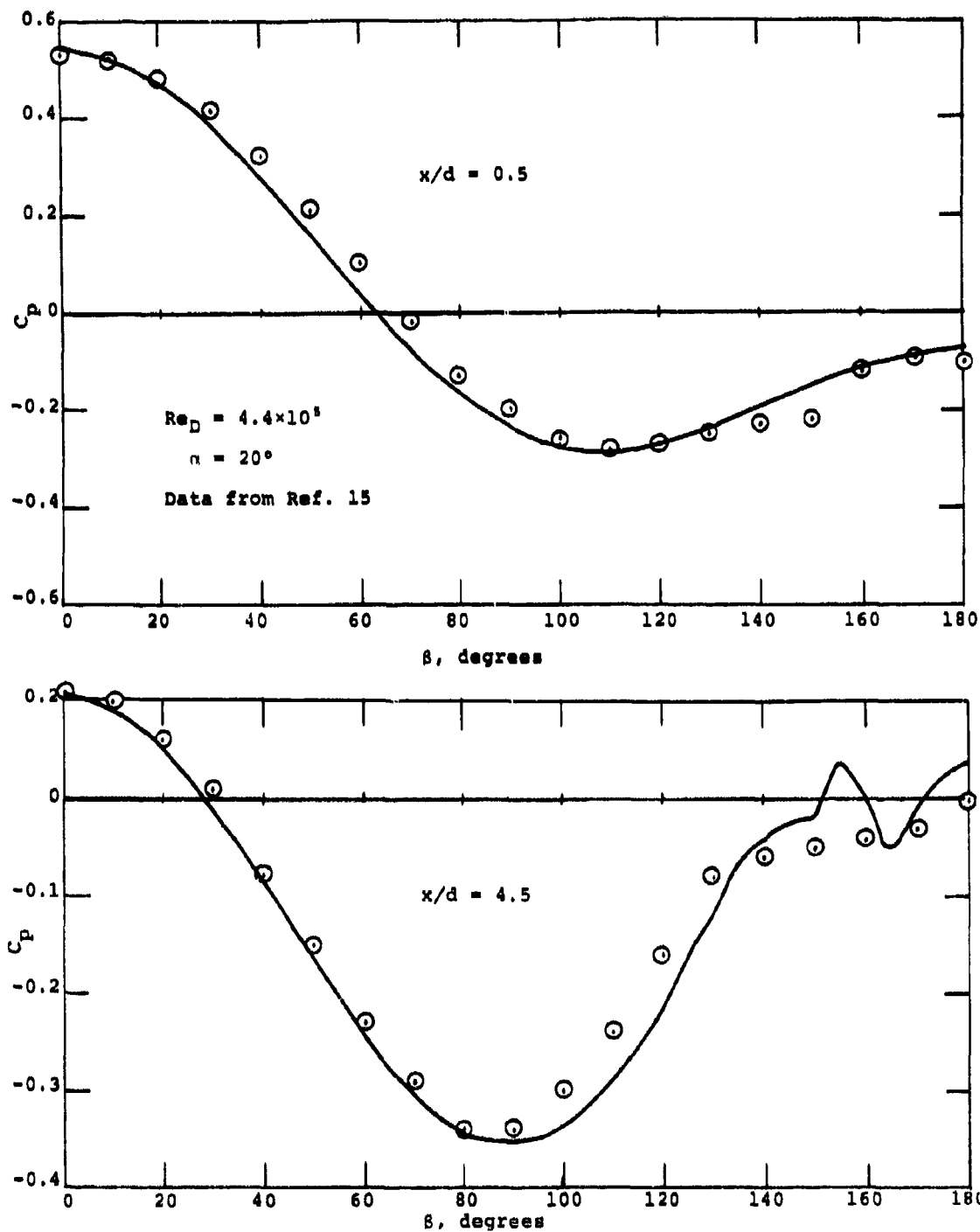conditions and results are described in reference 16.

58

Figure 14. Comparison of Predicted and Measured Pressure Distribution on an Ogive Cylinder at Two Axial Stations.
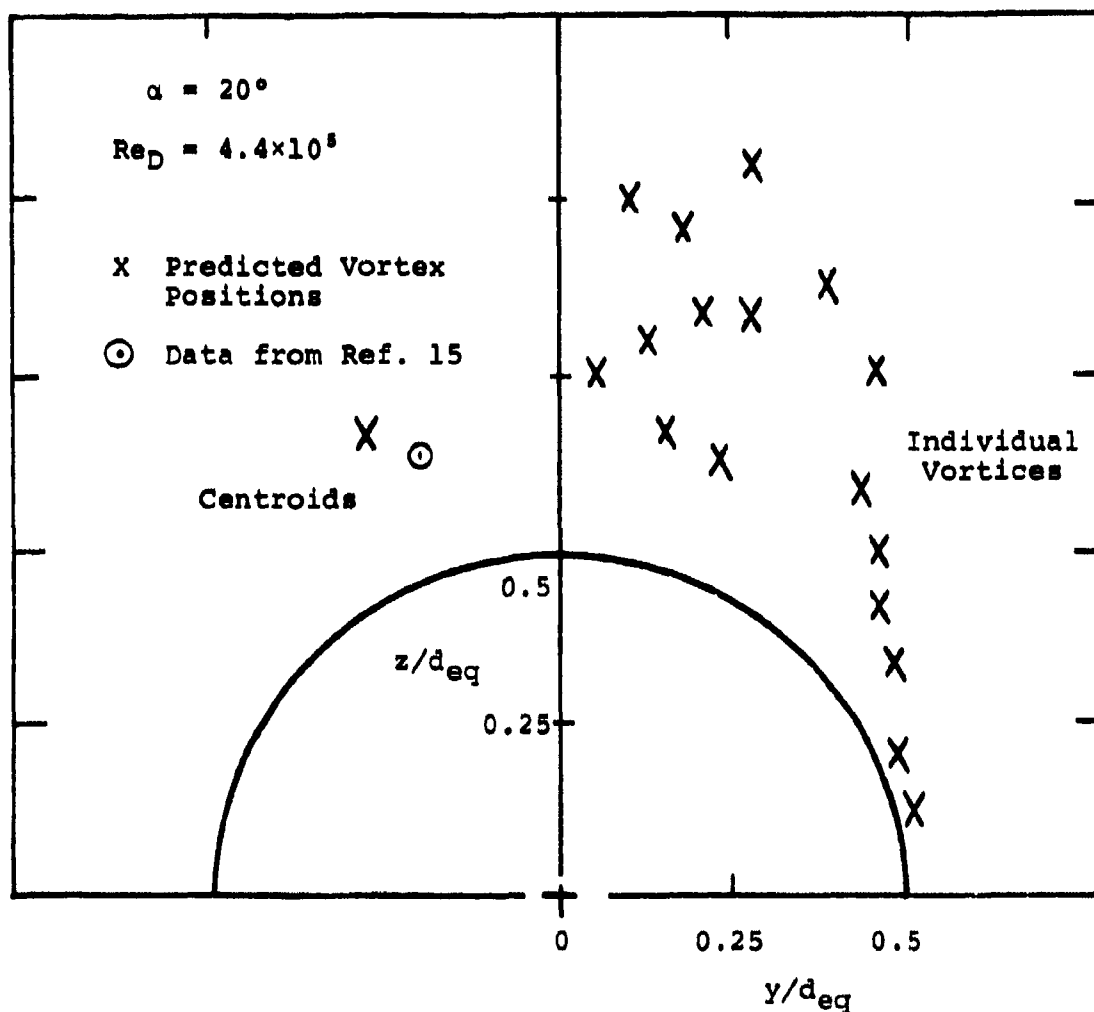
Figure 15. Predicted and Measured Vortex Positions on an Ogive-Cylinder at $x/d_{eq} = 7.5$.
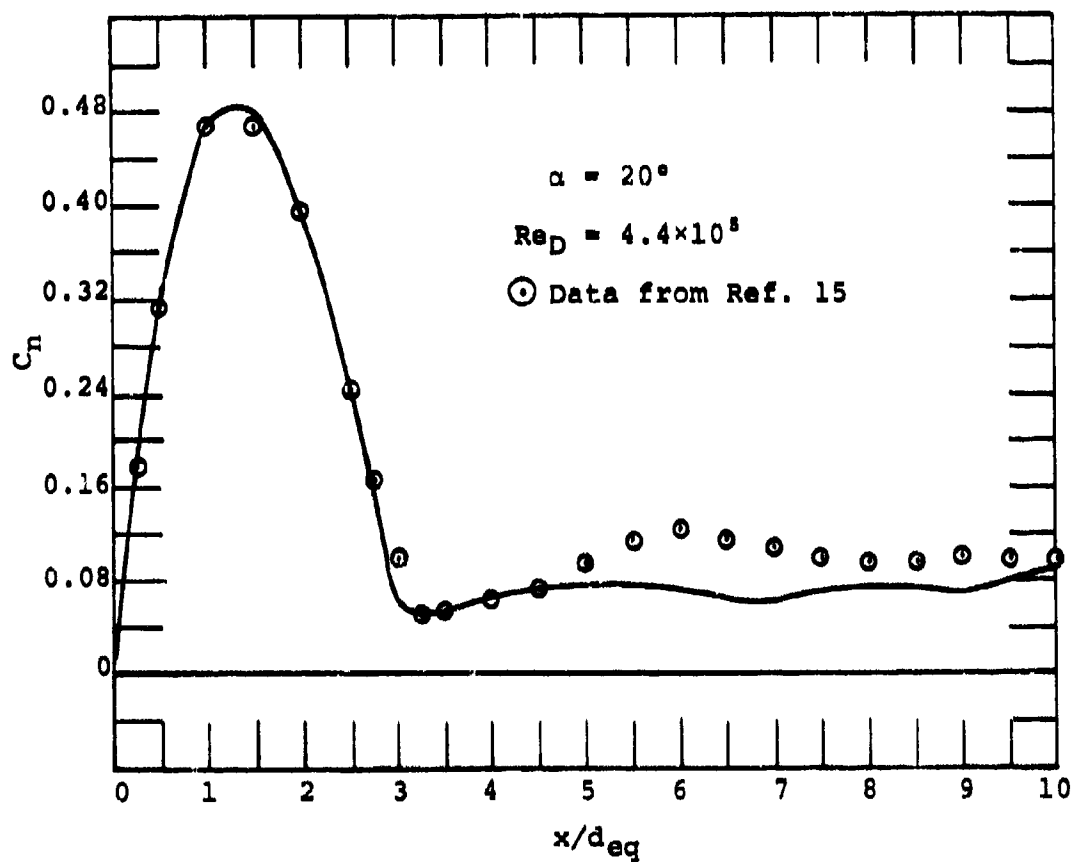
Figure 16.   Predicted and Measured Section Normal
Force Coefficient on an Ogive-Cylinder.

The theory was applied to this case using the turbulent separation criterion and the $\sin\alpha$ factor as given in equation (48). In order to introduce an asymmetric disturbance into the calculation, the separation points on the flanks of the body over the initial 12 percent of the model length were shifted 2 degrees. Downstream of the 12 percent length station, the separation points as calculated were used.

Results for the downwash distribution at the 70 percent axial station are presented in Figures 17 and 18. The angle of attack is 37.5 degrees. Figure 17 shows predicted and measured velocities along a horizontal line slightly above the body surface and Figure 18 shows results along the vertical line passing through the body center. The theory in both cases agrees quite well with the data. The vortex system is clearly asymmetric at this station, and the theory shows the asymmetric features.
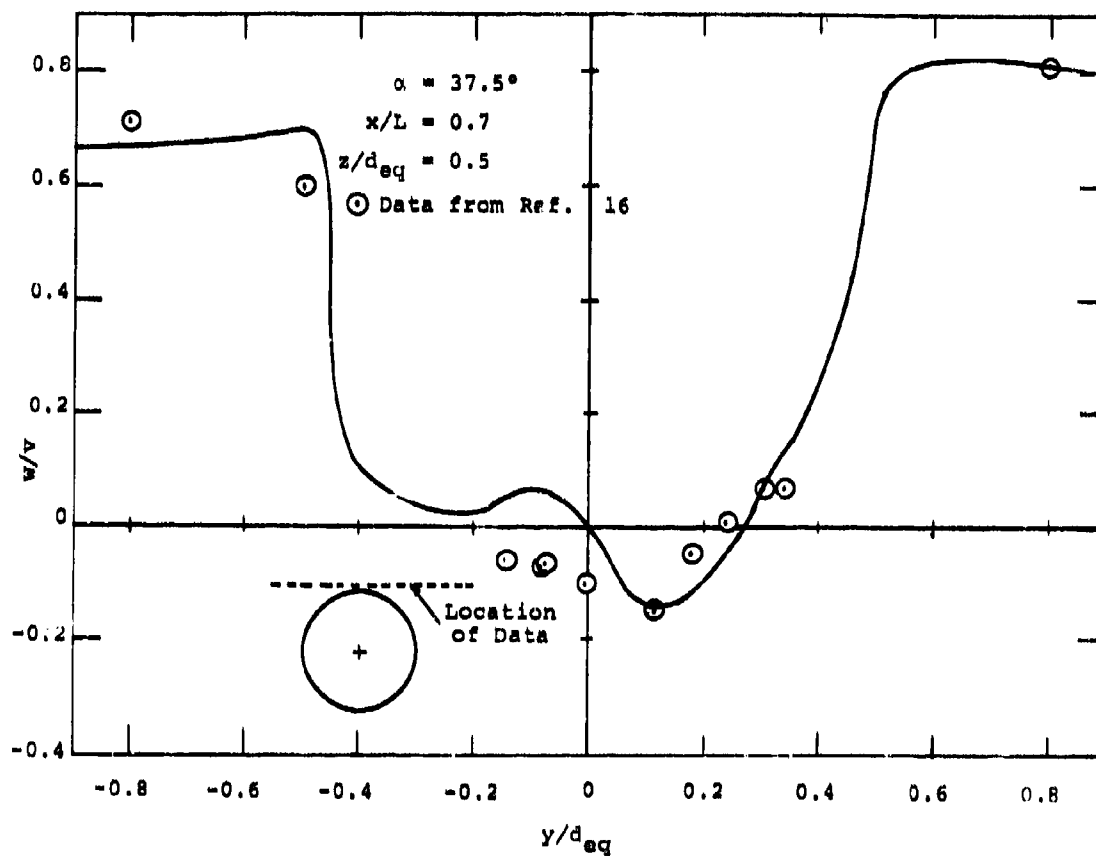
Figure 17. Predicted and Measured Downwash Distribution Along a
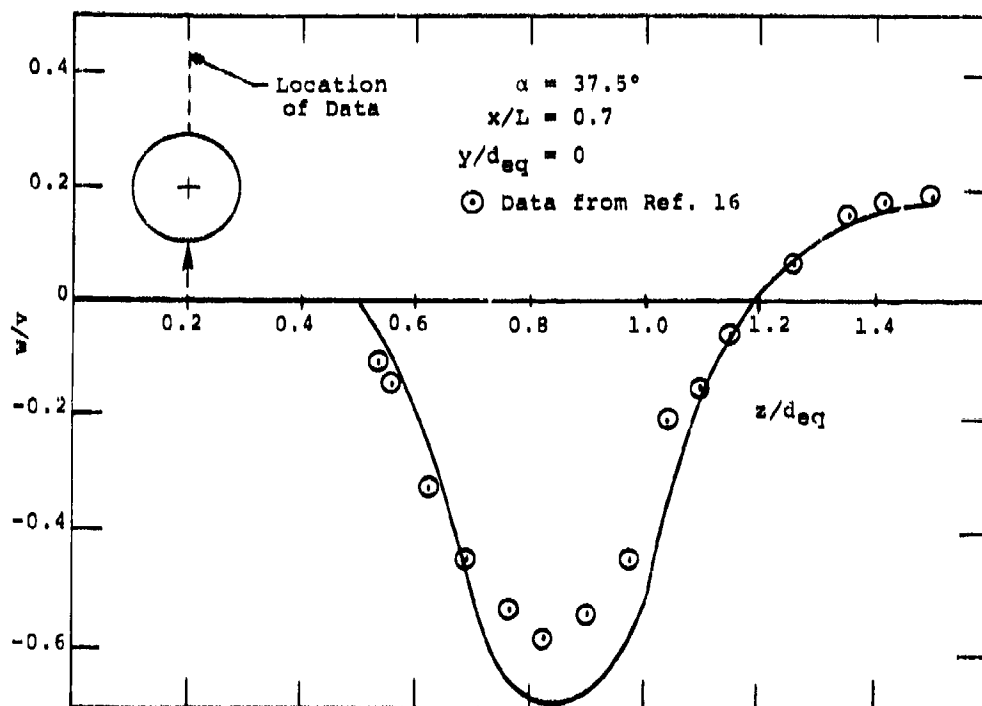Horizontal Line Just Above the Body of an Ogive-Cylinder
at Low Speed.

63

Figure 18.   Predicted and Measured Downwash Distribution Along the
Vertical Axis Above the Body of an Ogive-Cylinder at Low Speed.

5. DISCUSSION OF RESULTS

Several areas of the investigation described in previous sections are worthy of discussion. These have to do with the quantitative and qualitative observations of the water tunnel tests, comparisons between theory and various sets of data made possible by the coordinated tests, and observations on the status of the nose vortex shedding analysis made possible by the comparison.

5.1 Nose Shape

One shape feature that is suggested by the water-tunnel data as being important for tailoring lateral loads on aircraft noses at high angles of attack is that which affects the height of the vortices above the body. The F-5 nose has a vortex pair that lays relatively close to the body at angles of attack up to 40 degrees. If this is the case, then as the nose is sideslipped and the vortices move laterally with respect to the body, the windward vortex is over the center of the body and can be affected by the presence of the cockpit canopy. The influence could take the form of lateral and vertical deflection of the core and possibly a change in axial pressure gradient which could change the vorticity distribution in the crossflow plane. The latter is suggested by the difference in appearance of the vortices between Figures 6 and 7, which appear to be quite concentrated at 30 degrees angle of attack and more diffuse over the canopy area at 40 degrees angle.

The general height level of the vortices appears to be affected by "bluntness" of the nose and the cross section shape. The vortices on the V/STOL nose (the "bluntest") tend to lie very close to the surface and, in fact, lie within the lateral confines of the nose (as seen in a top view) at 10 degrees of sideslip. The vortices on the F-5 nose also tend to lie close to the top surface (within a body radius) to the highest angle of attack tested, although the leeward vortex at angle of sideslip is well outboard of the flank of the body. At the other extreme, the elliptical ogive with major axis vertical has a large vertical displacement of one vortex from the top body surface, which would prevent any interaction of that vortex with a canopy, for instance.

Of the three "research" shapes tested, the elliptical ogive with major axis horizontal showed the highest angle of attack for the onset of lateral effects and the least sensitivity to Reynolds number effects. This shape tends to fix the location of separation more than the others

65

because of the high circumferential pressure gradients on the flanks, so the variations in separation location which cause lateral forces to occur should be least of the shapes tested. The forward portion of the F-5 nose has this shape, which might be another factor in its unusual force characteristics.

5.2 Vortex Positions and Strengths

The tests of the V/STOL configuration in both the LRC V/STOL tunnel and the water tunnel permit comparisons of vortex positions with the theory described in Section 4 and comparisons of the LRC results with theory for vortex strength. The theory was applied to the V/STOL shape using the noncircular body model for 35 degrees angle of attack and both 0 and 10 degrees of sideslip. For zero sideslip, an asymmetric disturbance to the separation line location was introduced, as discussed in Section 4.2. The vortex center locations from the LRC flow field data were estimated by plotting radial and circumferential variations of velocity components and interpolating for changes in sign of the cross-flow plane velocity components.

The results of the comparison for vortex positions are shown in Figure 19 for Body Station 51.9, which is at the intersection of the strake leading edge with the body. For the case of zero sideslip, the agreement is reasonably good. Both sets of data and the theory indicate little asymmetry in position. At 10 degrees sideslip, the differences are greater, with the measured vortex positions closer to the body than the predicted values. One of the uncertainties in making this comparison is the problem of characterizing a distribution of vorticity by its "center", rather than using the vorticity distribution itself or induced velocities.

The influence of Reynolds number on vortex positions could not be determined with these measurements. Turbulent separation was used with the theory of Section 4, and the predicted separation locations on the body are insensitive to Reynolds number. The NEAR water-tunnel results showed considerable variation in forces and moments with a Reynolds number change from 0.95×10^5 to 3.3×10^5, but no vortex position data could be obtained at the higher tunnel velocity due to limitations on the instrumentation. The LRC force data show little influence of Reynolds number from 2.3×10^5 to 7.4×10^5, but no vortex position data were obtained at the lower Reynolds number.

66
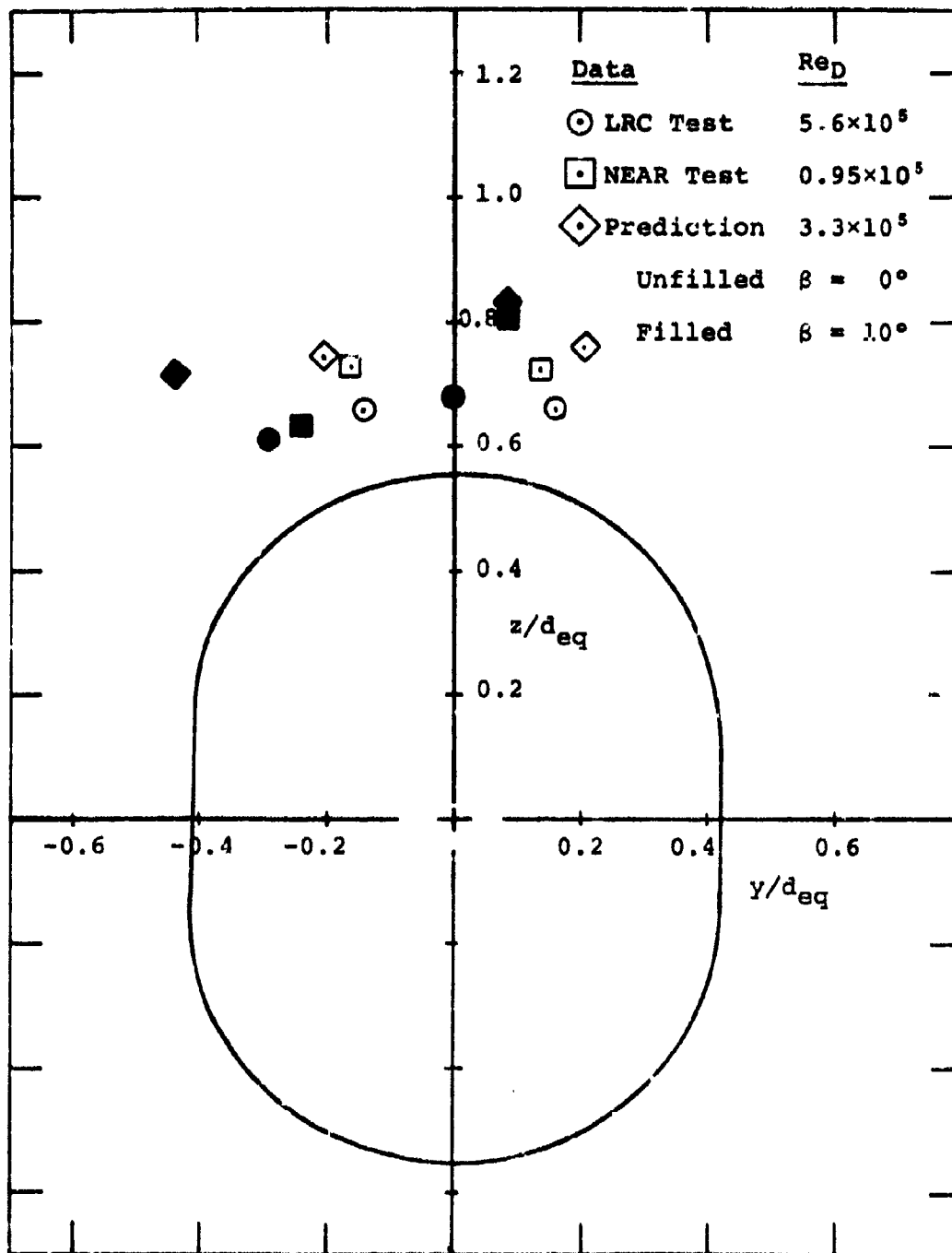
Figure 19. Vortex Positions on V/STOL Body at BS 51.9
for α = 35°.

67

With the velocity components known at grid points such as was
obtained in the LRC tests, it is possible to perform contour integrations
to obtain circulation strengths for comparison with the predicted values.
A first approximation to such a calculation was made for the case dis-
cussed above, with 10 degrees of sideslip, by using two contours to
encompass the grid of velocity measurements, with the boundary between
the left and right contours a straight radial line along the plane con-
taining the crossflow vector (the fifth radial line of points left of
the vertical axis in Figure A-17). From examination of Figure A-17, it
is clear that while the outer part of this common boundary is aligned
with the crossflow velocity vectors and is thus a reasonable boundary
between positive and negative circulation, the inner part is not. As a
result, one would expect the magnitudes of both the vortex strengths to
be somewhat low with this computation. The results for vortex strength
(Γ/V) and the predicted values are:

	LRC Test	Predicted
right vortex	+0.520	+0.636
left vortex	-0.342	-0.644

The predicted values show little difference in magnitude, whereas the
measured values show a considerable difference, right to left. A more
detailed integration, particularly near the body, will probably show an
increase in the magnitudes of the measured vortex strengths, and this is
planned in subsequent analysis of this data.

It is planned that the contour integration process will be automated
so better contours can be taken, and contours of different size can be
taken to determine the distribution of vorticity.

5.3 Forces and Moments

It is possible to compare predicted forces and moments on the V/STOL
nose with those measured in the NEAR water tunnel tests. This was done
for the 35 degree angle of attack case at both zero and 10 degrees of
sideslip, with the following results. The predicted values were obtained
using a turbulent separation criteria for separation location.

68

	Water Tunnel		Predicted
	$Re_D = 0.9 \times 10^5$	3.4×10^5	3.3×10^5
$\beta = 0°$			
c_N	1.79	1.24	1.09
c_Y	0.68	0.04-0.08	0.092
c_m	1.17	1.08	1.60
c_n	-0.58	0.01-0.10	0.12
$\beta = 10°$			
c_N	1.56	1.14	1.02
c_Y	-1.39	-0.64	-0.57
c_m	1.28	1.18	1.74
c_n	0.52	-0.23	-0.08

In general, the predicted values agree reasonably well with the measured values for the comparable Reynolds number, except for pitching moment. The reason for the disagreement on C_m is not known. It does not have much separation-induced content, so the problem may lie with the force balance readings or calibration.

6. CONCLUDING REMARKS

As part of a continuing study on spin entry of high speed aircraft, a series of analytical and experimental investigations have been performed, directed principally at vortex separation from aircraft nose shapes at high angles of attack and small sideslip. The asymmetric separation characteristics of the nose have been identified as an important factor in the lateral aerodynamic forces and moments that are developed on many fighter-bomber aircraft at incipient spin entry conditions. Understanding and prediction of the nose flow characteristics will lead to an ability to calculate the lateral loads on complete configurations.

A significant aspect of the investigation is the strong correlation between the analytical work and the execution of the tests to obtain data to check the methods and provide understanding of the flow over real nose shapes. In particular, it is essential to obtain flow visualization and flow field data under identical conditions as force and moment data to understand the phenomena.

The comparisons between the asymmetric vortex shedding theory and the various sets of data have shown reasonably good correlation considering the complexity of the flow phenomena and the fact that few results are available from previous work on vortex shedding from noncircular bodies.

It is necessary to do additional work on the nose vortex shedding method before it can be incorporated into an overall computation method for a complete aircraft. The separation criteria need to be examined in more detail and compared with additional data, particularly for three dimensional separation cases. The means of introducing asymmetric perturbations for cases of zero sideslip at high angles of attack need additional examination. Finally, there are considerably more comparisons and evaluations that should be done with the LRC and water-tunnel data to evaluate the vortex shedding analysis.

When reasonable confidence has been established in the prediction method, it would then be of great interest to evaluate systematically aircraft nose shapes to determine those characteristics which provide the least undesirable or perhaps favorable aerodynamic behavior. It should be possible to rationally design aerodynamic characteristics into a fighter-bomber aircraft to provide desirable high angle handling qualities.

REFERENCES

1. Spangler, S. B. and Nielsen, J. N.: Exploratory Study of Aerodynamic Loads on a Fighter-Bomber at Spin Entry. NEAR TR 87, May 1975.

2. Spangler, S. B. and Dillenius, M. F. E.: Investigation of Aerodynamic Loads at Spin Entry. Report ONR-CR212-225-2, 28 May 1976.

3. Gloss, B. B.: The Effect of Canard Leading-Edge Sweep and Dihedral Angle on the Longitudinal and Lateral Aerodynamic Characteristics of a Close-Coupled Canard-Wing Configuration. NASA TN D-7814, Dec. 1974.

4. Keener, E. R., Chapman, G. T., Cohen, L., and Taleghani, J.: Side Forces on Forebodies at High Angles of Attack and Mach Numbers from 0.1 to 0.7: Two Tangent Ogives, Paraboloid and Cone. NASA TM X-3489, Feb. 1977.

5. Grafton, S. B., Chambers, J. R., and Coe, P. L.: Wind-Tunnel Free-Flight Investigation of a Model of a Spin-Resistant Fighter Configuration. NASA TN D-7716, June 1974.

6. Marshall, F. J. and Deffenbaugh, F. D.: Separated Flow Over Bodies of Revolution Using an Unsteady Discrete-Vorticity Cross Wake. NASA CR-2414, June 1974.

7. Deffenbaugh, F. D. and Koerner, W. G.: Asymmetric Wake Development and Associated Side Force On Missiles at High Angles of Attack. AIAA Paper No. 76-364, July 1976.

8. Mendenhall, M. R. and Nielsen, J. N.: Effect of Symmetrical Vortex Shedding on the Longitudinal Aerodynamic Characteristics of Wing-Body Combinations. NASA CR-2473, Jan. 1975.

9. Jameson, A.: Iterative Solution of Transonic Flows Over Airfoils and Wings, Including Flows at Mach 1. Comm. Pure Appl. Math., vol. 27, 1974, pp. 283-309.

10. Goodwin, F. K., Nielsen, J. N., and Dillenius, M. F. E.: A Method for Predicting Three-Degree-of-Freedom Store Separation Trajectories at Speeds up to the Critical Speed. Technical Report AFFDL-TR-71-81, Oct. 1974.

11. Stratford, B. S.: The Prediction of Separation of the Turbulent Boundary Layer. J. of Fluid Mech., vol. 5, 1959, pp. 1-16.

12. Cebeci, T., Mosinskis, G. J., and Smith, A. M. O.: Calculation of
    Viscous Drag and Turbulent Boundary-Layer Separation on Two-Dimen-
    sional and Axisymmetric Bodies in Incompressible Flow. McDonnell
    Douglas Rept. No. MDC J0 973-01, Nov. 1970.

13. Schlichting, J.: Boundary-Layer Theory, 4th Edition. McGraw-Hill
    Book Co., 1960.

14. Wilcox, D. C. and Chambers, T. L.: Streamline Curvature Effects on
    Turbulent Boundary Layers. AIAA Paper No. 76-353, July 1976.

15. Tinling, B. E. and Allen, C. Q.: An Investigation of the Normal-
    Force and Vortex-Wake Characteristics of an Ogive-Cylinder Body at
    Subsonic Speeds. NASA TN D-1297, Apr. 1962.

16. Fidler, J. E., Schwind, R. G., and Nielsen, J. N.: An Investigation
    of Slender Body Wake Vortices. Nielsen Engineering & Research
    TR 108, Feb. 1976.

APPENDIX A

RESULTS OF LANGLEY RESEARCH CENTER
TESTS IN VSTOL TUNNEL
ON VSTOL FIGHTER MODEL
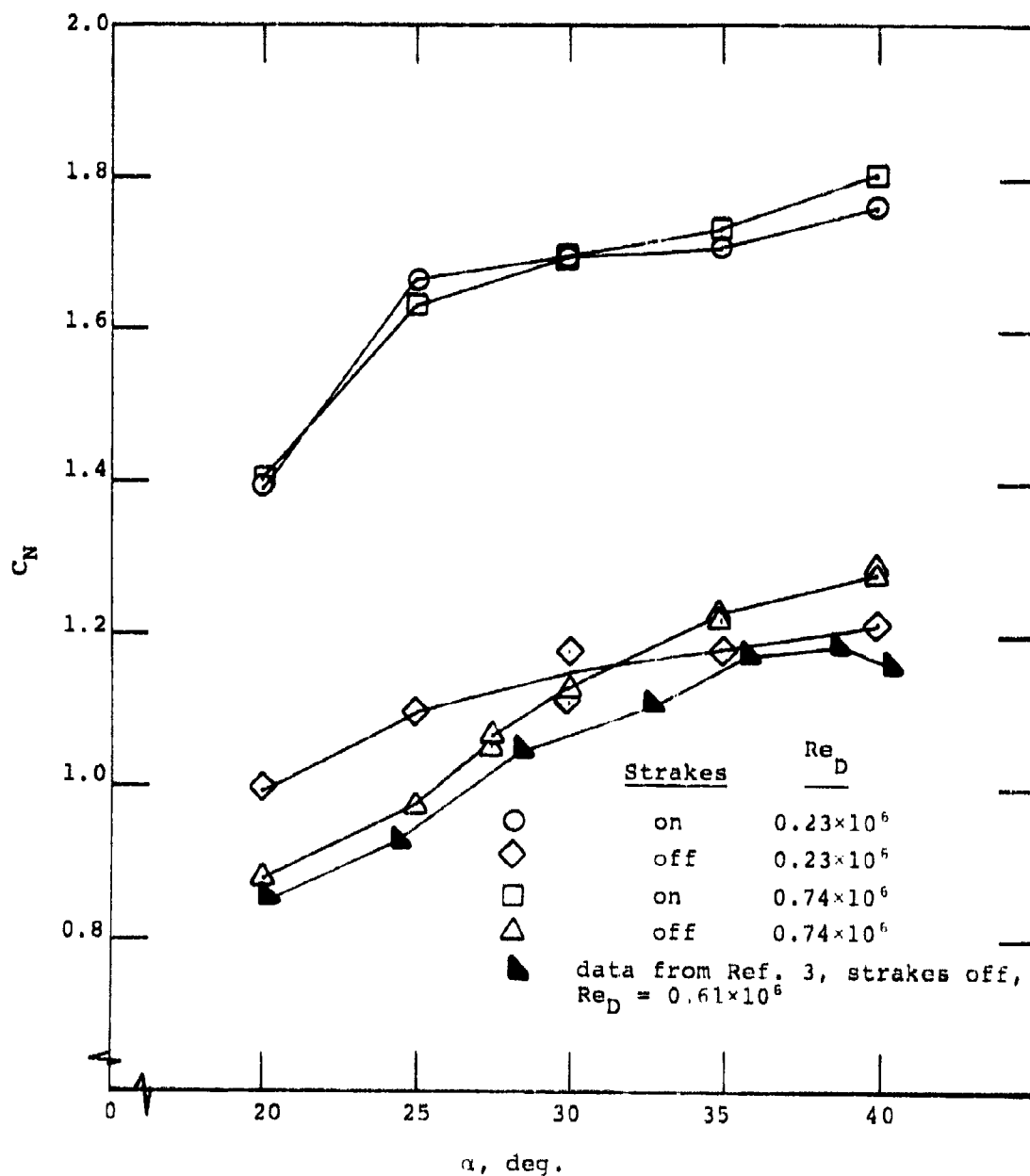
Figure A.1. Normal Force Variation with Angle of Attack
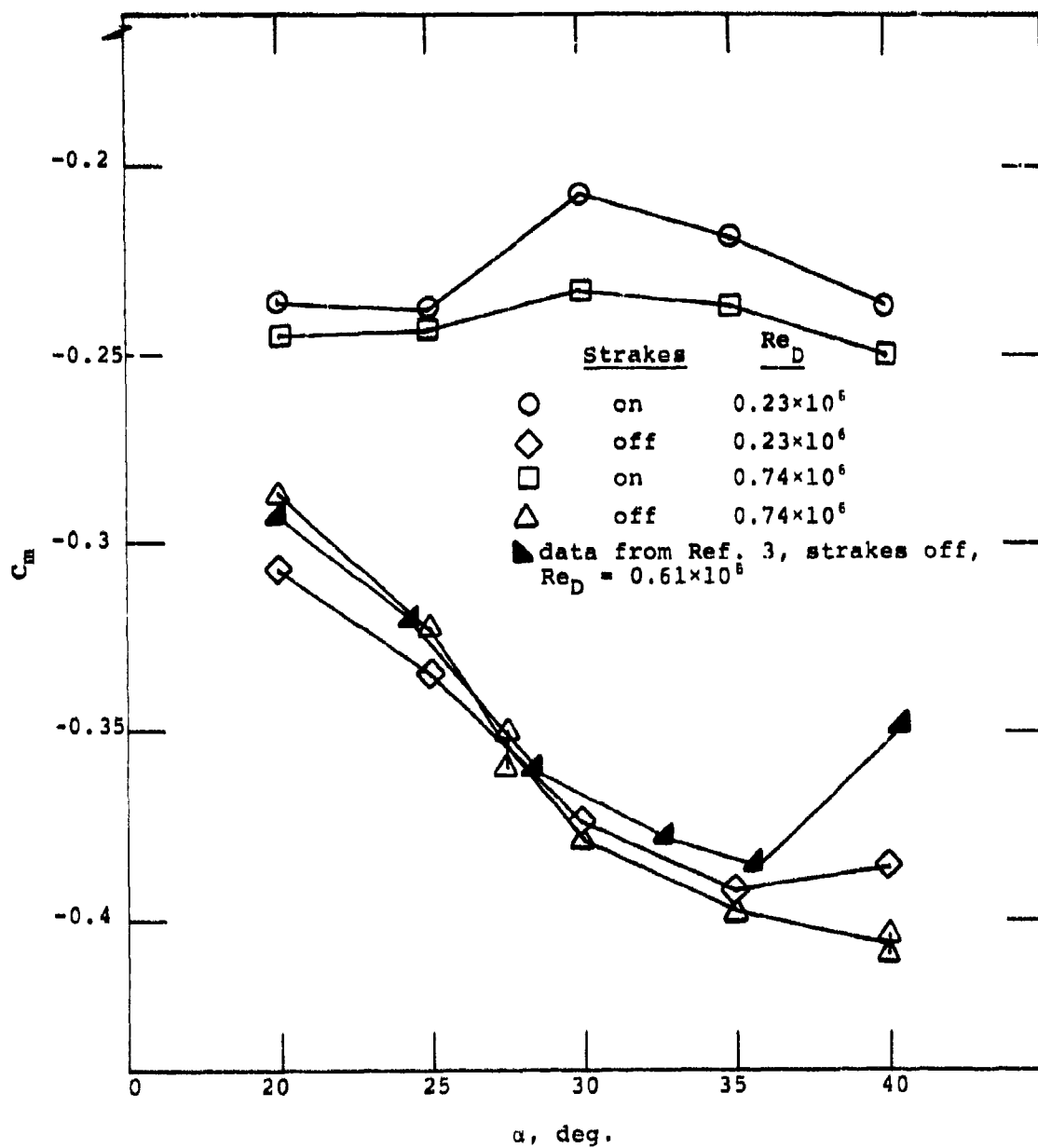at Zero Sideslip.

74

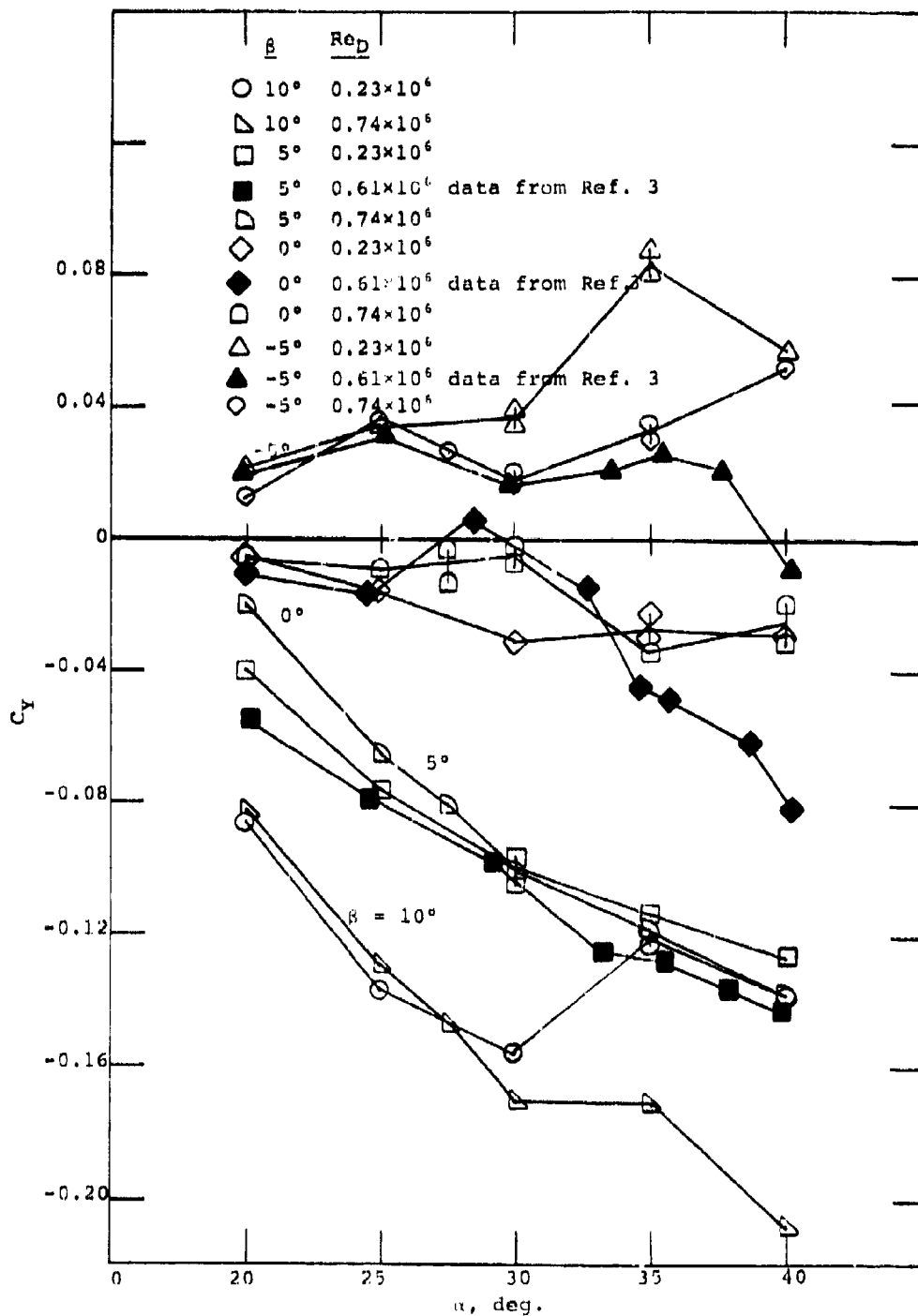Figure A.2. Pitching Moment Variation with Angle of Attack at Zero Sideslip.

Figure A.3. Side Force Variation with Angle of Attack
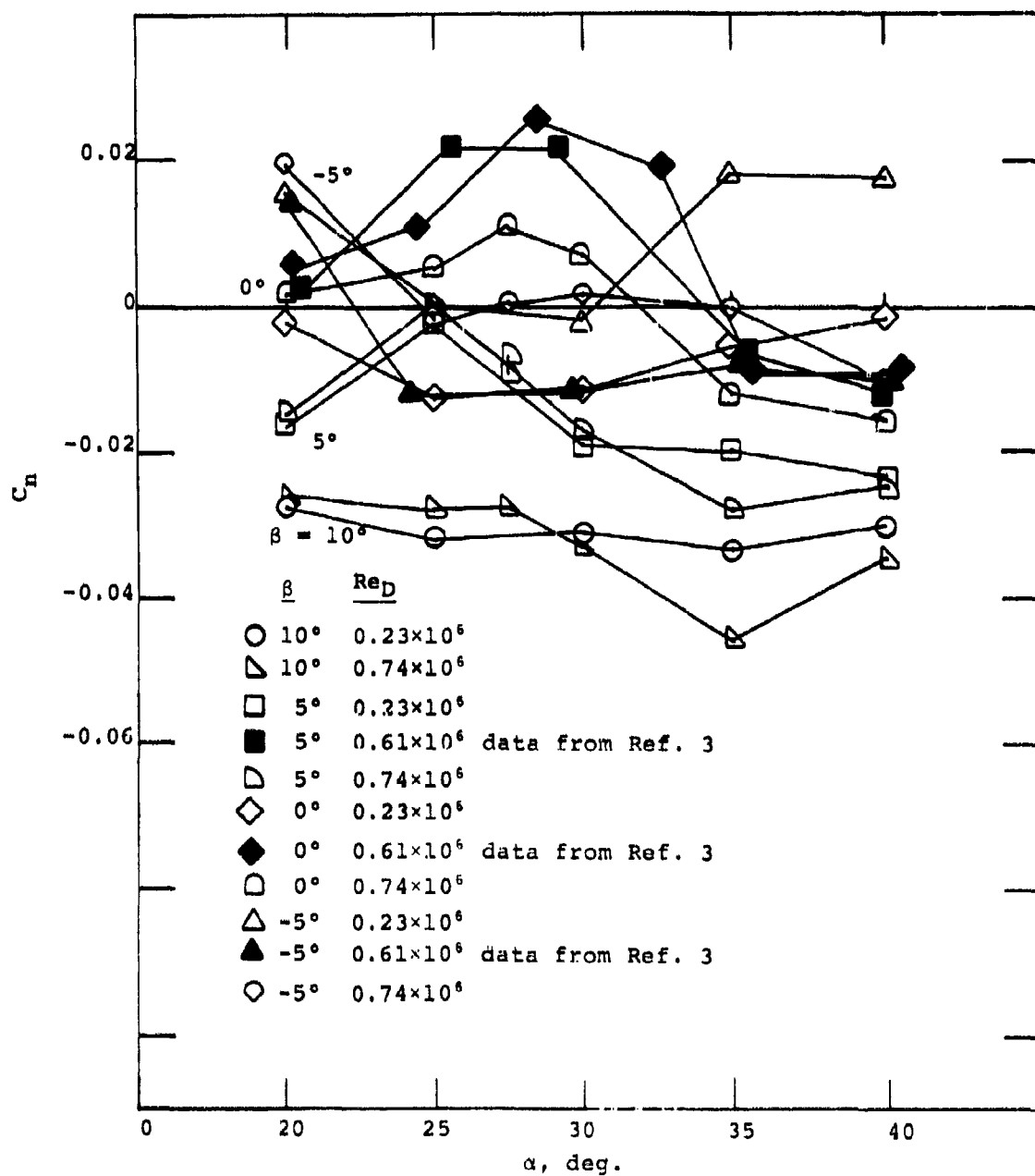for Four Sideslip Angles. Tail off, Strakes off.

76

Figure A.4.   Yawing Moment Variation with Angle of Attack
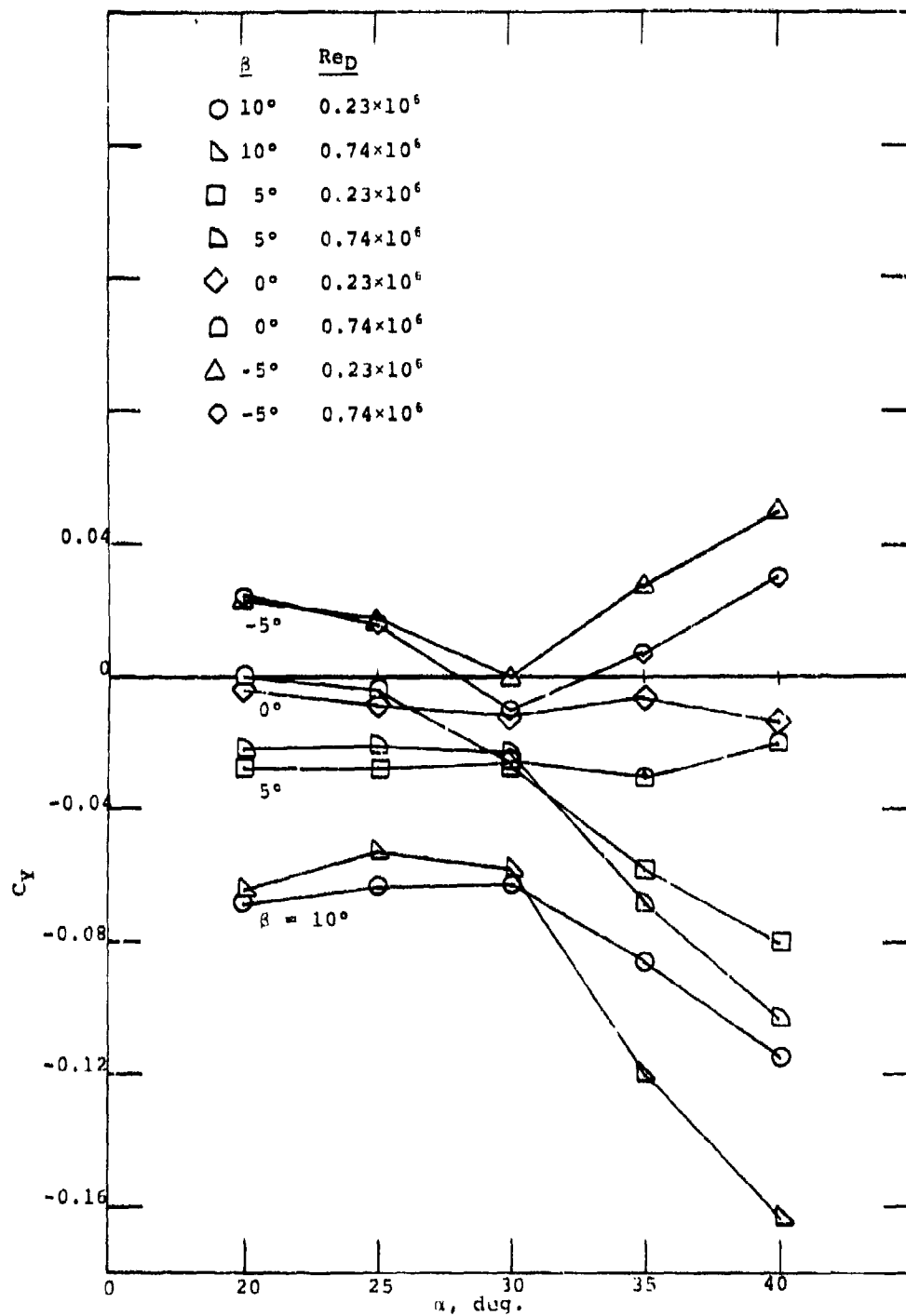for Four Sideslip Angles.   Tail off, Strakes off.

Figure A.5. Side Force Variation with Angle of Attack
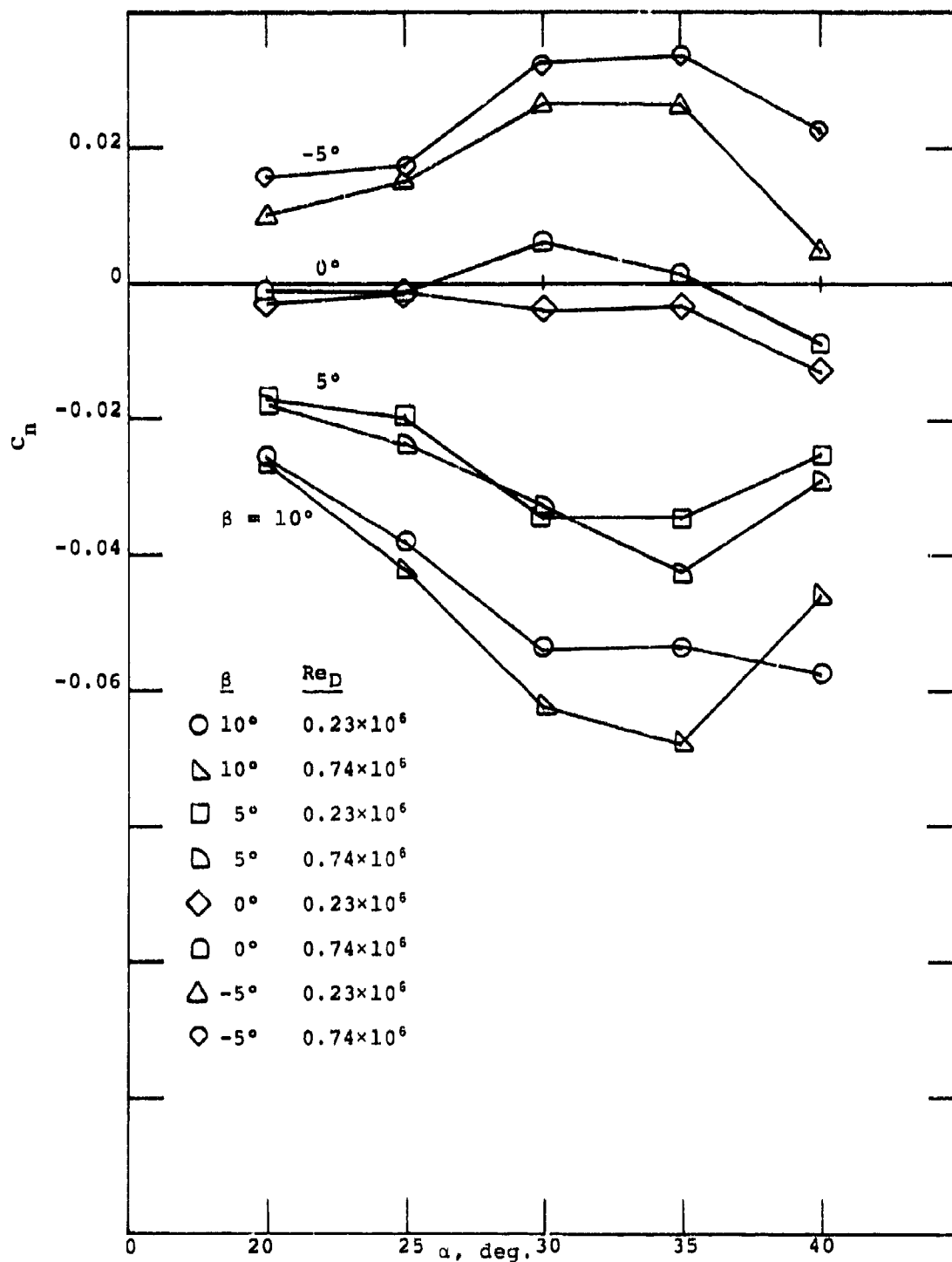for Four Sideslip Angles. Tail off, Strakes on.

Figure A.6.   Yawing Moment Variation with Angle of Attack for Four Sideslip Angles.   Tail off, Strakes on.
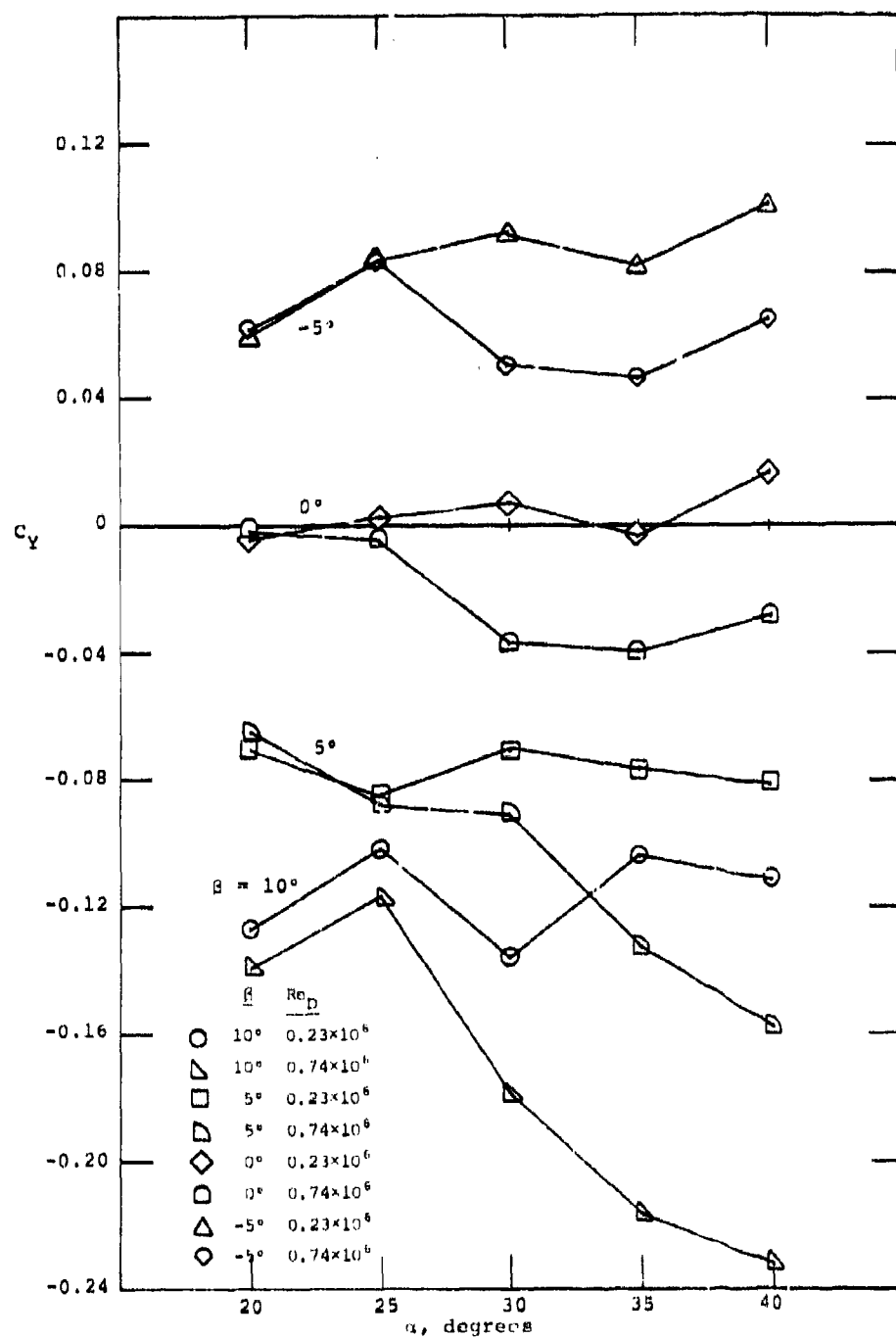
Figure A.7. Side Force Variation with Angle of Attack for
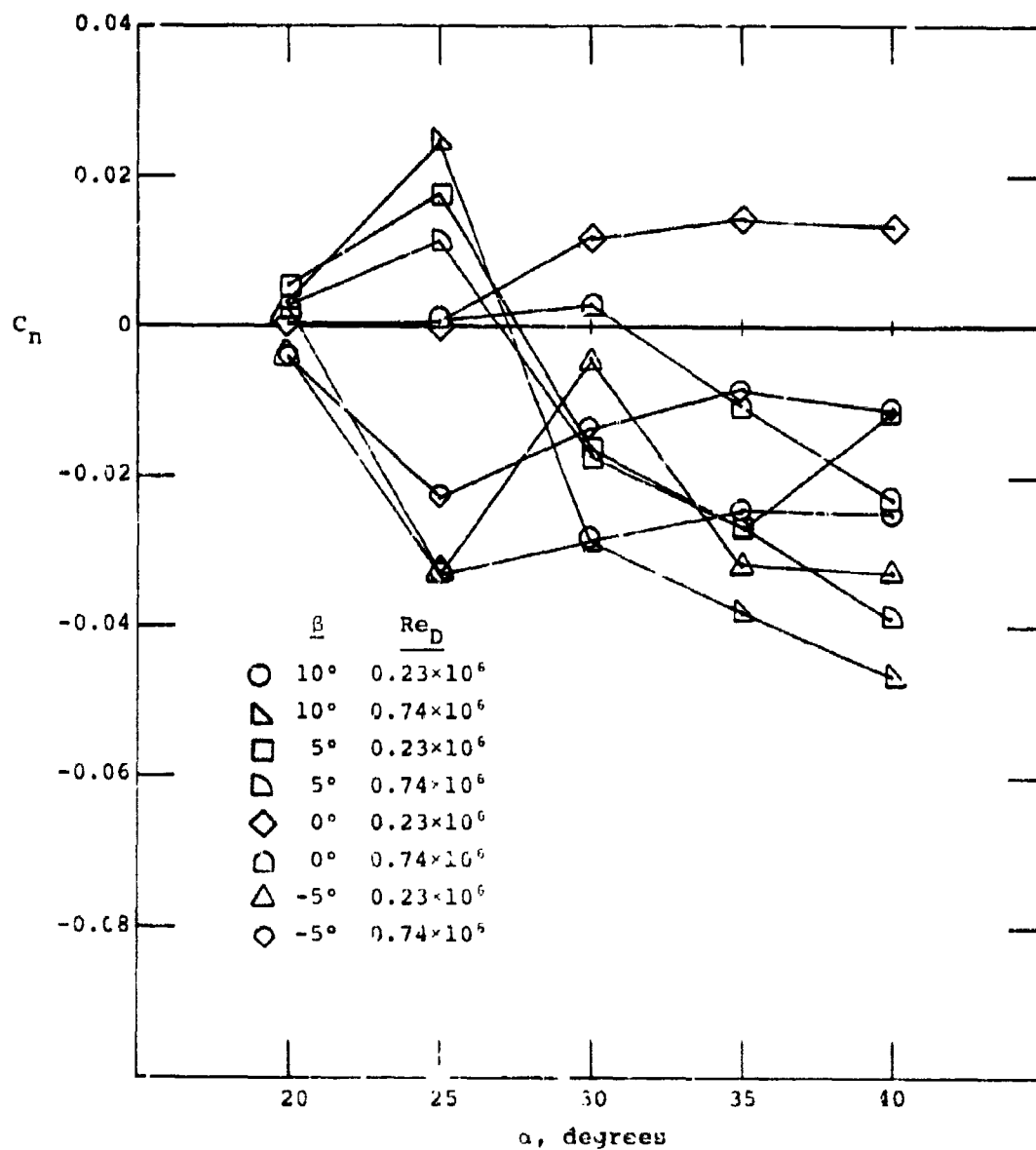Four Sideslip Angles. Tail On. Strakes Off.

Figure A.8.   Yawing Moment Variation with Angle of Attack for
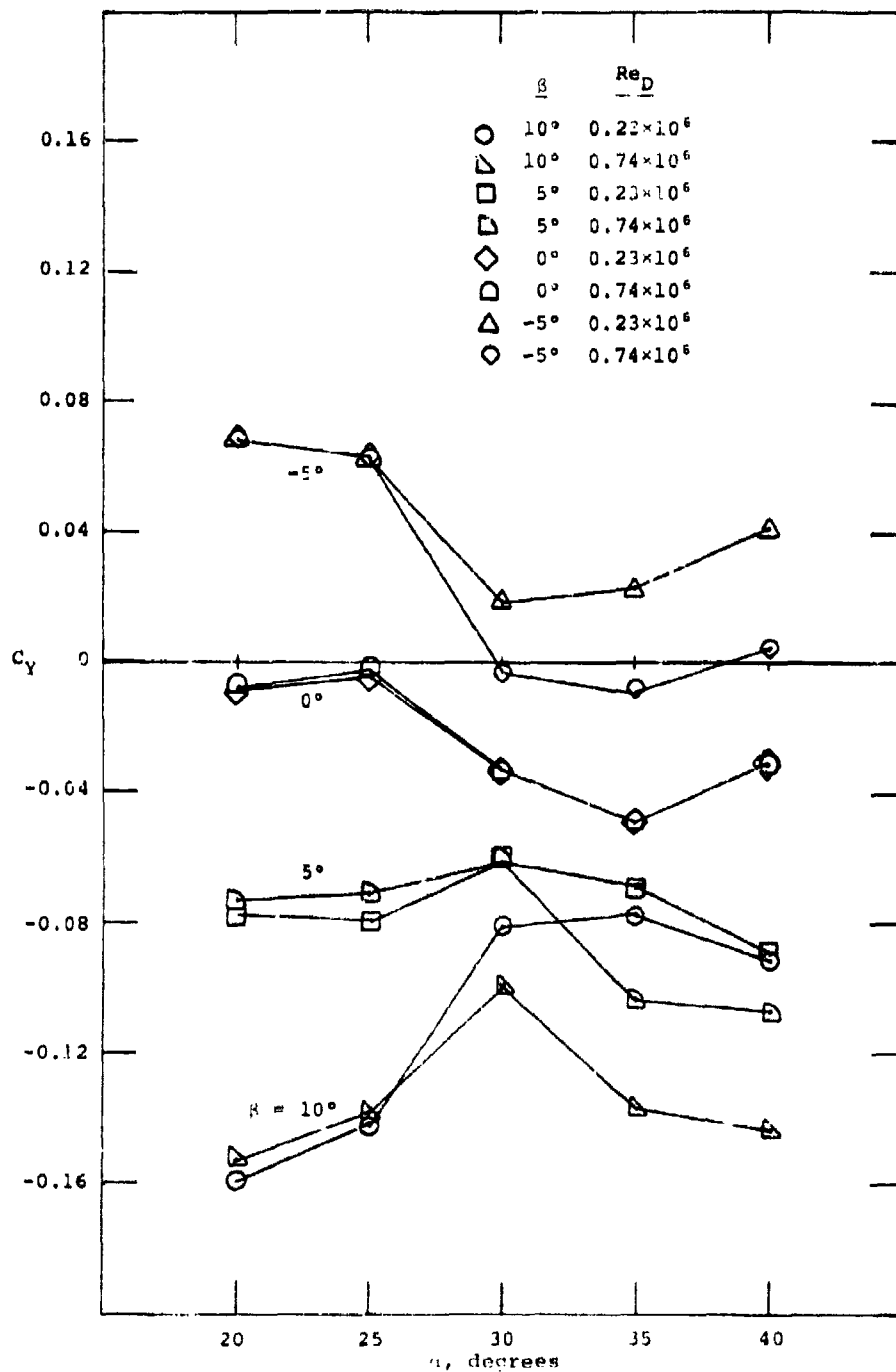Four Sideslip Angles. Tail On. Strakes Off.

Figure A.9. Side Force Variation with Angle of Attack for
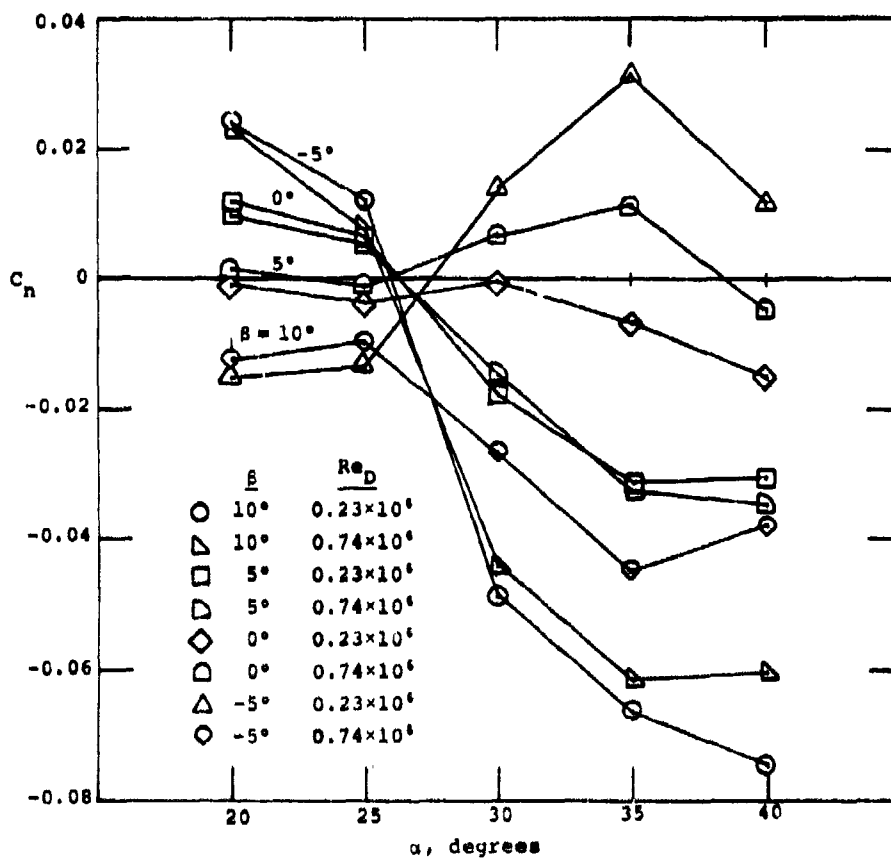Four Sideslip Angles. Tail On. Strakes On.

Figure A.10. Yawing Moment Variation with Angle of Attack for
Four Sideslip Angles. Tail On. Strakes On.

83

Figure A.11. Variation of Side Force, Yawing Moment and Rolling Moment with
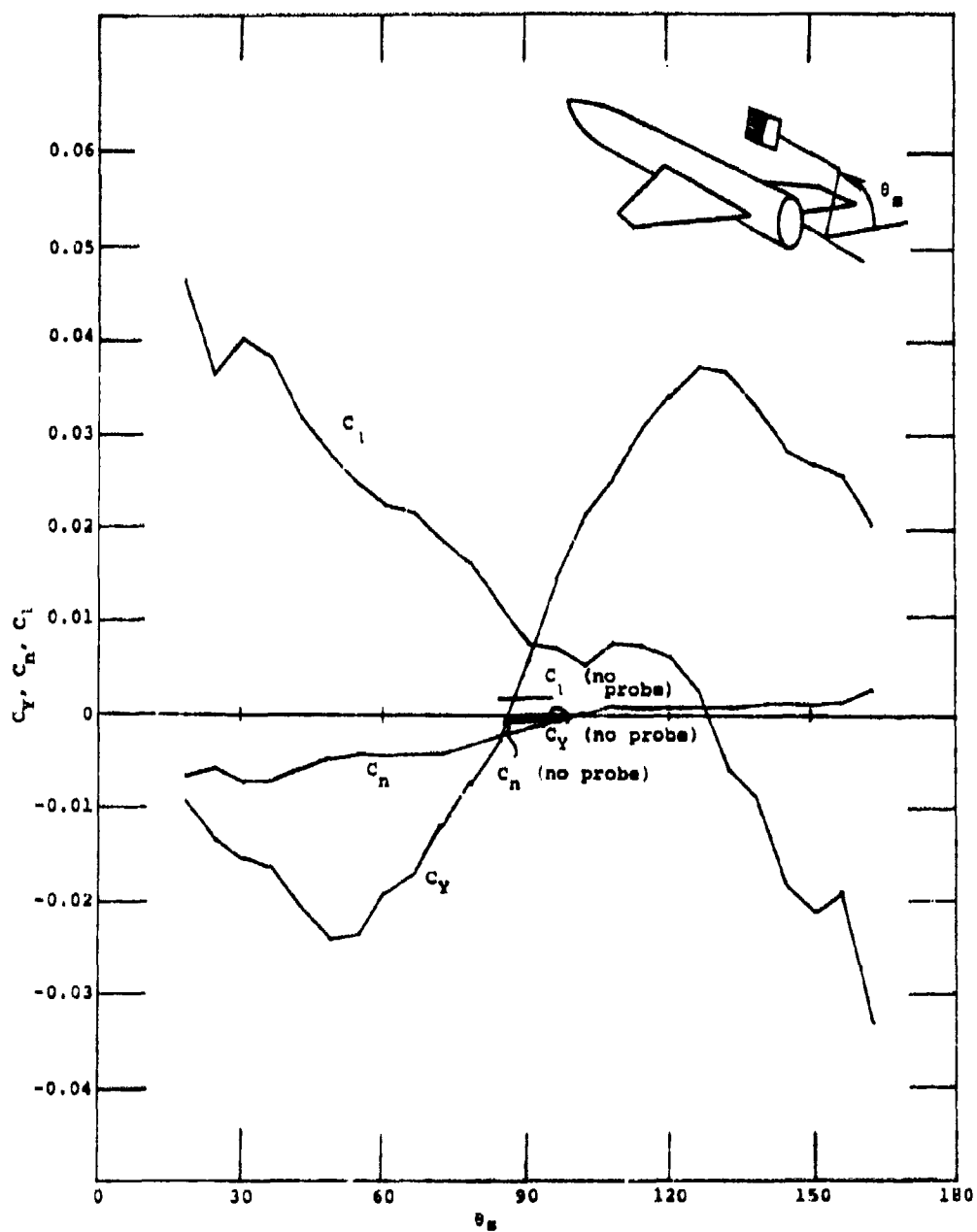Probe Position at α = 20°, β = 0°. Probe at BS 51.9 and
Innermost Radial Position.

84
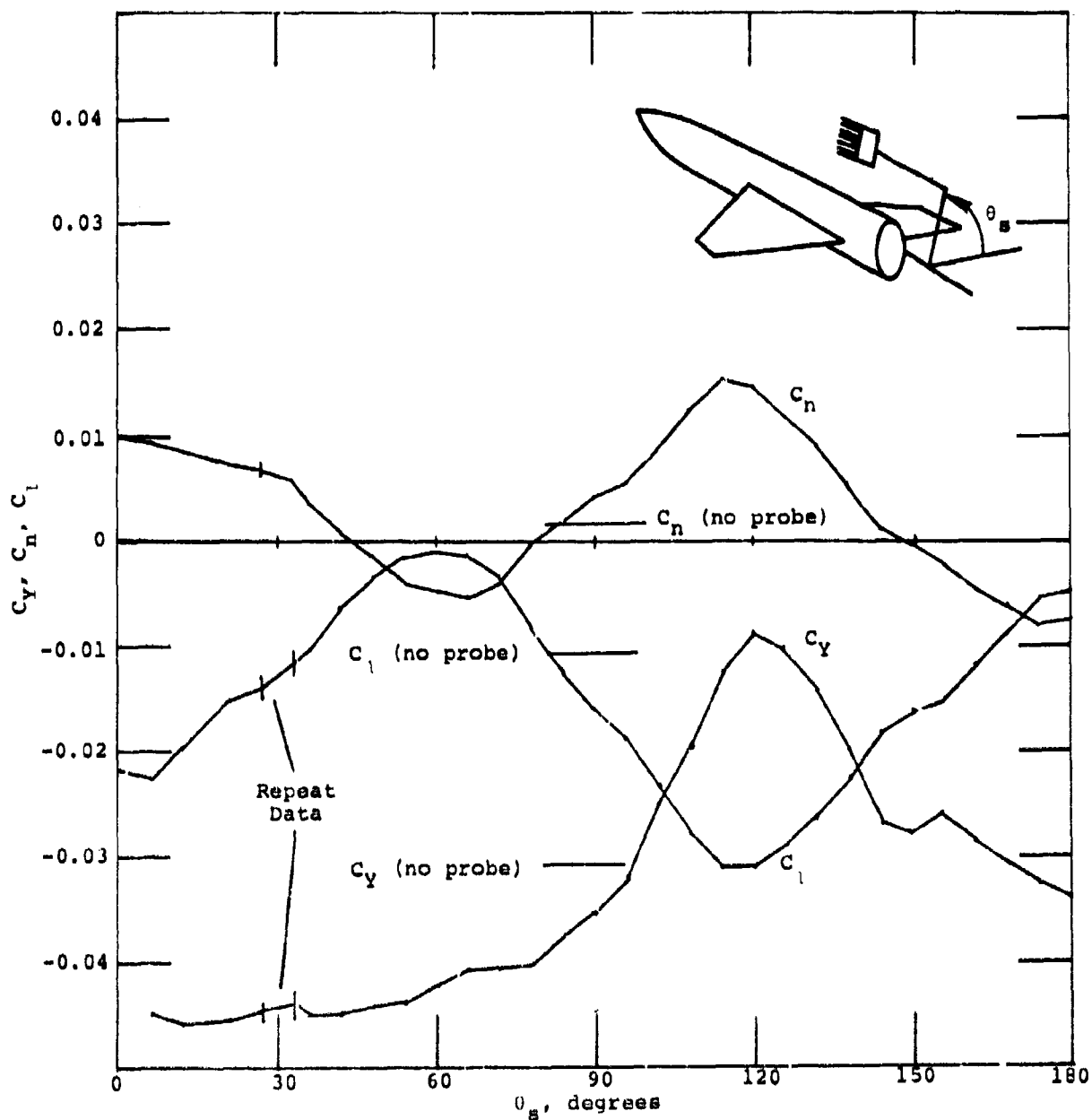
Figure A.12. Variation of Side Force, Yawing Moment and Rolling Moment with
Probe Position at $\alpha = 35°$, $\beta = 0°$. Probe at BS 98 and
Innermost Radial Position.

85

Figure A.13.   Comparison of Repeat Probe Velocity Data for Wing-Body
at BS 69, θ_g = 102°, Rake Radial Position 2.54 cm (1 inch)
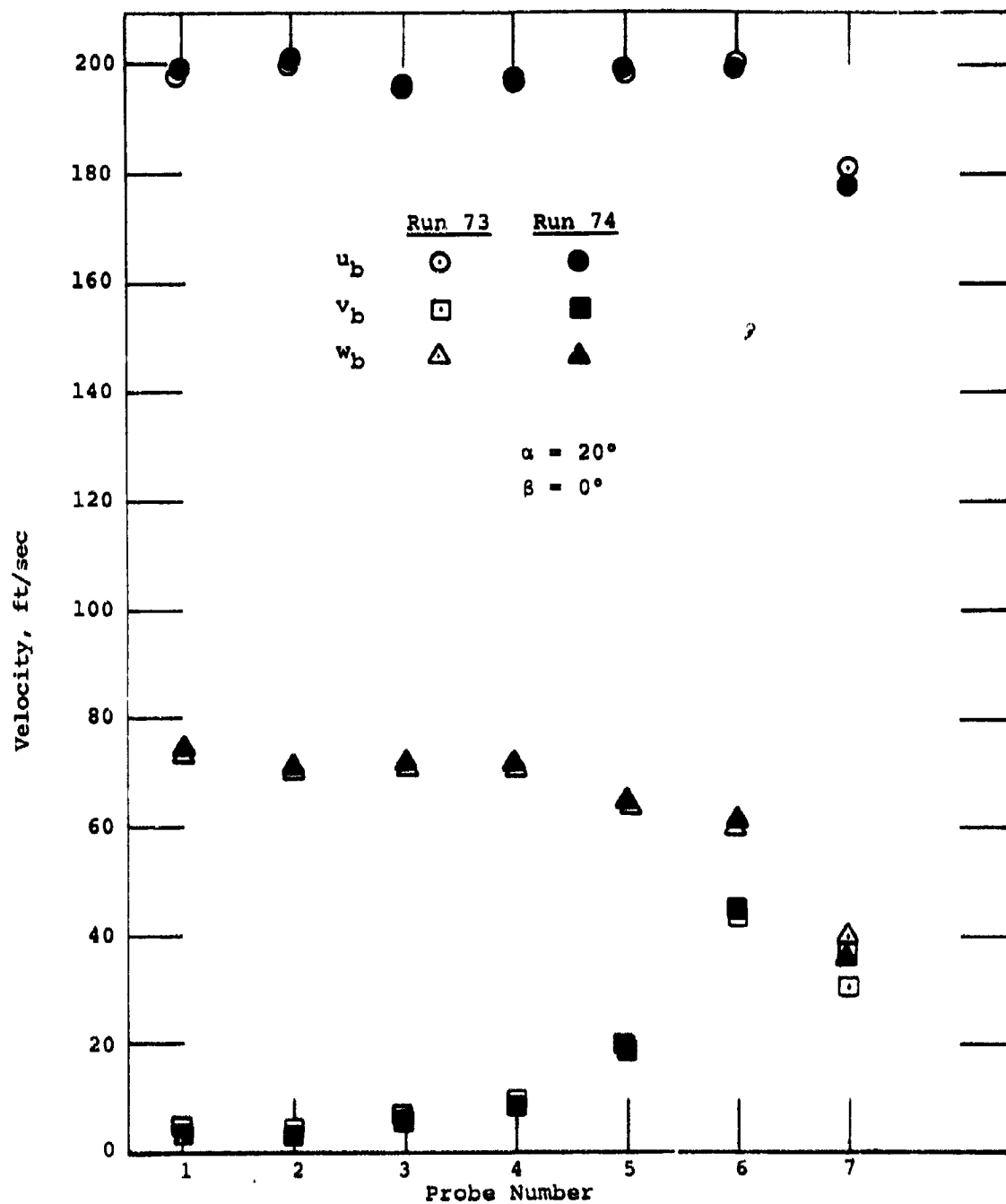Out from Innermost Station.
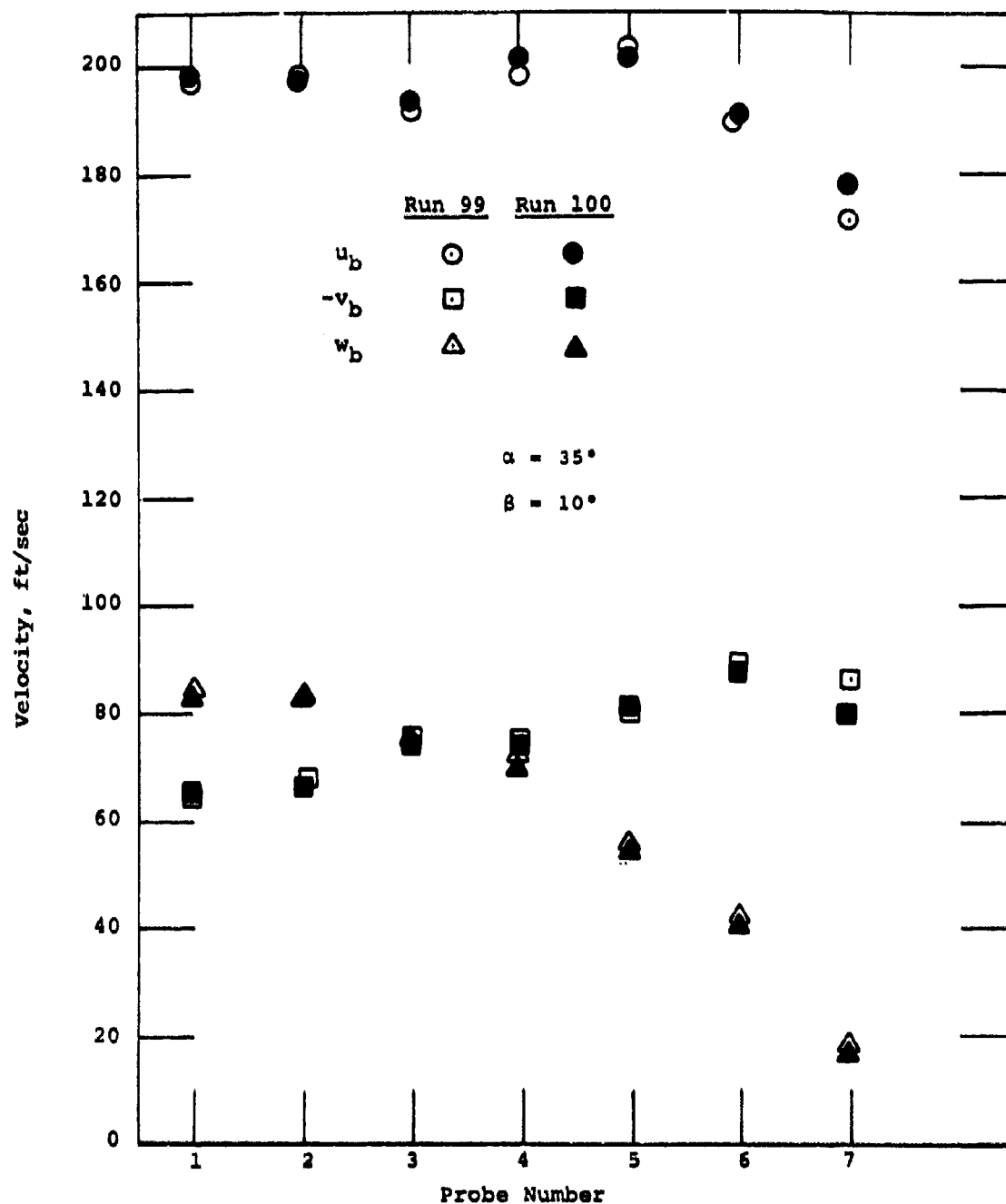
Figure A.14. Comparison of Repeat Probe Velocity Data for Wing-Body
at BS 98, $\theta_g = 85.5°$, Rake Radial Position 33 cm (13 in.)
from Innermost Position.

CROSSFLOW PLANE VELOCITY DISTRIBUTION
OVER V/STOL FIGHTER WING-BODY

PLOT 1
RUNS 82,88
STRAKES ON
ALPHA 20
BETA 0
MACH NO. .17
R_e 7.21x10⁶
TOO #1/24 + 1 1688
X STATION 51.8

Figure A.15

88

CROSSFLOW PLANE VELOCITY DISTRIBUTION
OVER V/STOL FIGHTER WING-BODY

PLOT 2

RUNS 93.00
STRAKES ON
ALPHA 20
BETA 10
MACH NO. .17
Re 7.0x10⁶
200 FT/SEC = 1 INCH
X STATION 51.0

Figure A.16

Figure A.17

Figure A.18

Figure A.19

Figure A.20

CROSSFLOW PLANE VELOCITY DISTRIBUTION
  OVER V/STOL FIGHTER WING-BODY

PLOT 7
RUNS 73,74,75
δ INTAKES OFF
ALPHA 20
BETA 0
MACH NO. .17
R_N 7.2x10^6
200 FRAMES x 1 base
X STATION 55.1

Figure A.21

94

CROSSFLOW PLANE VELOCITY DISTRIBUTION
OVER V/STOL FIGHTER WING-BODY

PLOT 8
RUN# 72.76
STRAKES OFF
ALPHA 20
BETA 10
MACH NO. .17
R$_N$ 7.2x10⁶
200 FT/SEC = 1 BOX
X STATION 68.1
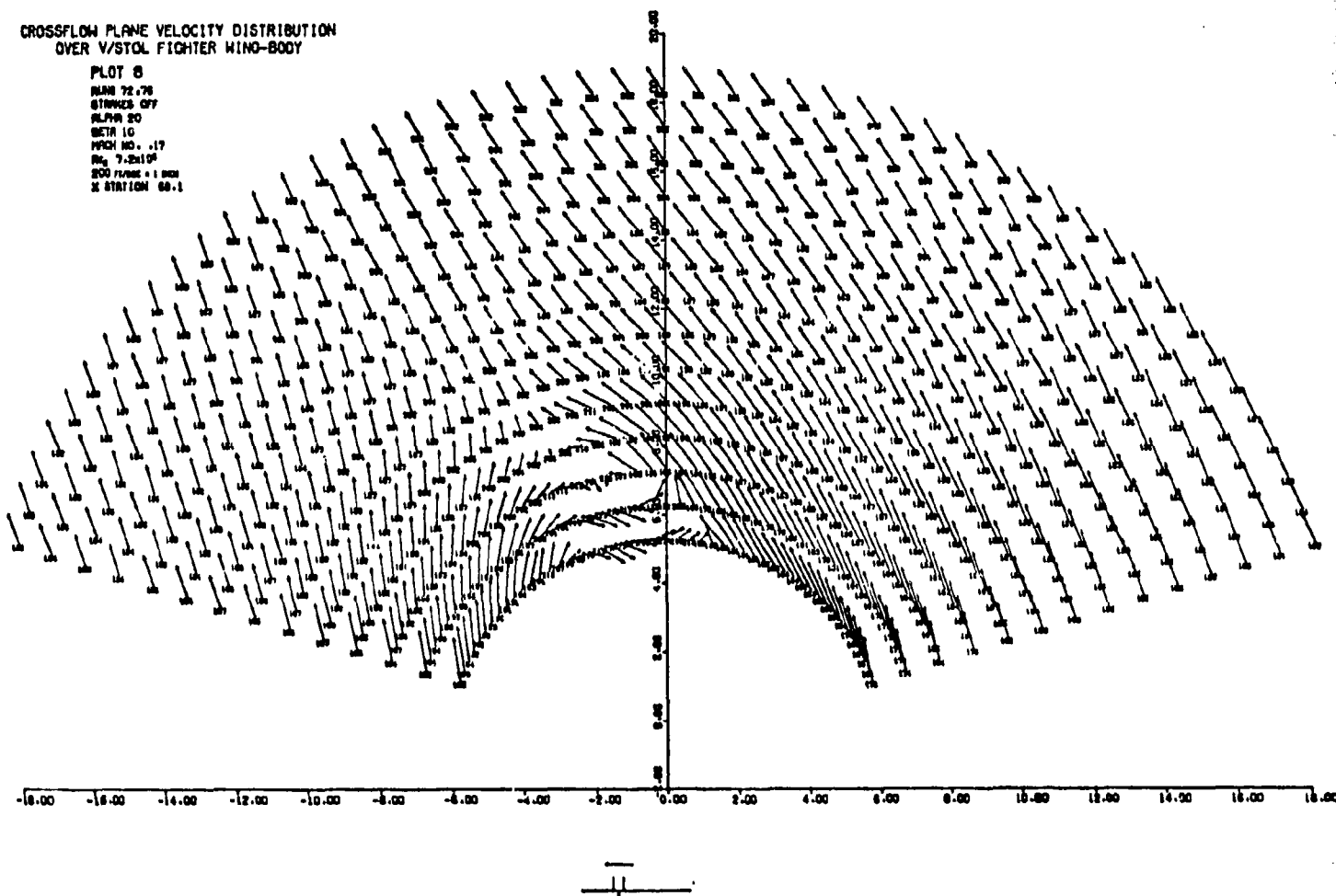
Figure A.22

CROSSFLOW PLANE VELOCITY DISTRIBUTION
OVER V/STOL FIGHTER WING-BODY

PLOT 9
RUNS 91,103
STRAKES ON
ALPHA 36
BETA 0
MACH NO. .17
R_n 7.2x10⁶
200 FT/SEC = 1 INCH
X STATION 87.2
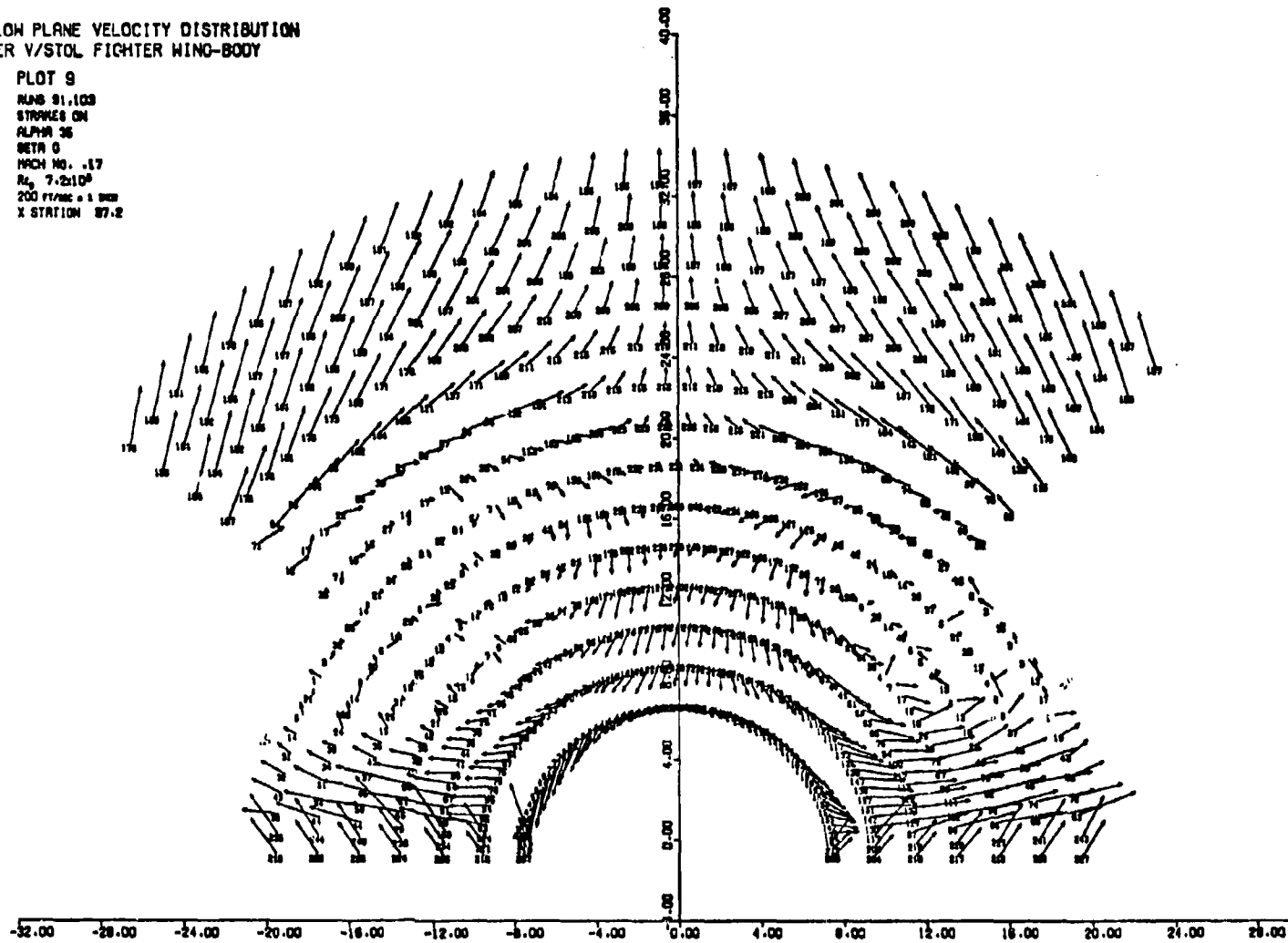
Figure A.23

CROSSFLOW PLANE VELOCITY DISTRIBUTION
OVER V/STOL FIGHTER WING-BODY

PLOT 10
RUNS 92,83,104
STRAKES ON
ALPHA 36
BETA 10
MACH NO. .17
Re_o 7.2x10⁶
200 ft/sec = 1 grid
X STATION 27.2

Figure A.24

CROSSFLOW PLANE VELOCITY DISTRIBUTION
     OVER V/STOL FIGHTER WING-BODY

          PLOT 11
          RUNS 96,106
          STRAKES ON
          ALPHA 20
          BETA 0
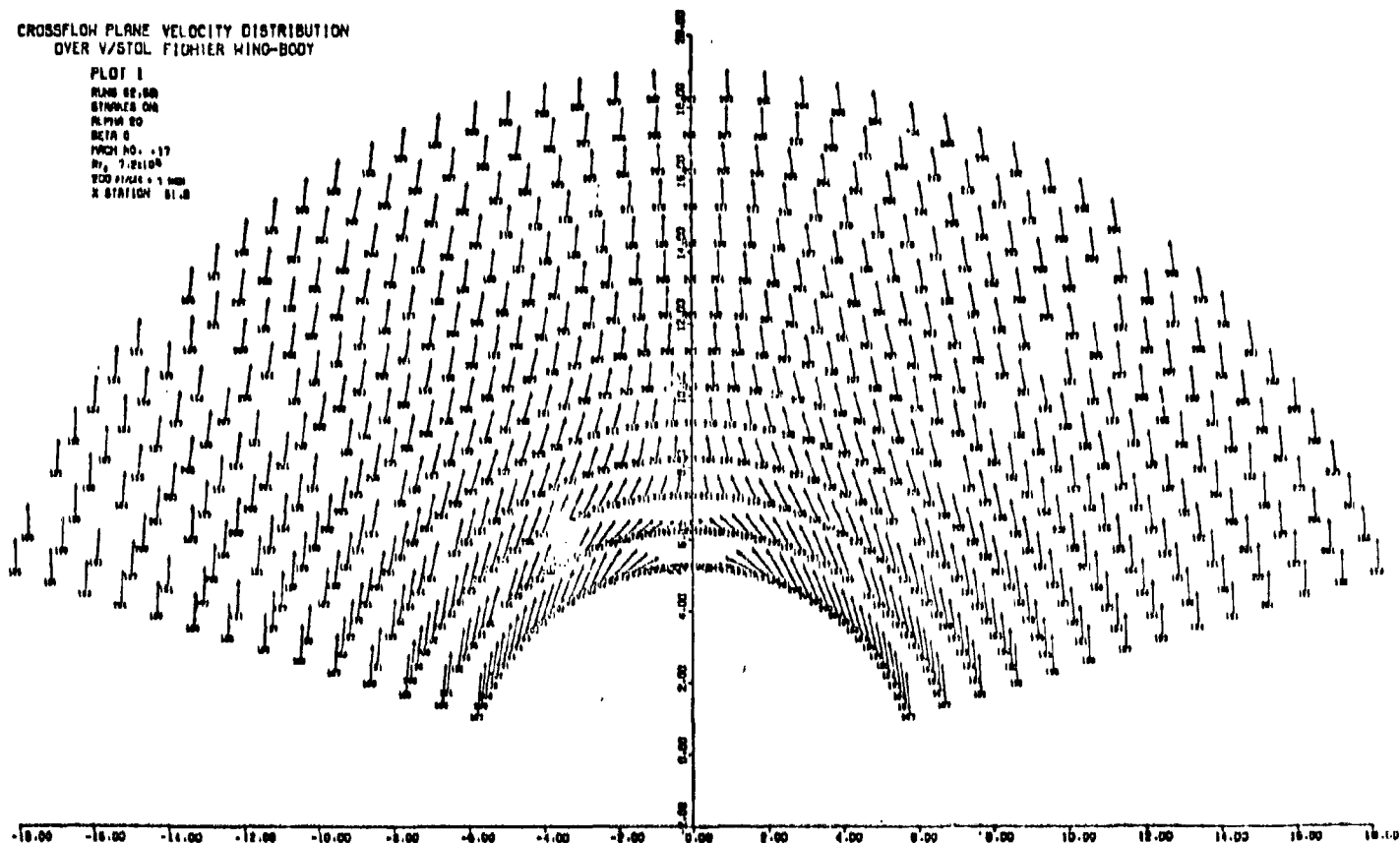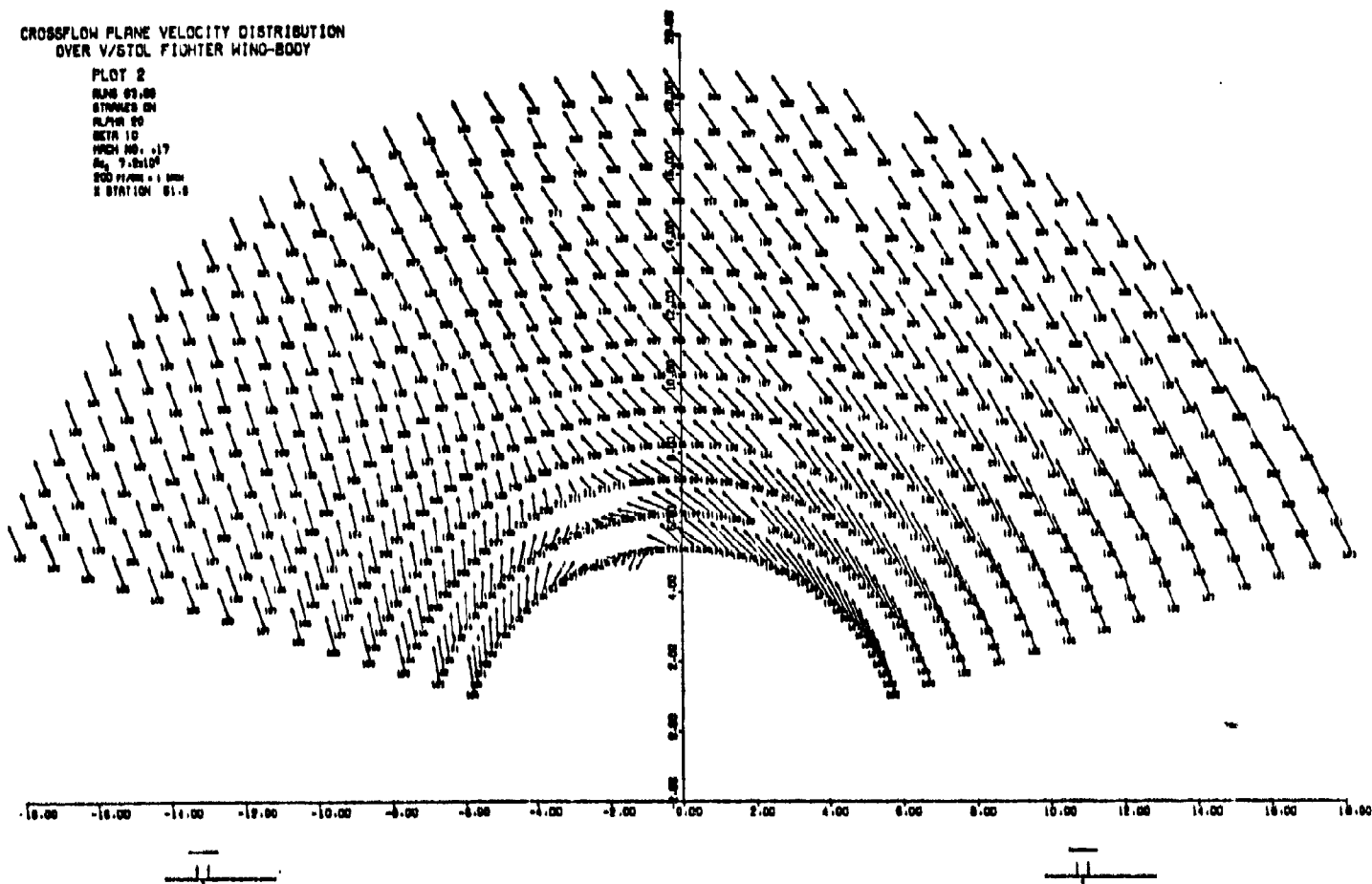   MACH NO. .17
          Re .7.2x10⁶
          200 FT/SEC = 1 INCH
          X STATION 97.2
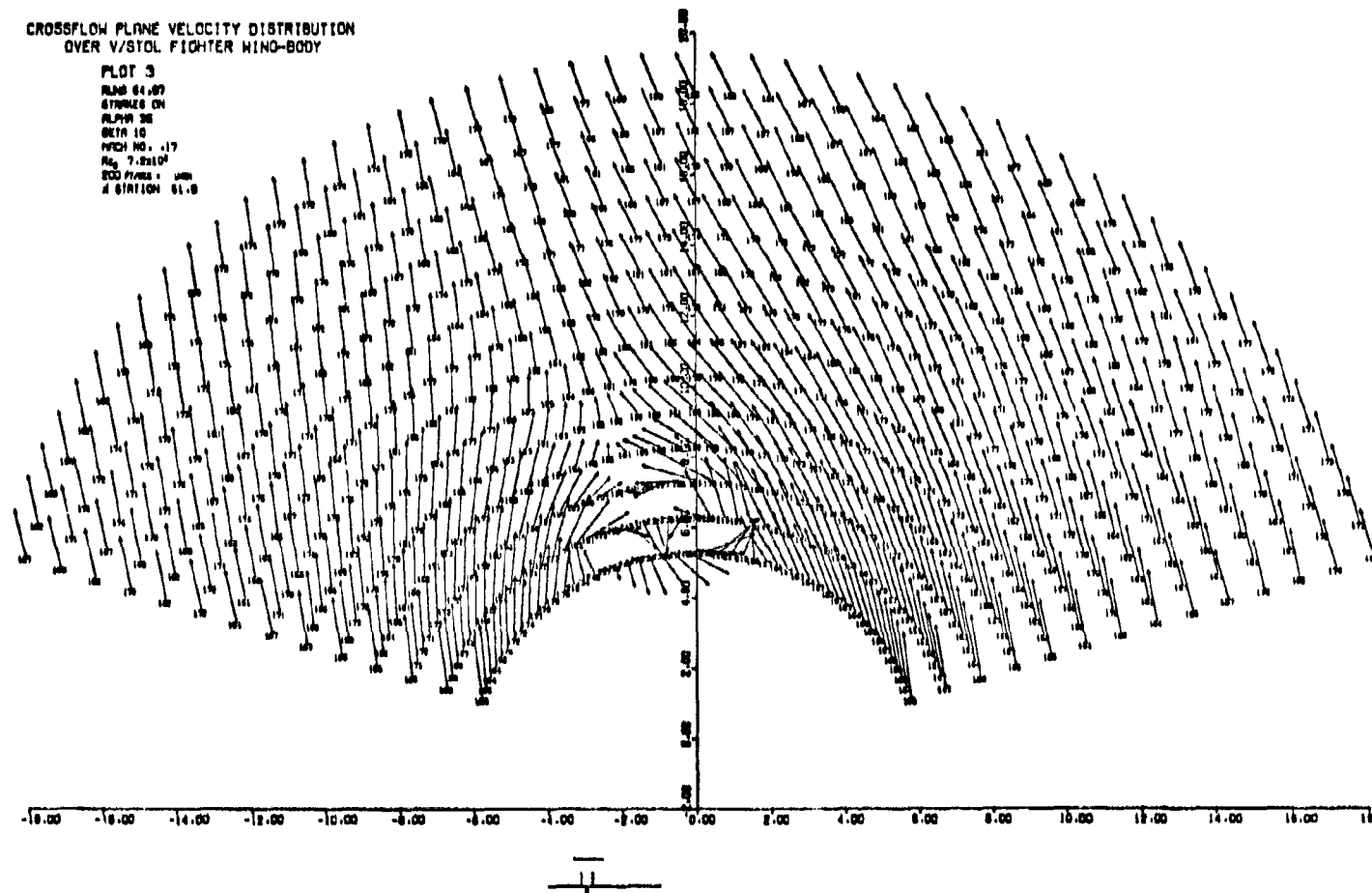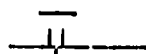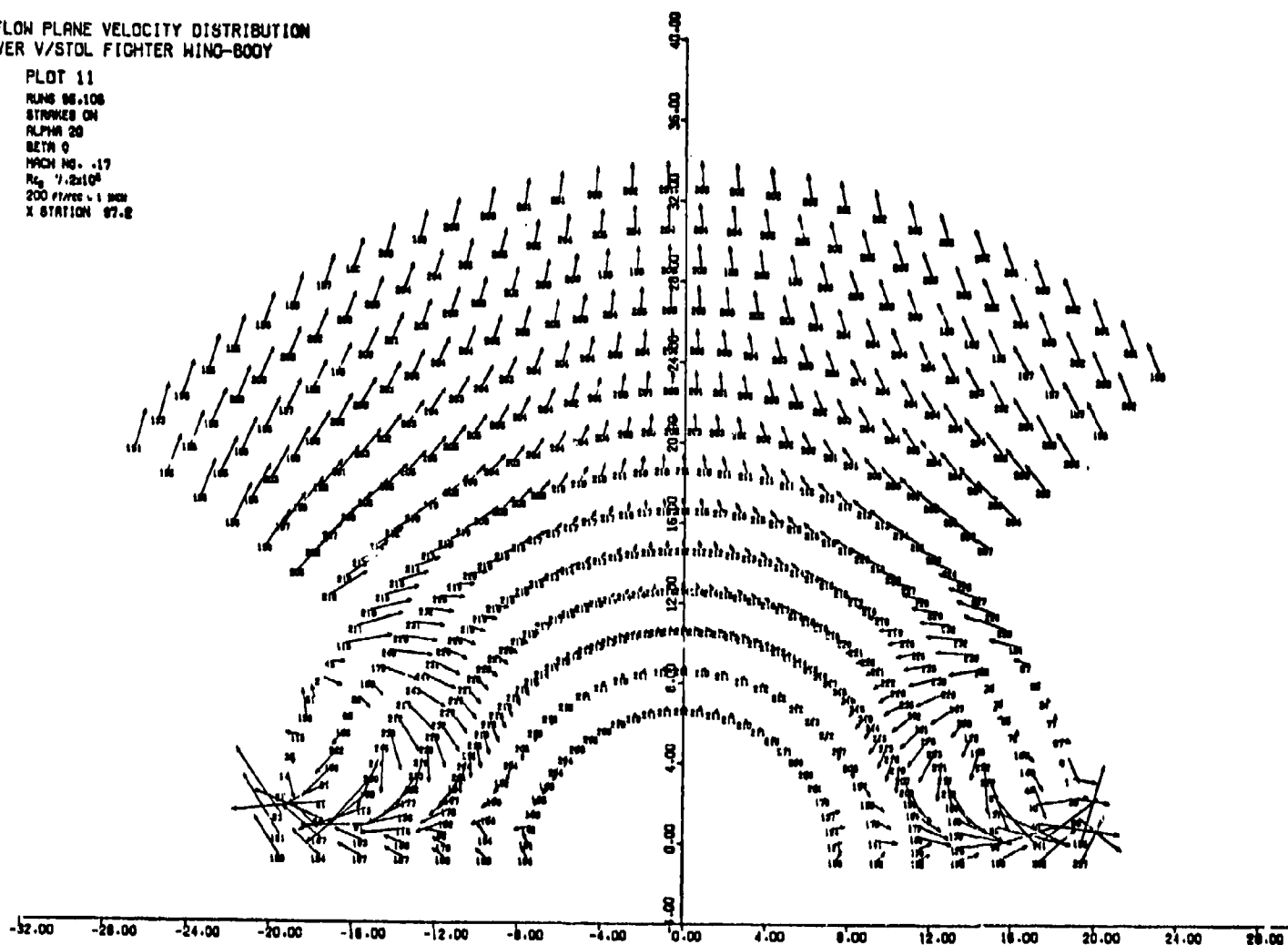
Figure A.25

CROSSFLOW PLANE VELOCITY DISTRIBUTION
   OVER V/STOL FIGHTER WING-BODY

      PLOT 12
      RUNS 94,105
      STRAKES ON
      ALPHA 20
      BETA 10
      MACH NO. .17
      R_g 7.2x10⁶
      200 FT/SEC = 1 INCH
      X STATION 87.2
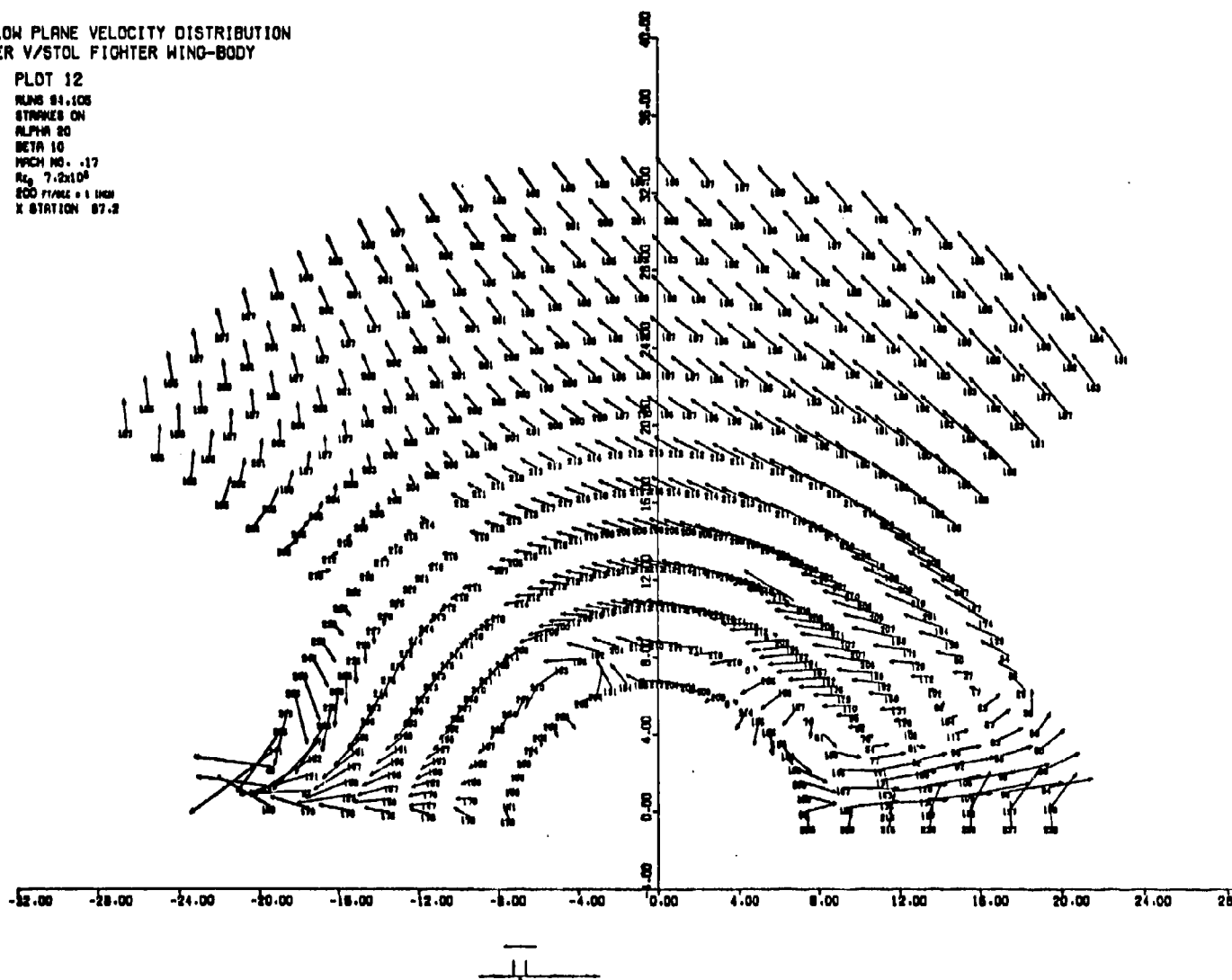
Figure A.26

CROSSFLOW PLANE VELOCITY DISTRIBUTION
OVER V/STOL FIGHTER WING-BODY

PLOT 13
RUNS 112,113,116
STRAKES OFF
ALPHA 35
BETA 0
MACH NO. .17
R_{L_0} 7.2x10^{5}
200 FT/SEC = 1 INCH
X STATION 97.2
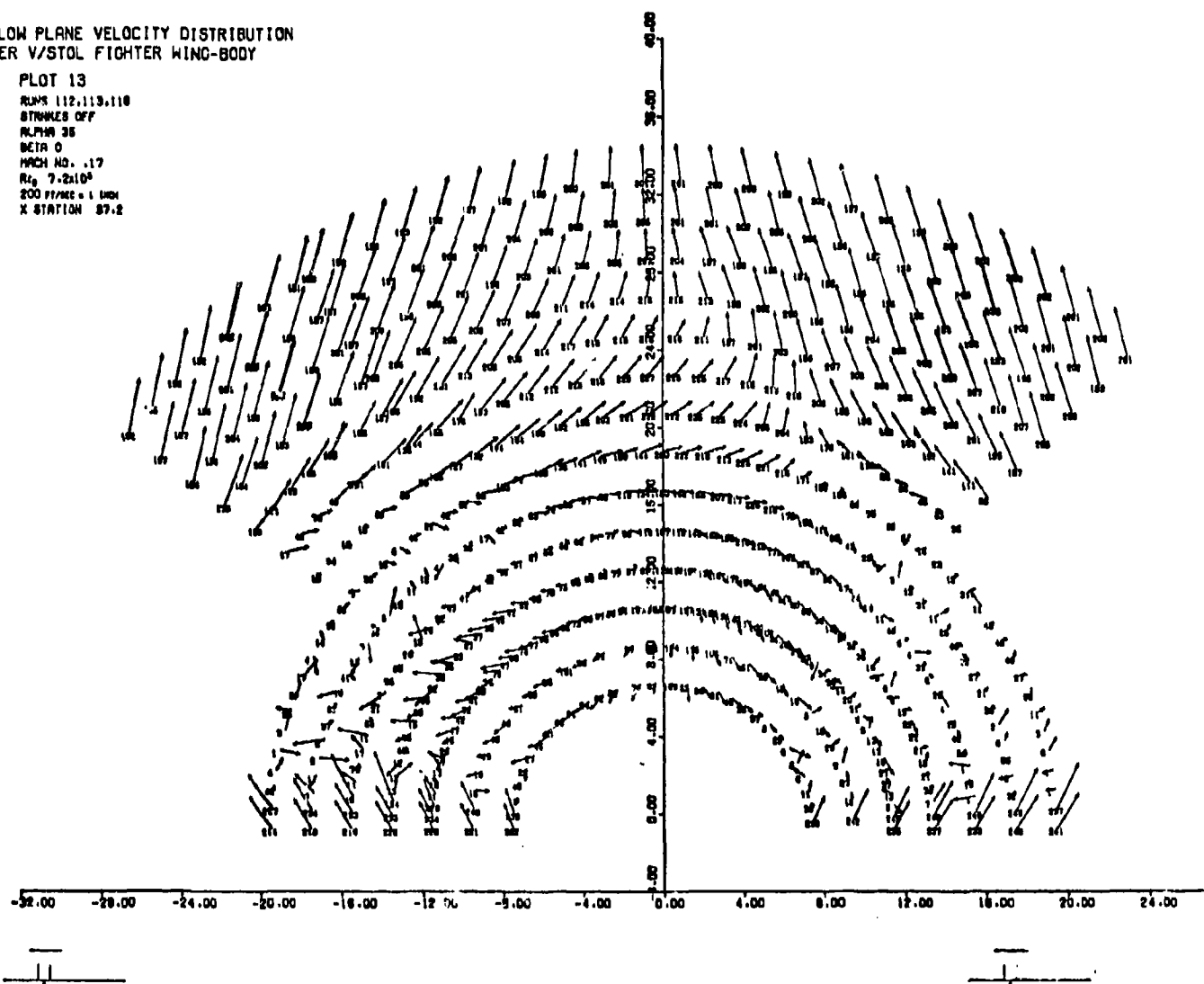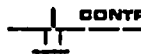
Figure A.27

CROSSFLOW PLANE VELOCITY DISTRIBUTION
    OVER V/STOL FIGHTER WING-BODY

        PLOT 14
        RUNS 114,118,120
        STRAKES OFF
        ALPHA 36
        BETA 10
        MACH NO. .17
        R_θ 7.2x10^6
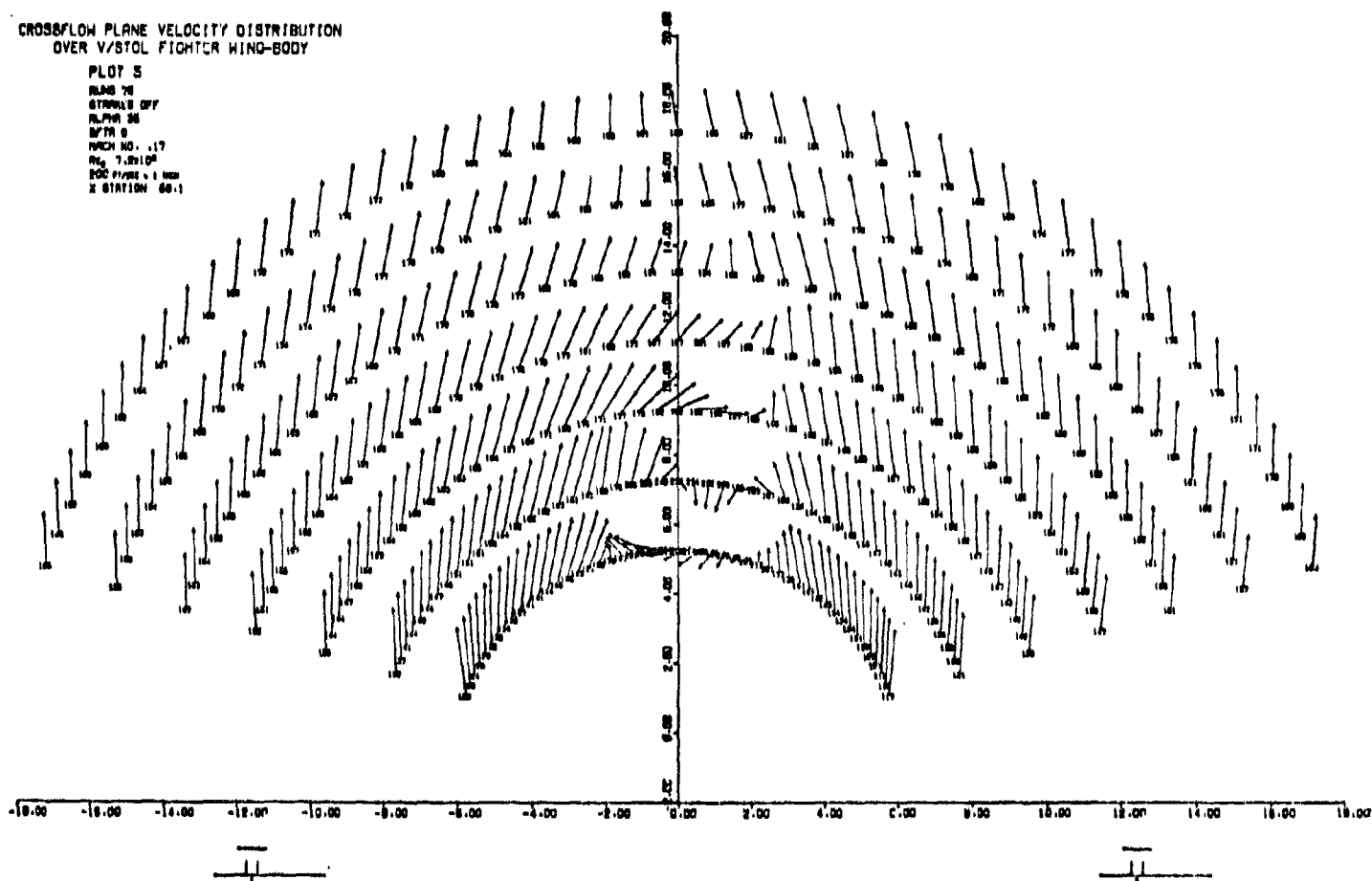   200 FT/SEC = 1 INCH
        X STATION 97.2

Figure A.28

101
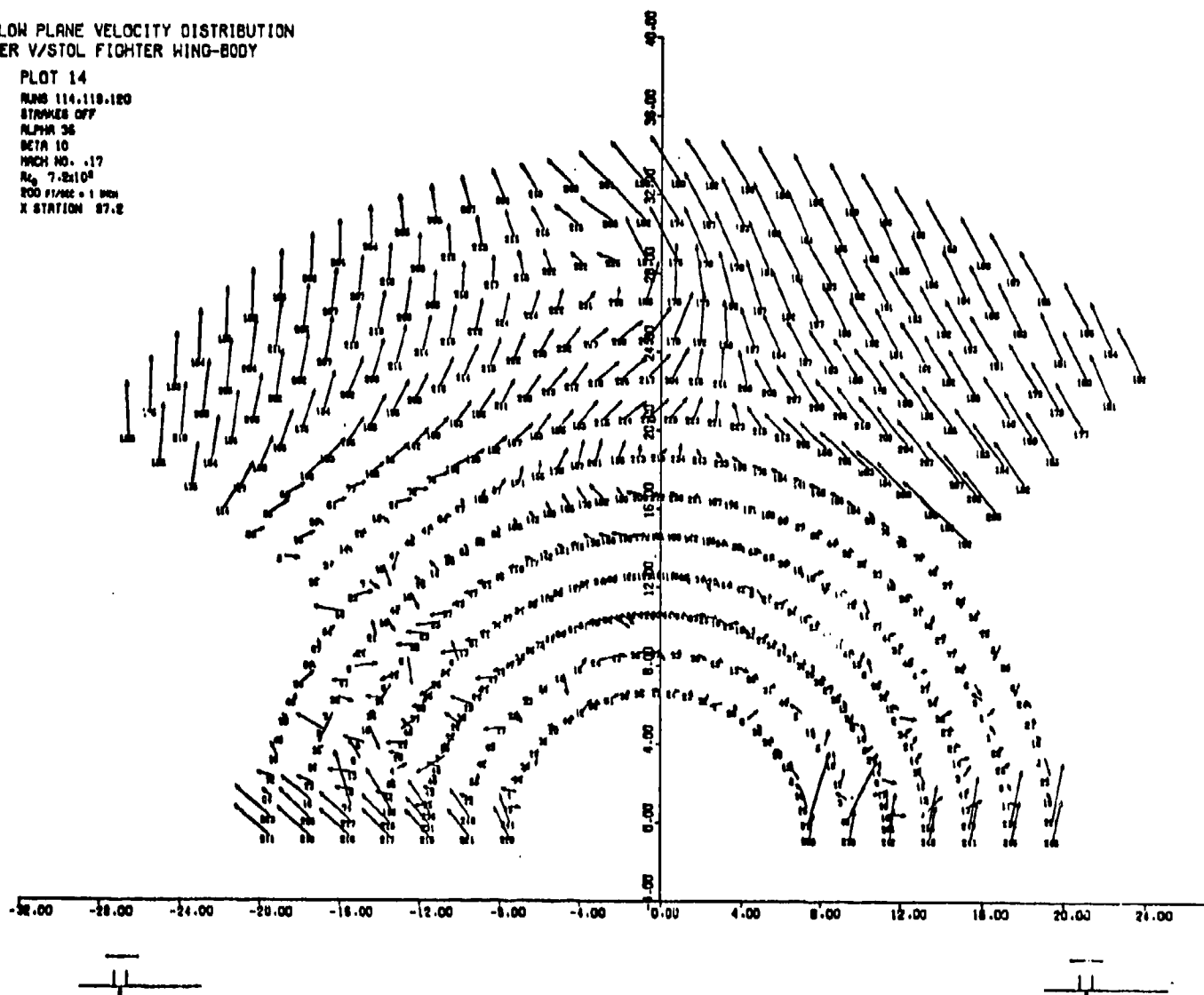
CROSSFLOW PLANE VELOCITY DISTRIBUTION
OVER V/STOL FIGHTER WING-BODY

PLOT 15
RUNS 117,122
STRAKES OFF
ALPHA 20
BETA -0
MACH NO. .17
R_e 7.2x10^6
200 FT/SEC = 1 INCH
X STATION 37.2

Figure A.29

102
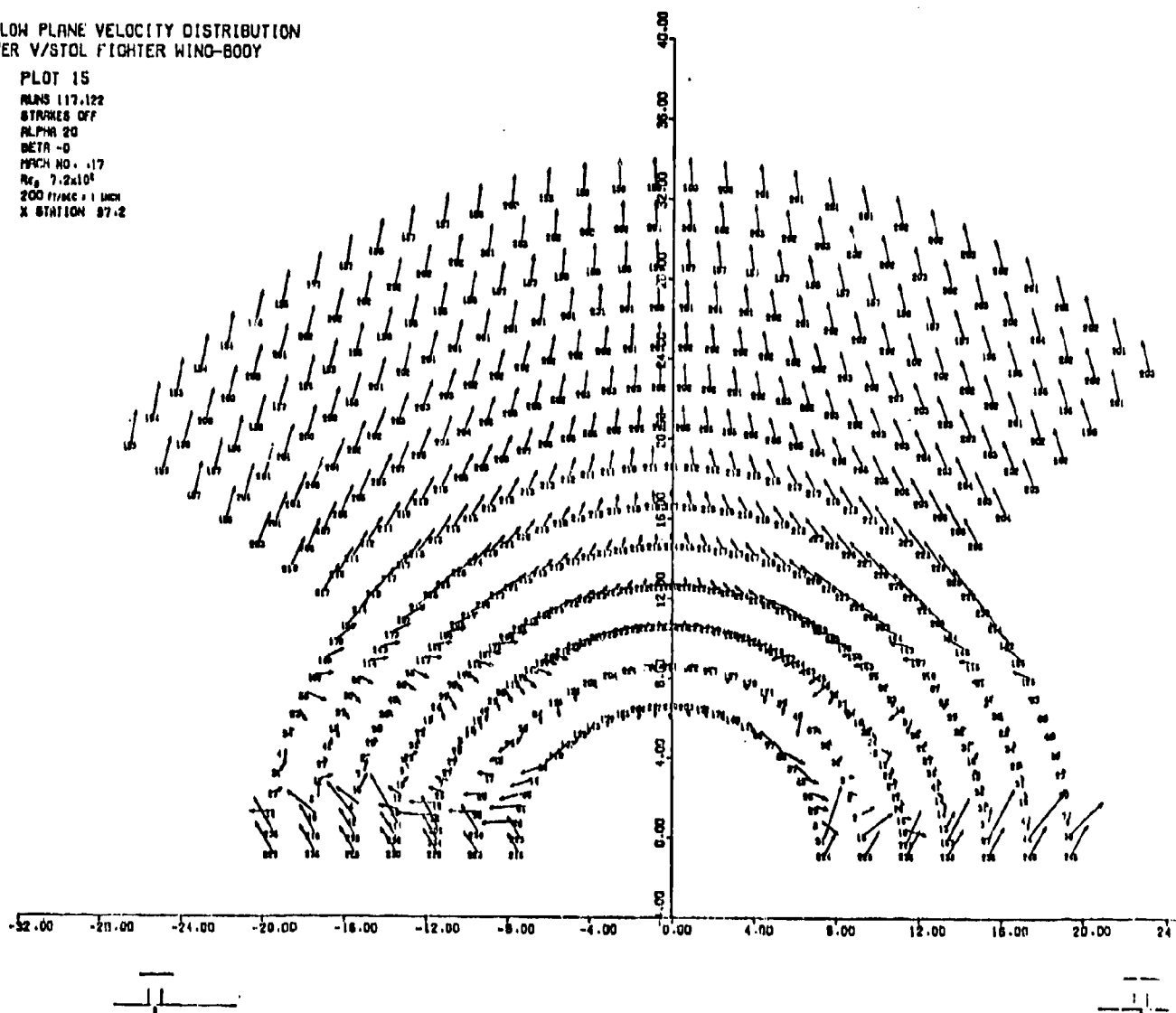
CROSSFLOW PLANE VELOCITY DISTRIBUTION
OVER V/STOL FIGHTER WING-BODY

PLOT 16

RUNS 115,116,121
STRAKES OFF
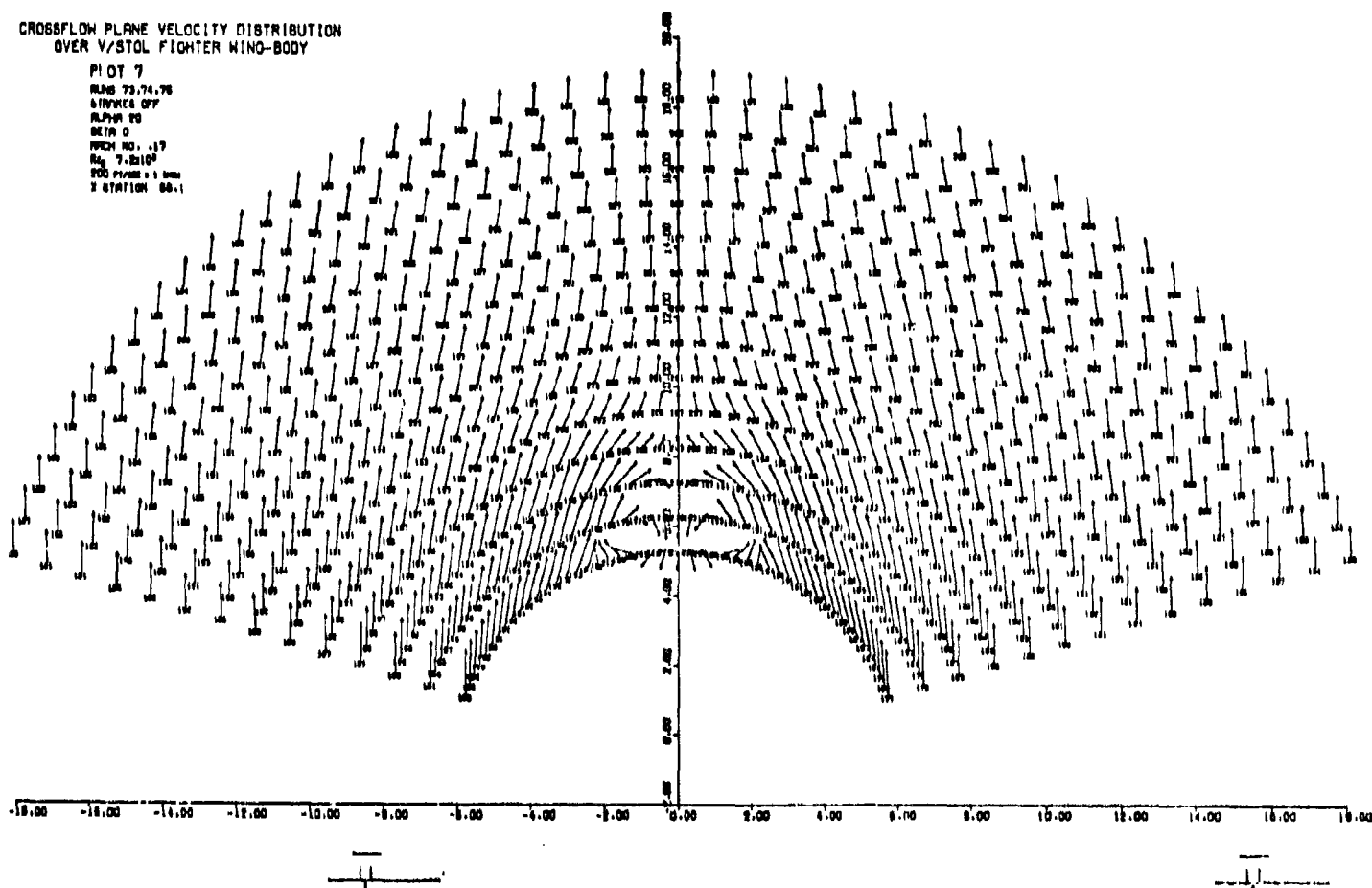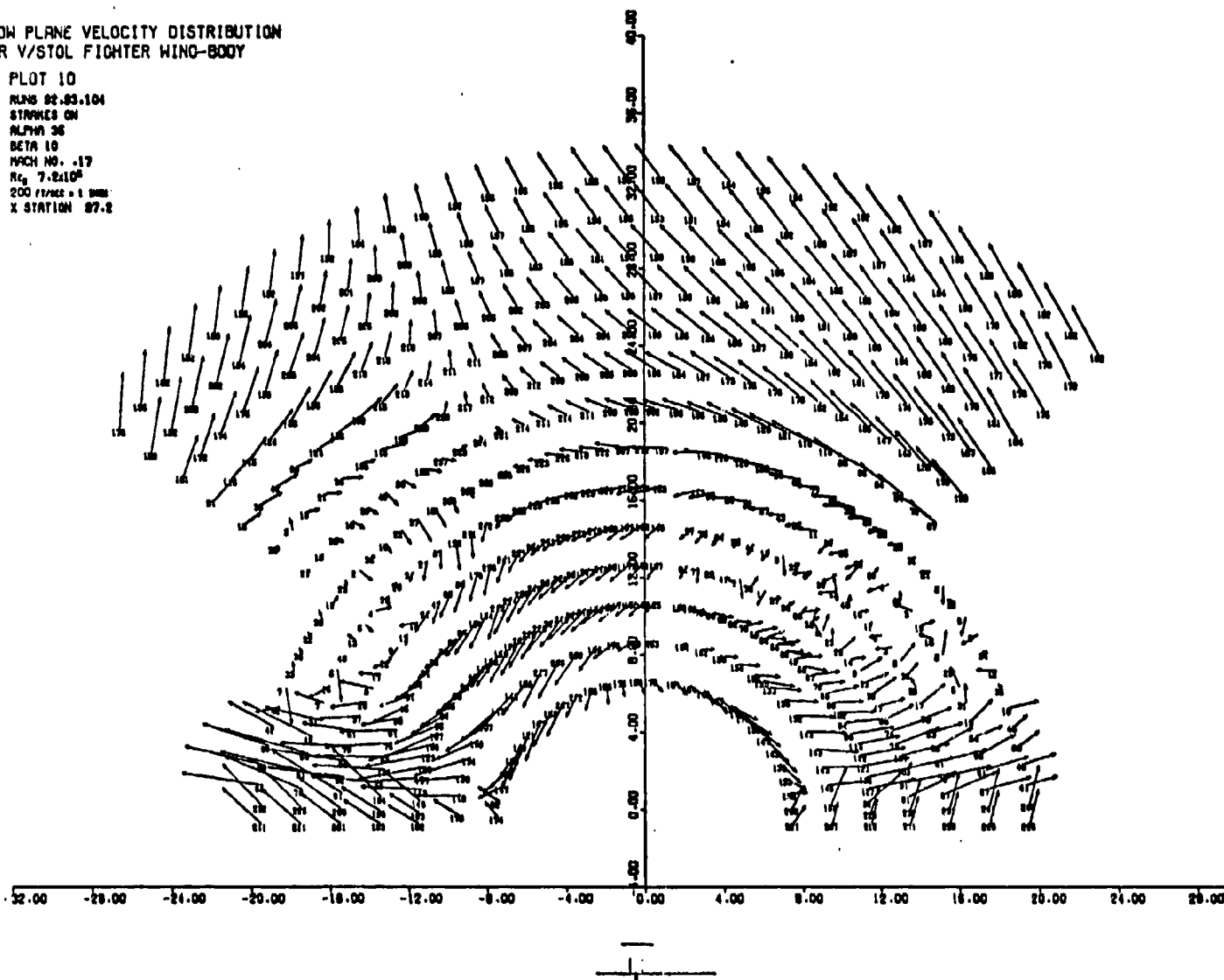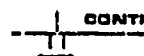ALPHA 20
BETA 10
MACH NO. .17
R_e 7.2x10^6
200 FT/SEC = 1 INCH
X STATION 87.2
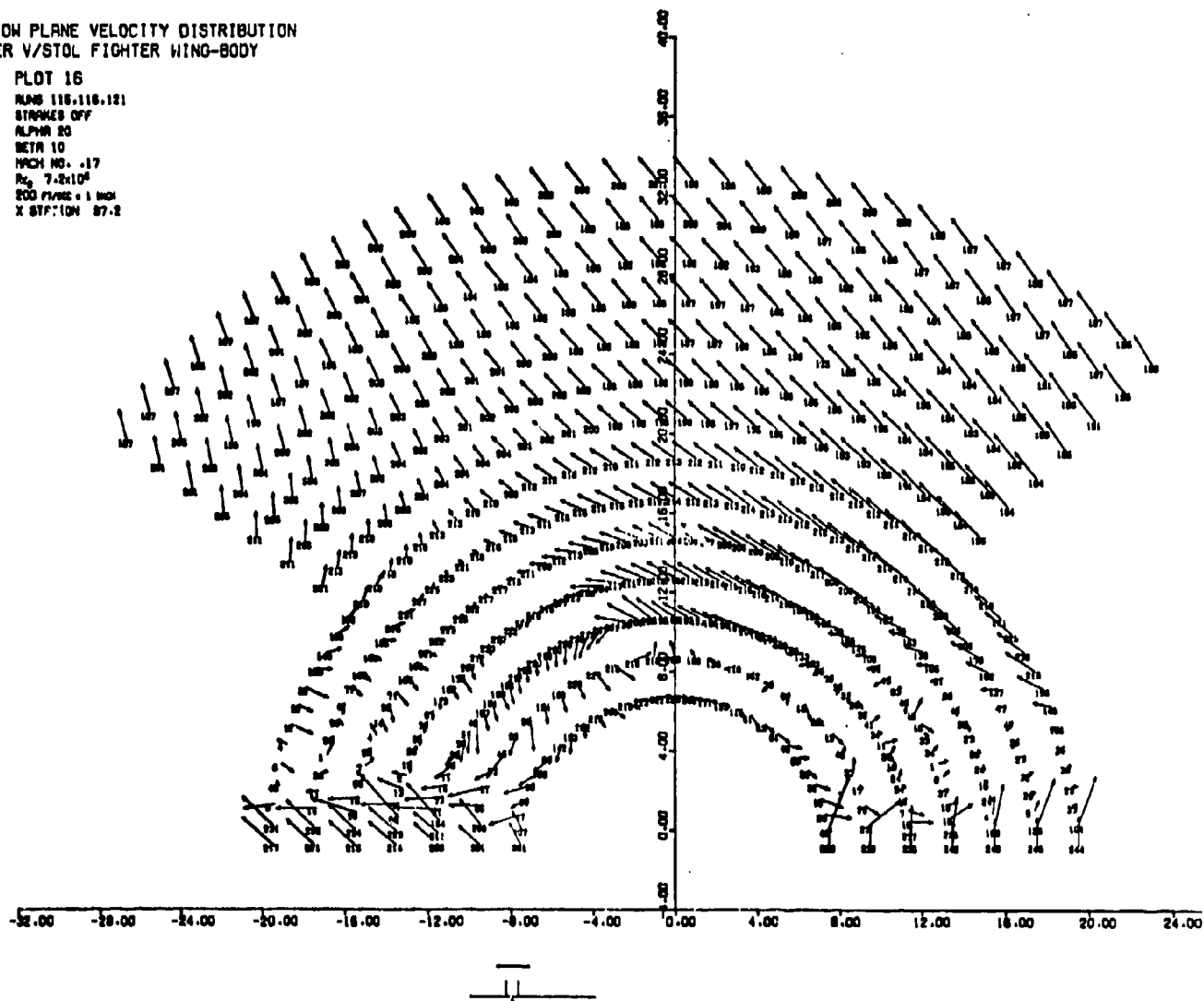
Figure A.30

APPENDIX B

RESULTS OF NEAR WATER TUNNEL
TESTS

TABLE B.1

VORTEX POSITION DATA

Configuration	α	β	x/L	left vortex y_v/d_{eq}	left vortex z_v/d_{eq}	right vortex y_v/d_{eq}	right vortex z_v/d_{eq}
F-5	30°	0°	.1	-.083	.14	.094	.14
			.2	-.14	.22	.19	.22
			.3	-.20	.32	.24	.32
			.4	-.21	.40	.27	.44
			.5	-.23	.52	.27	.55
			.6	-.21	.62	.25	.69
			.7	-.19	.75	.24	.83
			.8	-.21	.87	.26	.97
			.9	-.21	.94	.25	1.06
			1.0	-.23	1.01	.23	1.13
F-5	40°	0°	.1	-.089	.11	.079	.11
			.2	-.15	.23	.14	.23
			.3	-.20	.35	.20	.37
			.4	-.24	.46	.20	.57
			.5	-.23	.58	.24	.63
			.6	-.22	.68	.20	.75
			.7	-.20	.80	.18	.88
			.8	-.20	.89	.16	1.0
			.9	-.28	1.00	.18	1.11
			1.0	-.34	1.06	.12	1.27
F-5	30°	10°	.1	-.15	.09	.050	.09
			.2	-.25	.19	.070	.19
			.3	-.32	.30	.080	.30
			.4	-.38	.42	.080	.39
			.5	-.44	.52	.070	.48
			.6	-.46	.63	.060	.60
			.7	-.50	.74	.050	.69
			.8	-.54	.84	.020	.81
			.9	-.57	.86	0	.95
			1.0	-.58	.88	0	.98

F-5	34°	10°	.1	-.10	.13	.062	.13
			.2	-.21	.23	.11	.23
			.3	-.29	.33	.15	.33
			.4	-.31	.43	.11	.46
			.5	-.35	.51	.11	.56
			.6	-.37	.61	.11	.66
			.7	-.45	.70	.073	.81
			.8	-.47	.81	.073	.97
			.9	-.52	.90	.052	1.07
			1.0	-.55	.88	0	1.15
F-5	40°	10°	.1	-.12	.14	.030	.14
			.2	-.19	.24	.080	.24
			.3	-.28	.35	.12	.40
			.4	-.34	.44	.12	.54
			.5	-.42	.54	.12	.68
			.6	-.46	.62	.050	.81
			.7	-.54	.73	.080	.93
			.8	-.62	.88	.060	1.03
			.9	-.70	.98	-.050	-
			1.0	-.77	1.03	-.18	-
VSTOL	20°	0°	.1	no	.20	no	.20
			.2	data	.40	data	.40
			.3	↓	.51	↓	.51
			.4		.57		.57
			.5		.58		.58
			.6		.58		.58
			.7		.58		.58
			.8		.58		.58
			.9		.62		.62
			1.0		.62		.62
VSTOL	25°	0°	.1	no	.23	no	.23
			.2	data	.42	data	.42
			.3	↓	.52	↓	.52
			.4		.57		.57
			.5		.60		.60

106

			.6	↑	.57	↓	.57
			.7		.59		.59
			.8		.65		.65
			.9	↓	.70	↓	.70
			1.0		.74		.74
VSTOL	30°	0°	.1	no	.18	no	.18
			.2	data	.38	data	.38
			.3		.54		.54
			.4		.61		.61
			.5		.63		.63
			.6		.63		.63
			.7		.64		.64
			.8		.65		.65
			.9	↓	.70	↓	.70
			1.0		.76		.76
VSTOL	35°	0°	.1	–	.20	–	.20
			.2	-.23	.42	.21	.42
			.3	-.23	.56	.21	.56
			.4	-.21	.65	.19	.65
			.5	-.17	.68	.19	.68
			.6	-.14	.70	.16	.70
			.7	-.16	.71	.16	.71
			.8	-.17	.75	.12	.75
			.9	-.19	.80	.14	.80
			1.0	–	.86	–	.86
VSTOL*	20°	10°	.1	–	–	–	–
			.2	-.37	.24	.056	.44
			.3	-.43	.34	-.037	.56
			.4	-.48	.40	-.10	.60
			.5	-.47	.45	-.11	.60
			.6	-.49	.47	-.093	.61
			.7	-.49	.47	-.084/+.10	.61/.61
			.8	-.45	.45	-.17/+.092	.65/.65
			.9	-.45	.5	-.22/+.092	.65/.65
			1.0	-.45	.51	-/+.092	.65/.65

TABLE B.1 Continued

VSTOL*	30°	10°	.1	-.19	-	.038	-
			.2	-.29	.43	.057	.43
			.3	-.32	.54	.038	.54
			.4	-.34	.63	-.019/.15	.63/.63
			.5	-.34	.65	-.057/.17	.65/.65
			.6	-.34	.66	-.095/.15	.66/.66
			.7	-.34	.62	-.095/.13	.69/.69
			.8	-.34	.65	-/.13	.76/.76
			.9	-.34	.63	-/.038	.82/.82
			1.0	-.34	.61	-/0	.86/.86
VSTOL	35°	10°	.1	-	-	-	-
			.2	-.23	.36	-	-
			.3	-.31	.48	.078	-
			.4	-.35	.63	.078	.63
			.5	-.35	.63	.088	.68
			.6	-.30	.63	.088	.70
			.7	-.28	.64	.078	.76
			.8	-.19	.65	.097	.85
			.9	-.16	.62	.097	.97
			1.0	-	.63	.097	1.12
ELLIPTIC OGIVE MAJOR AXIS HORIZONTAL	30°	0°	.1	-	.12	-	.12
			.2	-.098	.21	.098	.21
			.3	-.16	.26	.16	.30
			.4	-.20	.35	.21	.41
			.5	-.26	.41	.26	.48
			.6	-.29	.47	.29	.59
			.7	-.31	.52	.32	.70
			.8	-.33	.59	.34	.77
			.9	-.31	.65	.37	.83
			1.0	-.29	.70	.40	.87

*Some indication exists that a third vortex is forming under the first
vortex on the right side.

ELLIPTIC OGIVE MAJOR AXIS HORIZONTAL	40°	0°	.1	-.061	.11	.061	.11
			.2	-.11	.22	.11	.27
			.3	-.15	.28	.15	.39
			.4	-.20	.36	.20	.51
			.5	-.24	.42	.26	.64
			.6	-.24	.48	.29	.75
			.7	-.24	.55	.34	.94
			.8	-.23	.59	.40	1.12
			.9	-.18	.64	.45	1.32
			1.0	-.16	.70	.51	1.57
ELLIPTIC OGIVE MAJOR AXIS HORIZONTAL	30°	10°	.1	-	.15	-	.15
			.2	-.20	.24	.039	.24
			.3	-.26	.32	.039	.32
			.4	-.33	.38	.059	.38
			.5	-.41	.46	.098	.46
			.6	-.47	.52	.098	.48
			.7	-.57	.52	.118	.60
			.8	-.65	.74	.118	.56
			.9	-.71	.84	.079	.60
			1.0	-.79	.89	0	.65
ELLIPTIC OGIVE MAJOR AXIS HORIZONTAL	40°	10°	.1	-	.12	-	.12
			.2	-.16	.24	.053	.24
			.3	-.22	.31	.083	.31
			.4	-.29	.41	.12	.41
			.5	-.37	.50	.13	.50
			.6	-.43	.56	.13	.56
			.7	-.49	.63	.12	.63
			.8	-.52	.71	.12	.71
			.9	-.59	.79	.13	.79
			1.0	-.61	.87	.13	.87

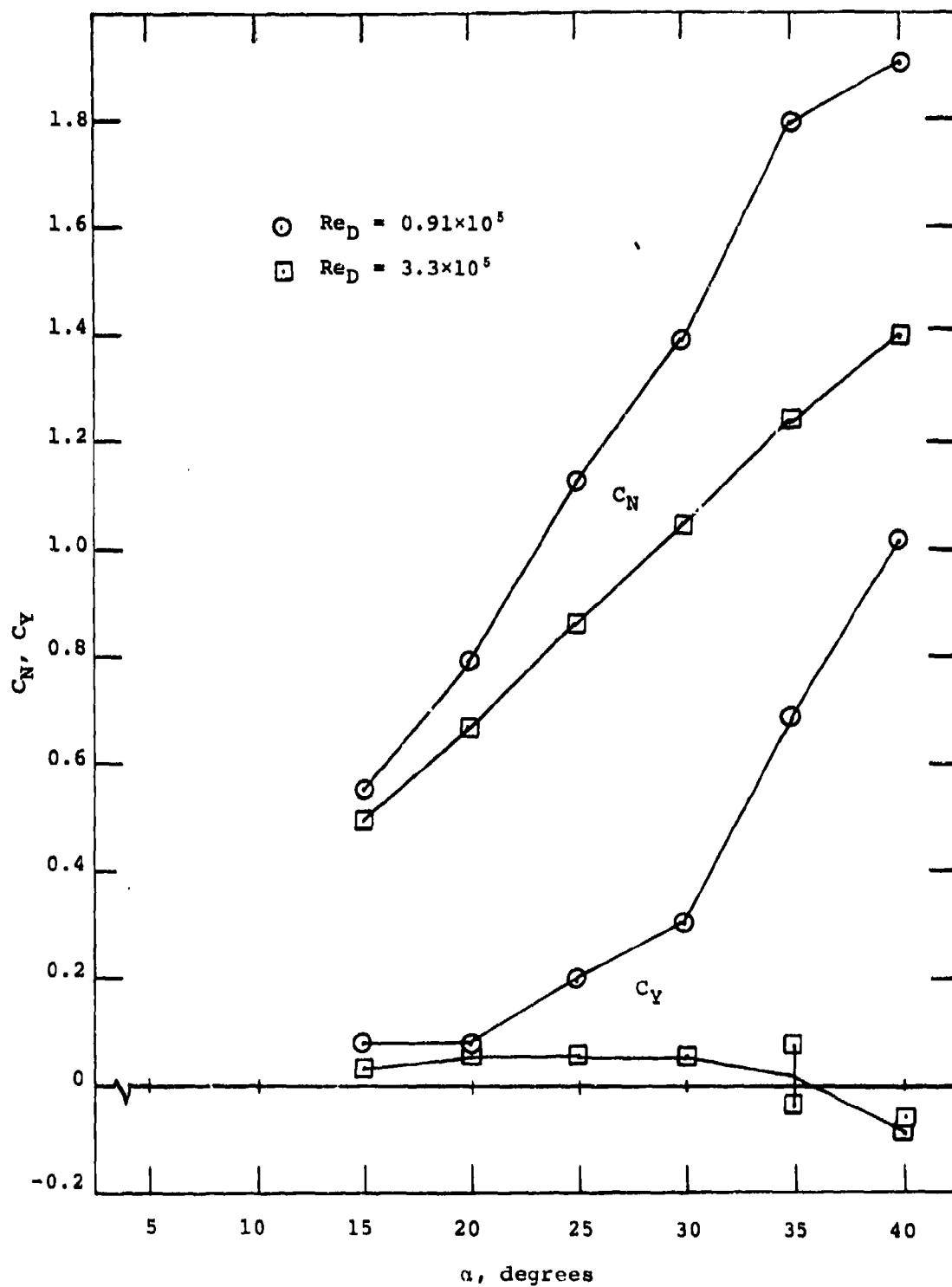|							
ELLIPTIC OGIVE MAJOR AXIS VERTICAL	30°	0°	.1	–	–	–	–
			.2	-.057	.28	.048	.28
			.3	-.076	.43	.076	.38
			.4	-.094	.60	.057	.47
			.5	-.11	.7?	.057	.53
			.6	-.13	.94	.057	.59
			.7	-.15	1.13	.094	.64
			.8	-.15	1.34	.13	.68
			.9	-.16	1.60	.13	.74
			1.0	-.20	–	.13	.77
ELLIPTIC OGIVE MAJOR AXIS VERTICAL	40°	0°	.1	-.060	.21	–	.17
			.2	-.099	.44	.038	.29
			.3	-.11	.74	.038	.38
			.4	-.14	1.03	.038	.50
			.5	-.18	1.35	.049	.59
			.6	-.22	1.71	.058	.66
			.7	-.23	2.02	.049	.76
			.8	–	2.47	.049	.84
			.9	–	2.77	.058	.90
			1.0	–	–	.077	.96
ELLIPTIC OGIVE MAJOR AXIS VERTICAL	40°	10°	.1	no	–	–	–
			.2	data	.25	0	.31
			.3	↓	.35	0	.49
			.4		.46	.04	.74
			.5		.54	.04	.99
			.6		.61	0	1.28
			.7		.63	-.06	1.63
			.8		.71	-.09	2.01
			.9	↓	.79	-.14	2.38
			1.0		.82	-.20	2.75

Figure B.1.   Normal and Side Force Variation with Angle of
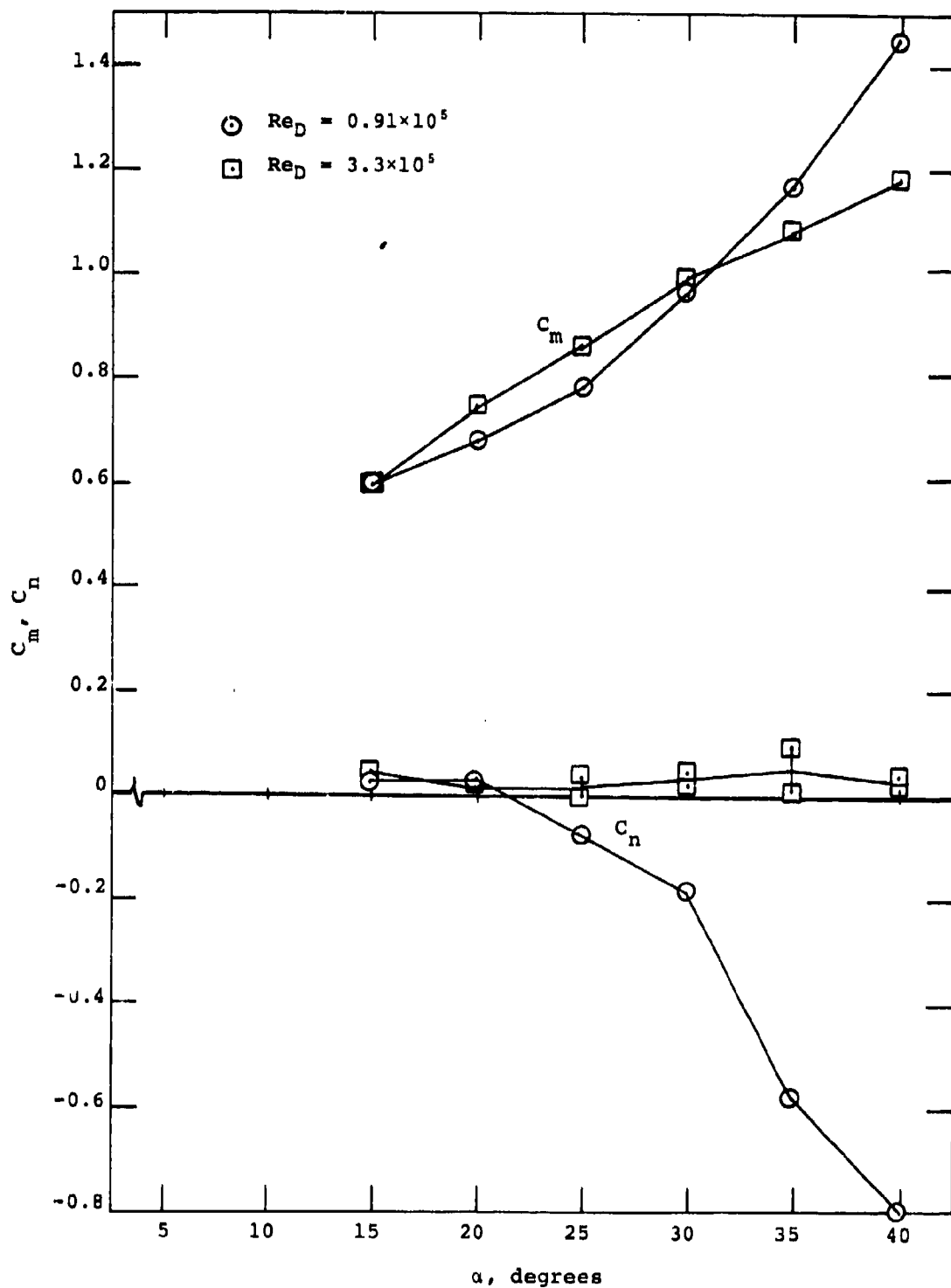Attack for V/STOL Nose. $\beta = 0$.

Figure B.2. Pitching and Yawing Moment Variation with Angle of Attack for V/STOL Nose. $\beta = 0$.
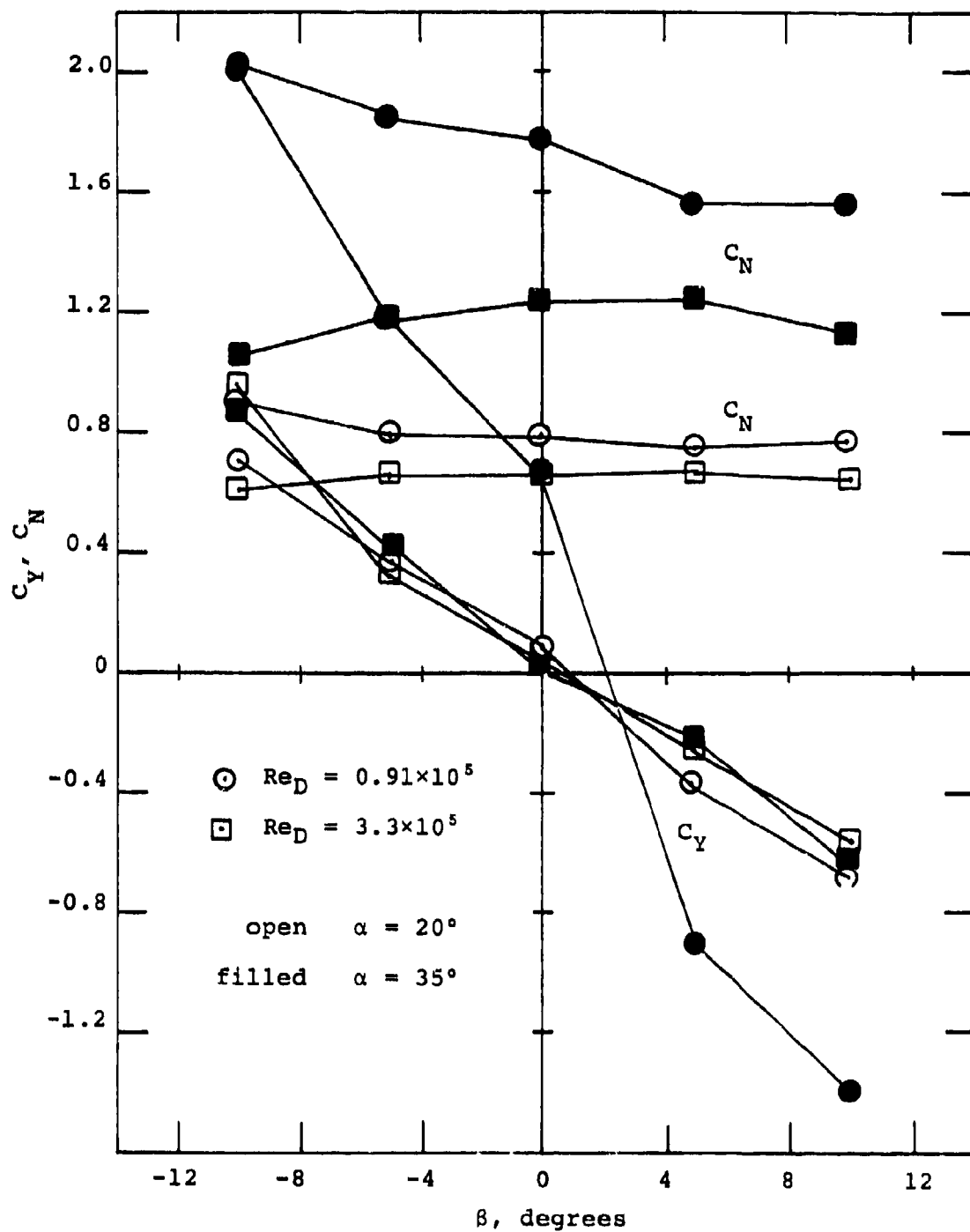
112

Figure B.3. Normal and Side Force Variation with Sideslip
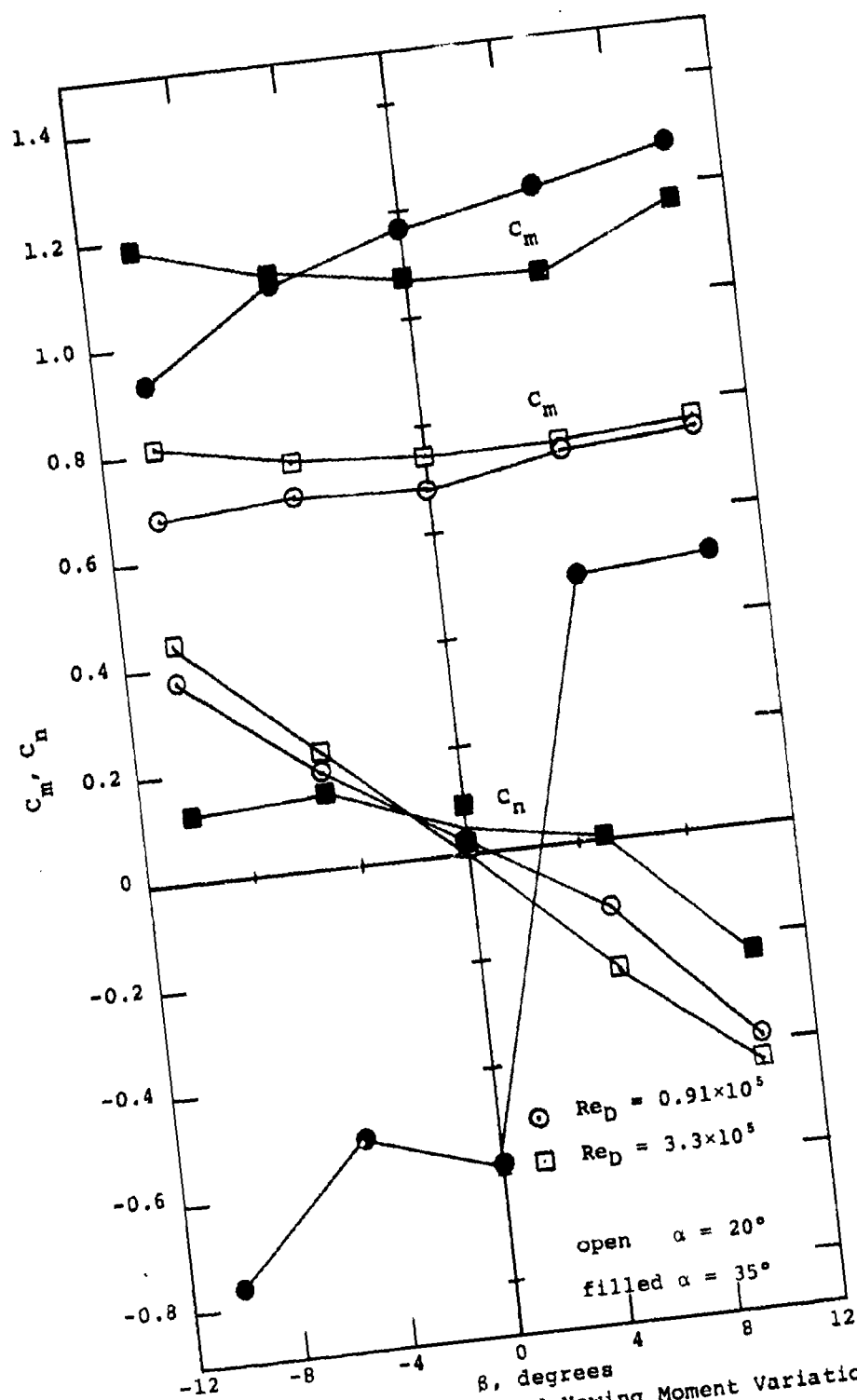for V/STOL Nose.

Figure B.4. Pitching and Yawing Moment Variations with Sideslip for V/STOL Nose.
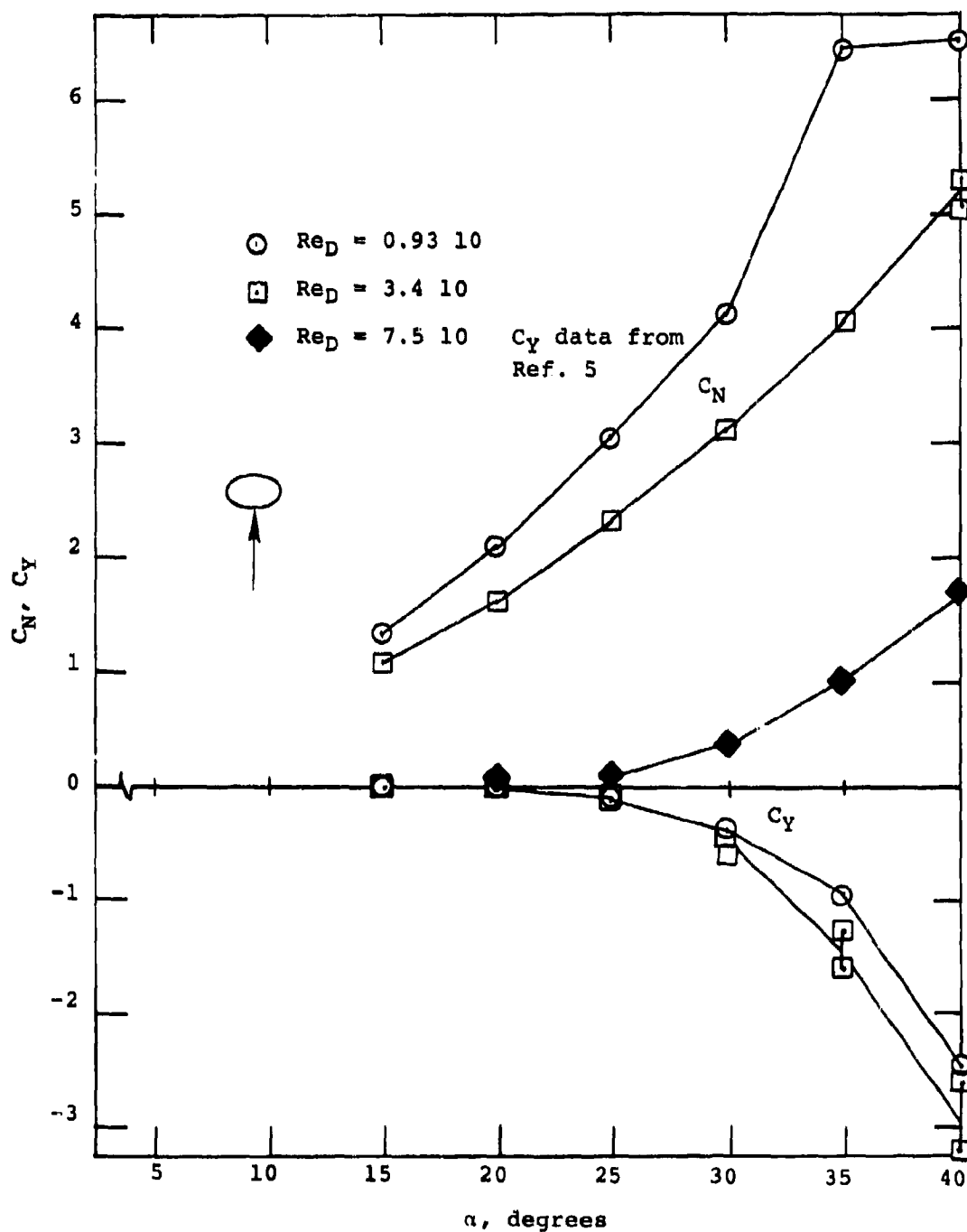
Figure B.5. Normal and Side Force Variations with Angle of
Attack for Elliptical Ogive with Major Axis Horizontal.
$\beta = 0$.

115

Figure B.6. Pitching and Yawing Moment Variation with Angle of Attack for Elliptical Ogive with Major Axis Horizontal. $\beta = 0$.

116

Figure B.7. Normal and Side Force Variation with Sideslip for Elliptical Ogive with Major Axis Horizontal.

117

Figure B.8. Pitching and Yawing Moment Variation with Sideslip for
Elliptical Ogive with Major Axis Horizontal.
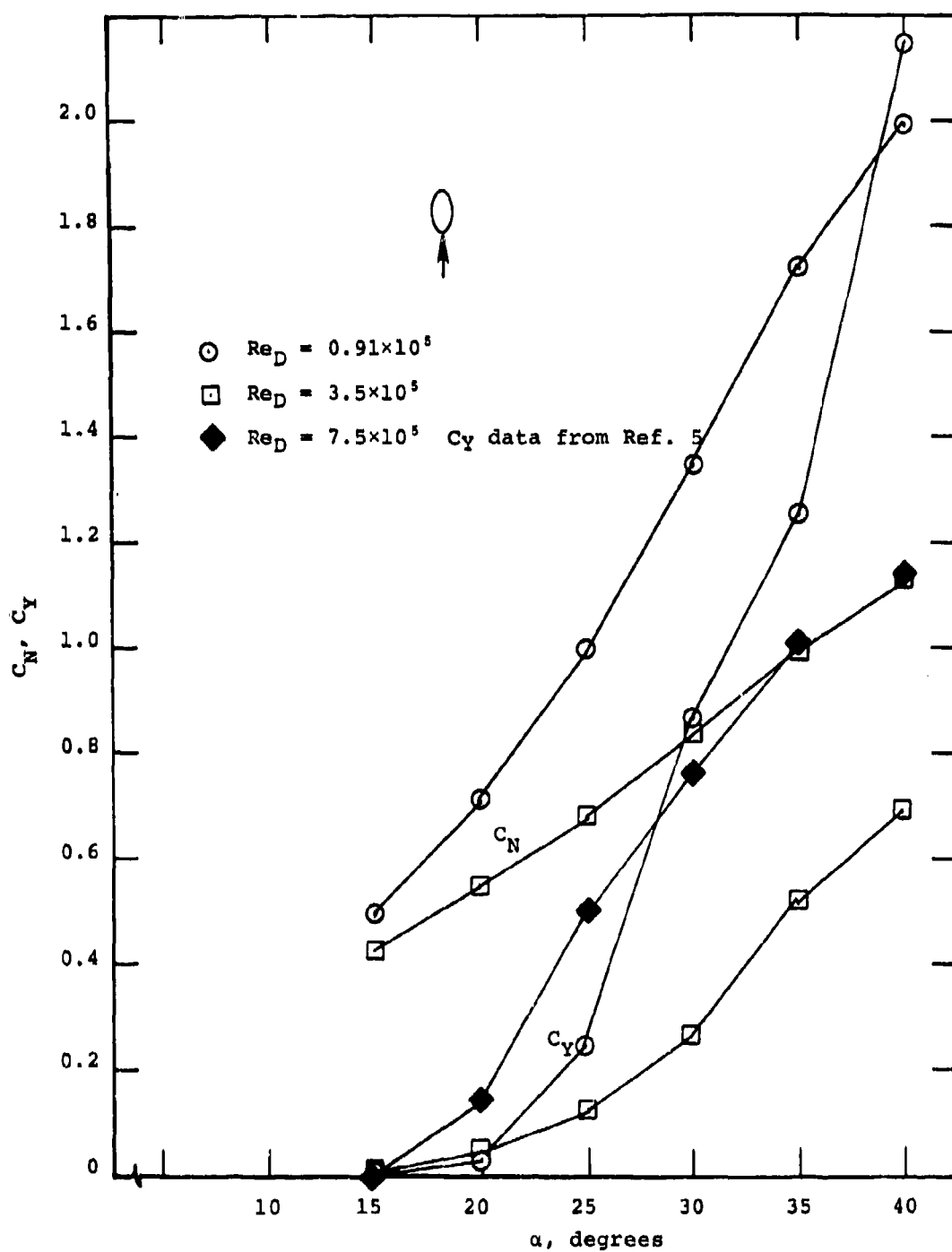
Figure B.9. Normal and Side Force Variation with Angle of Attack for Elliptical Ogive with Major Axis Vertical. β = 0.
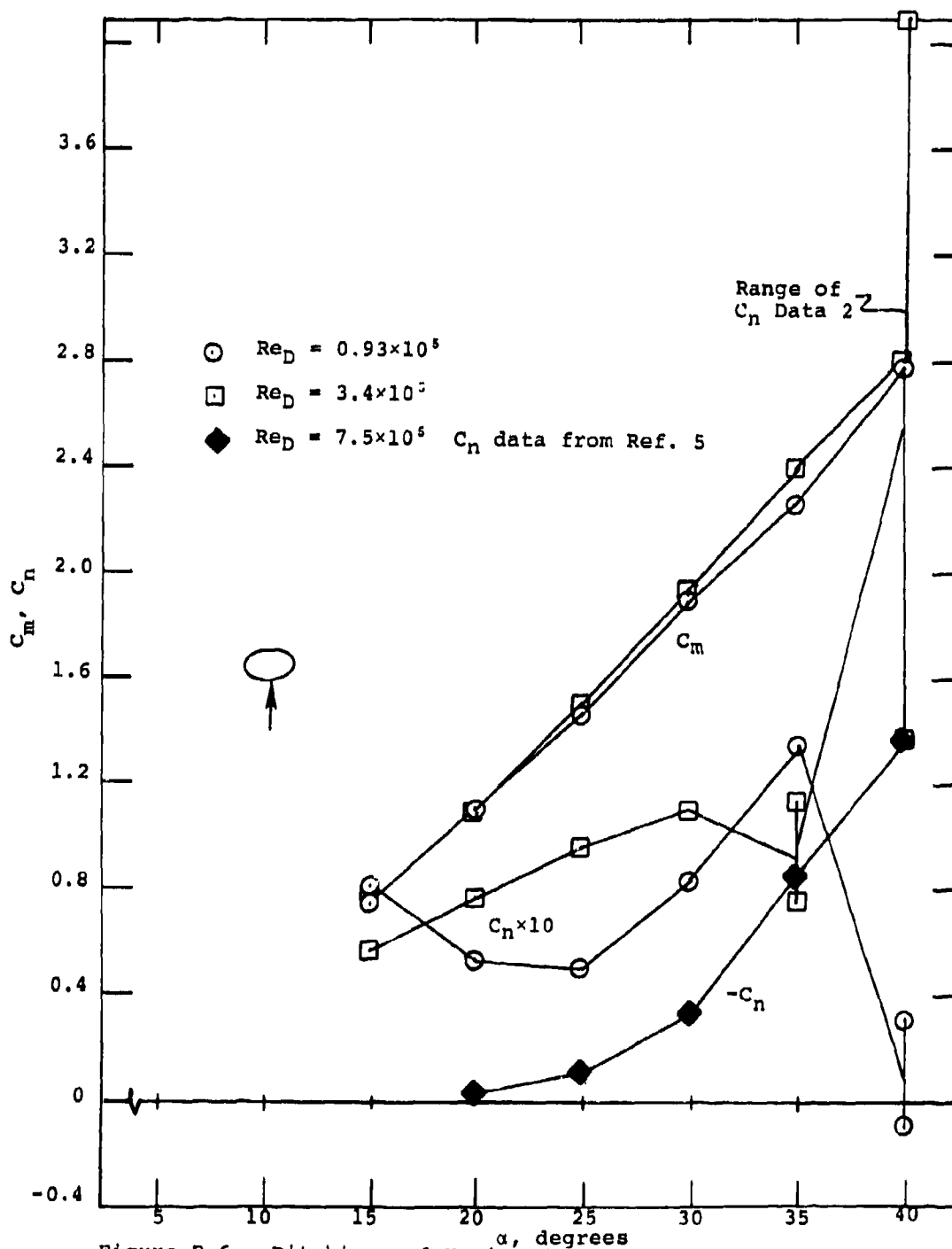
119

Figure B.10.   Pitching and Yawing Moment Variation with Angle of
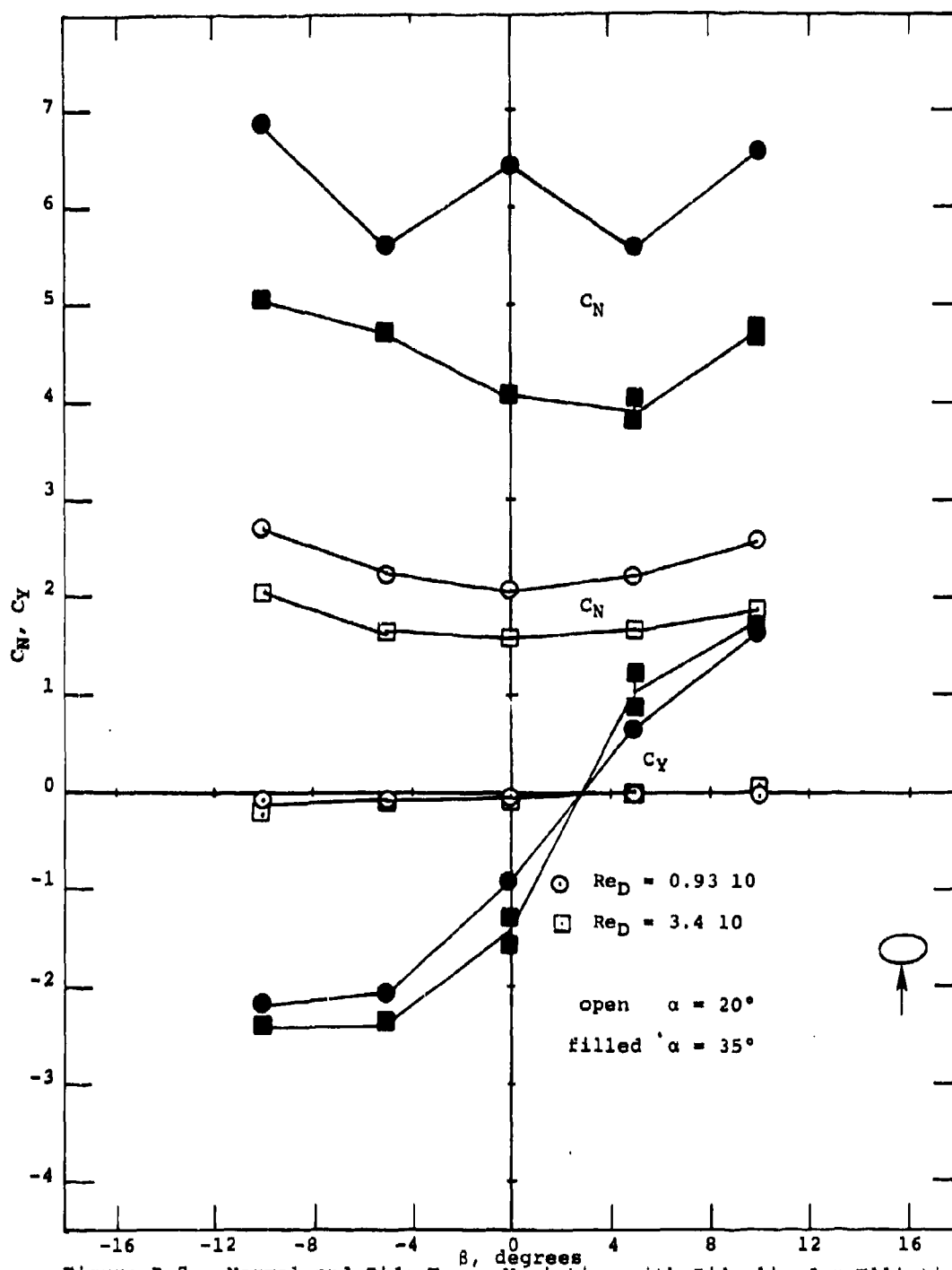Attack for Elliptical Ogive with Major Axis Vertical. $\beta = 0$.
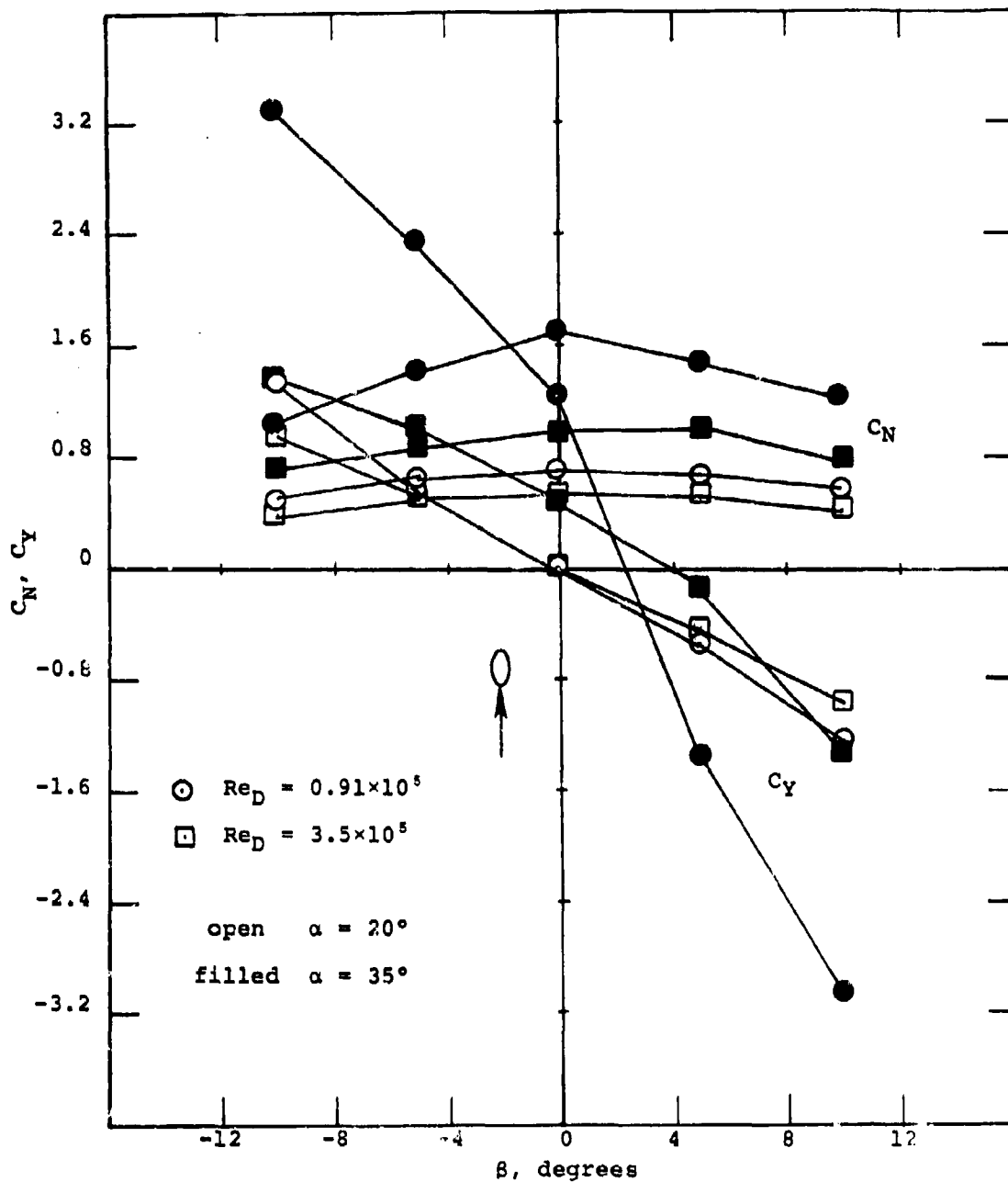
Figure B.11. Normal and Side Force Variation with Sideslip for
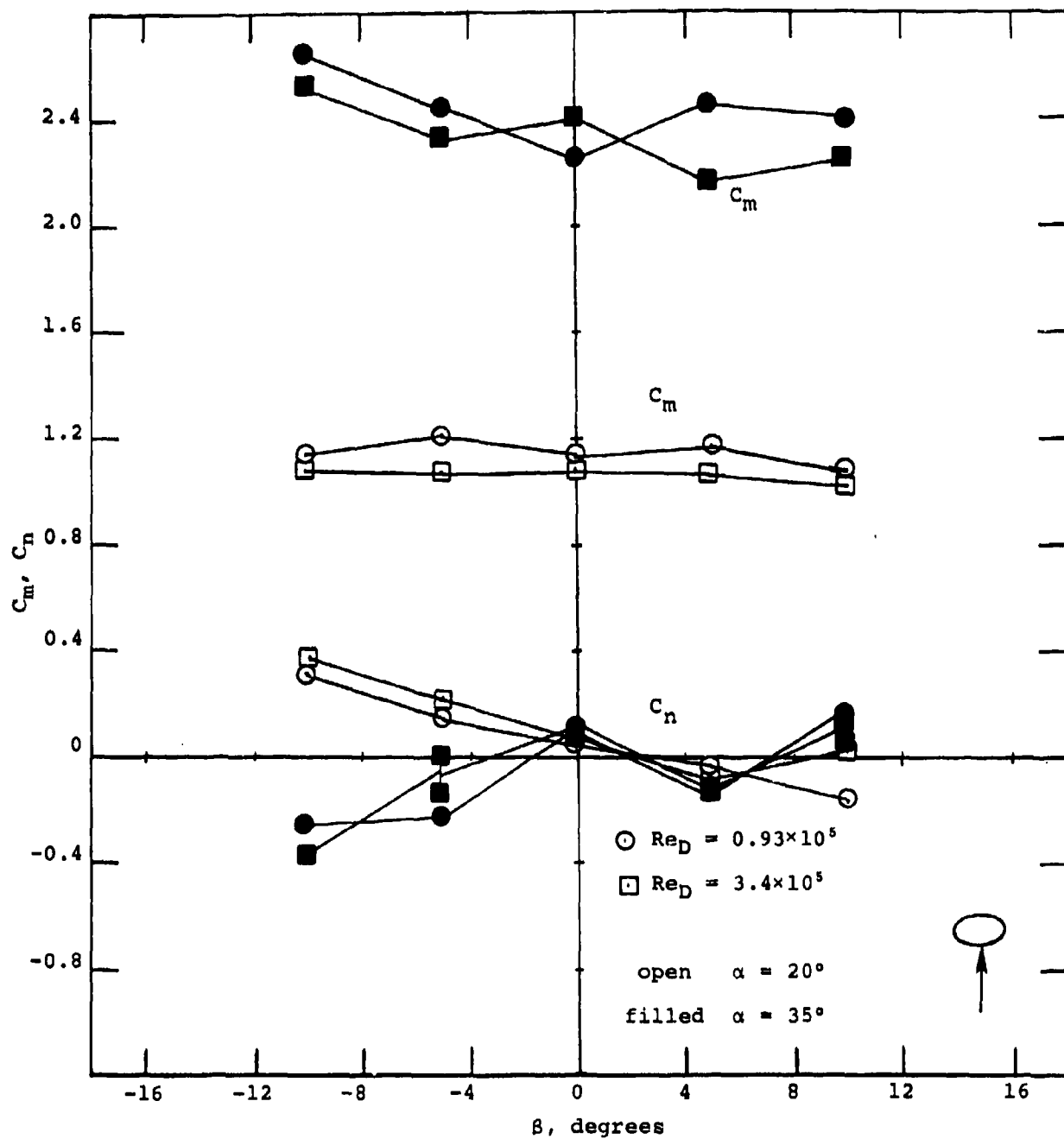Elliptical Ogive with Major Axis Vertical.

121
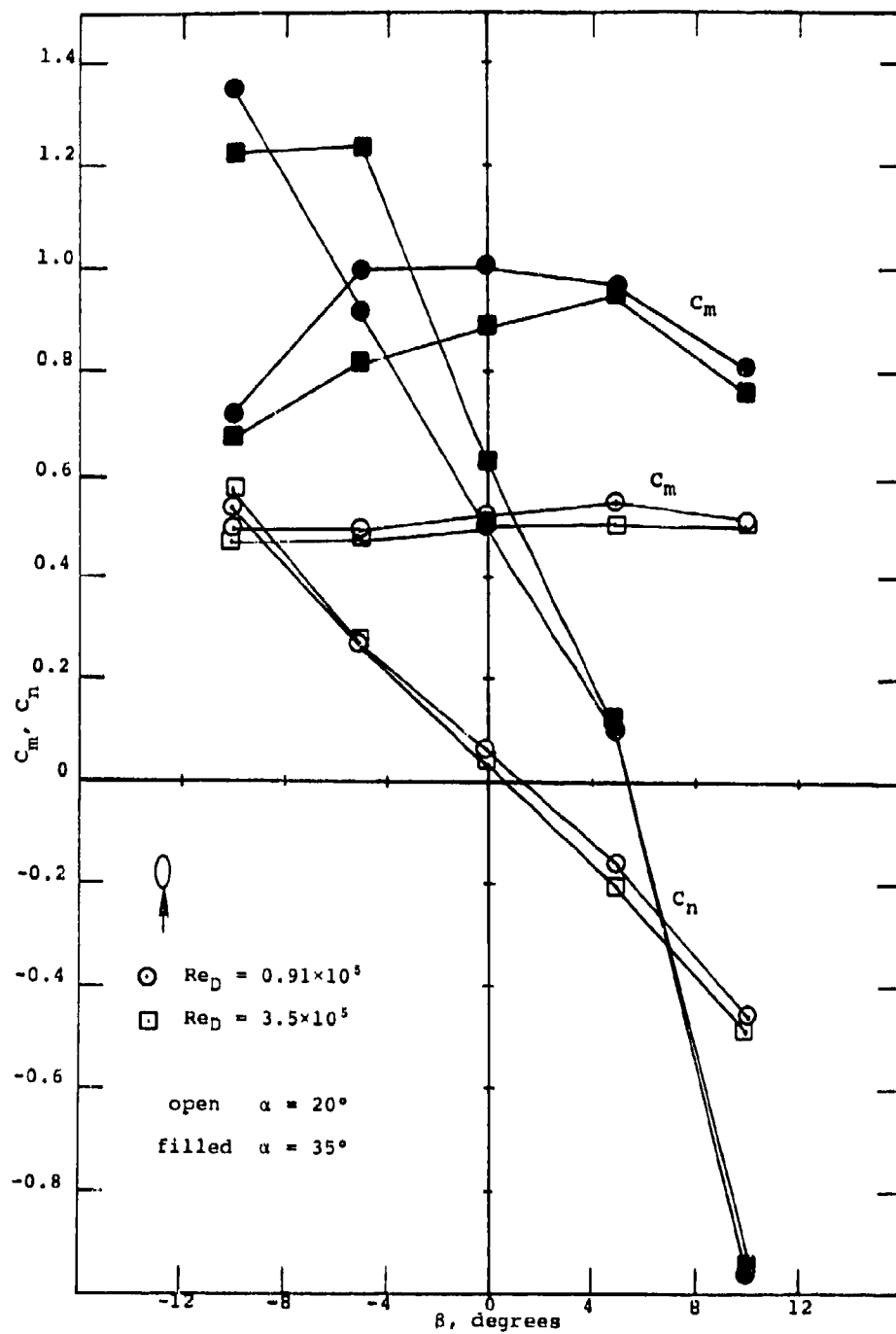
Figure B.12. Pitching and Yawing Moment Variation with Sideslip for Elliptical Ogive with Major Axis Vertical.
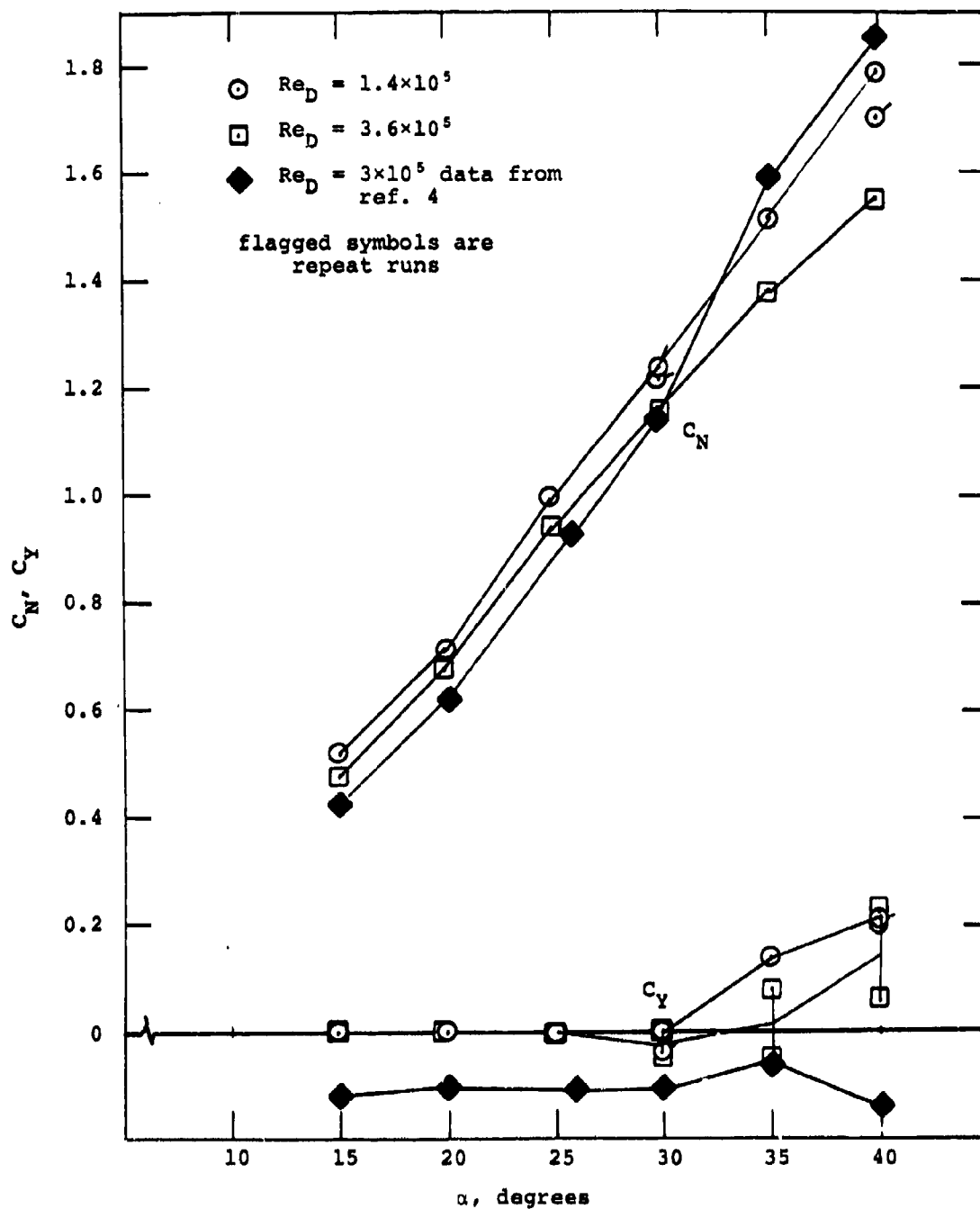
Figure B.13. Normal and Side Force Variation with Angle of
Attack for F-5 Nose. β = 0
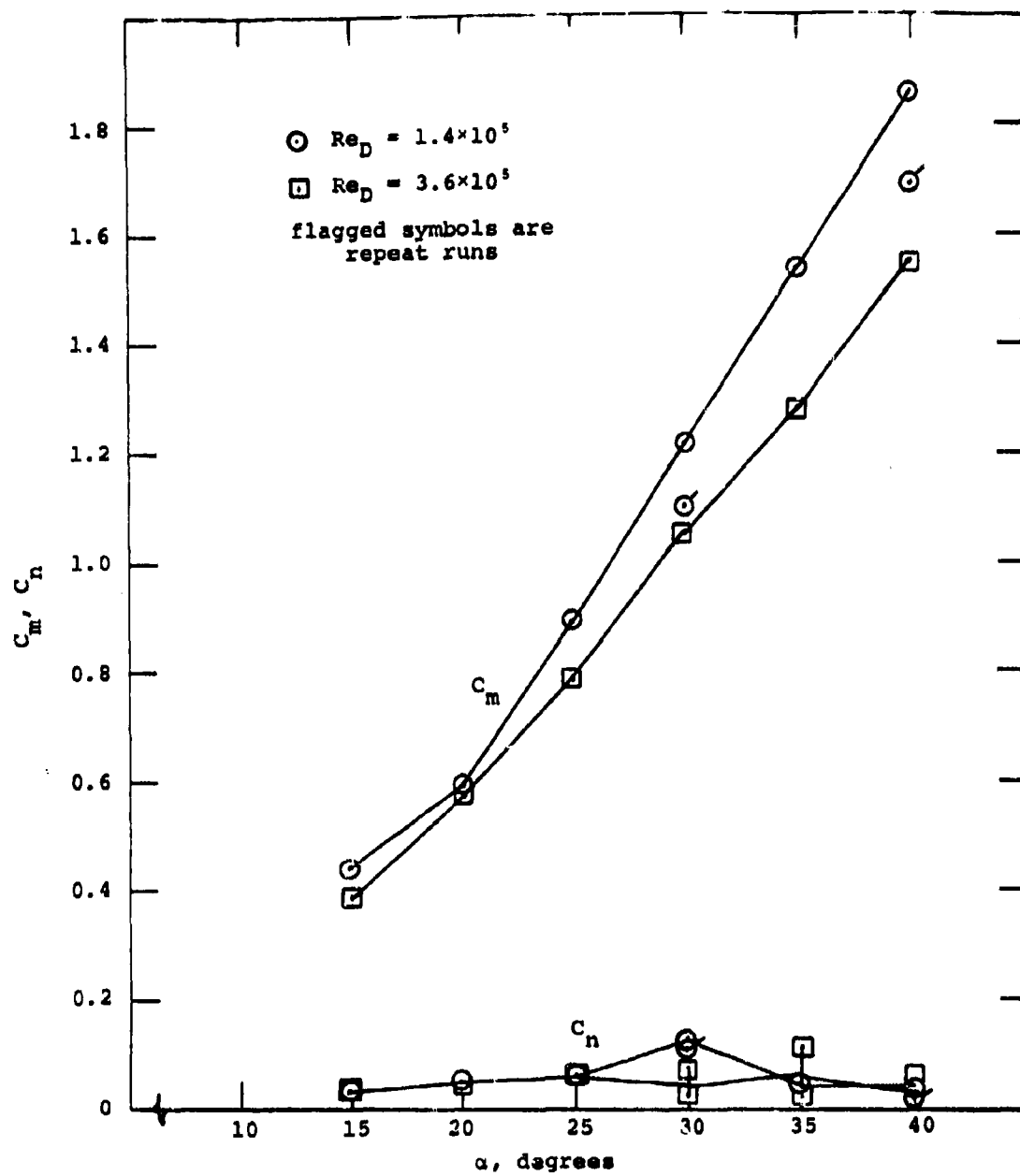
Figure B.14. Pitching and Yawing Moment Variation with Angle
of Attack for F-5 Nose. $\beta = 0$
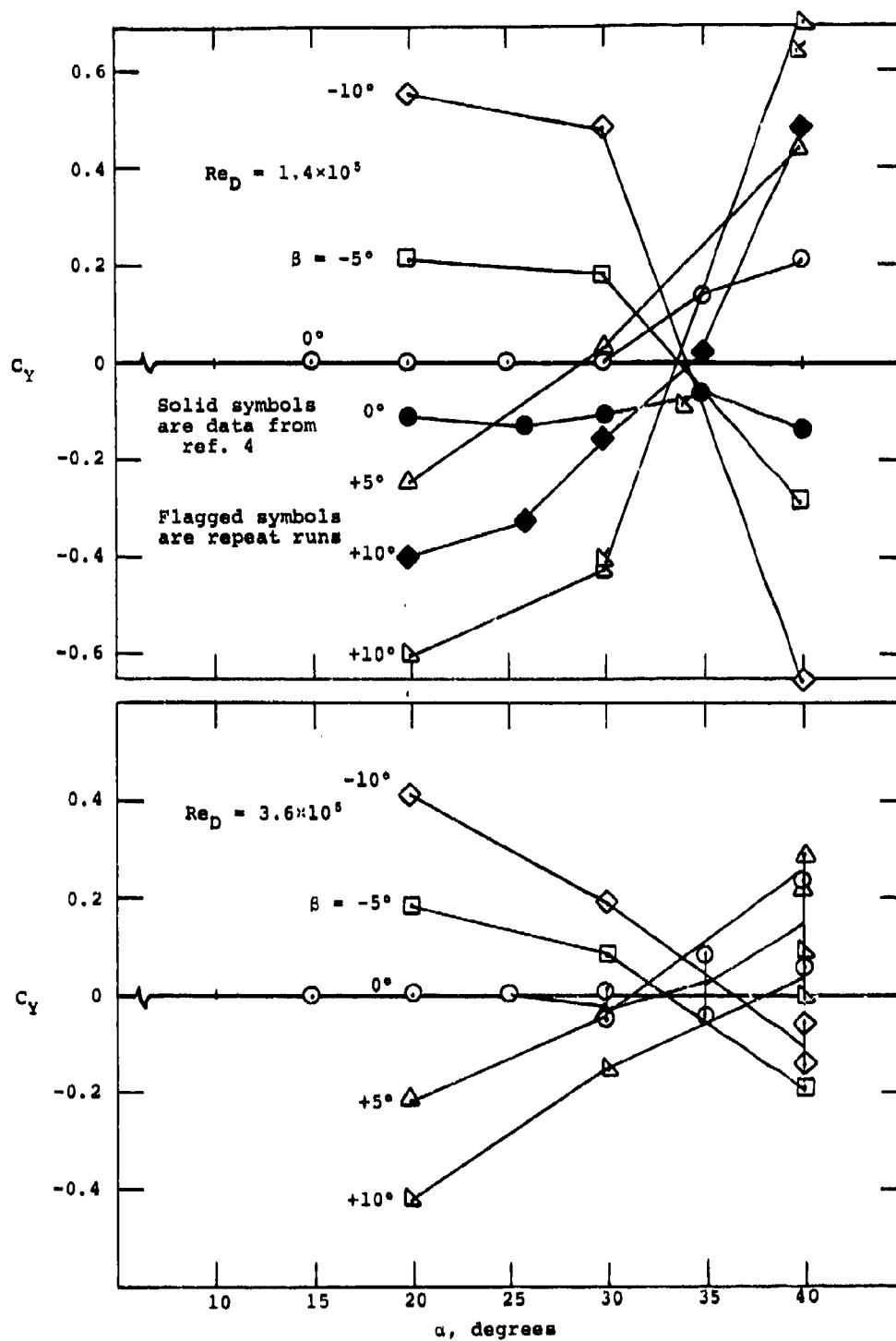
Figure B.15.   Side Force Variation with Angle of Attack for Several
Sideslip Angles for F-5 Nose.
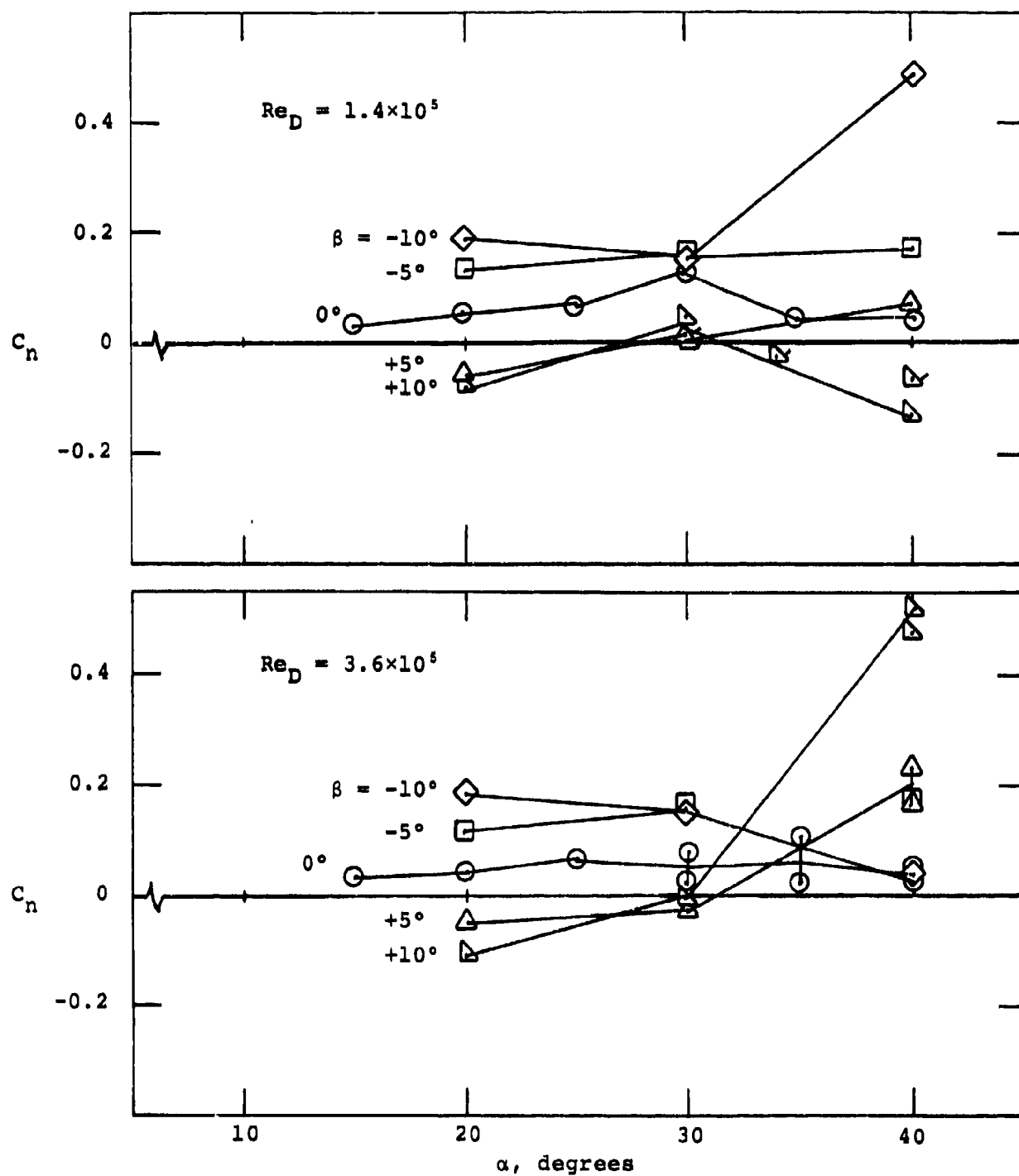
Figure B.16.   Yawing Moment Variation with Angle of Attack
for Several Sideslip Angles for F-5 Nose.
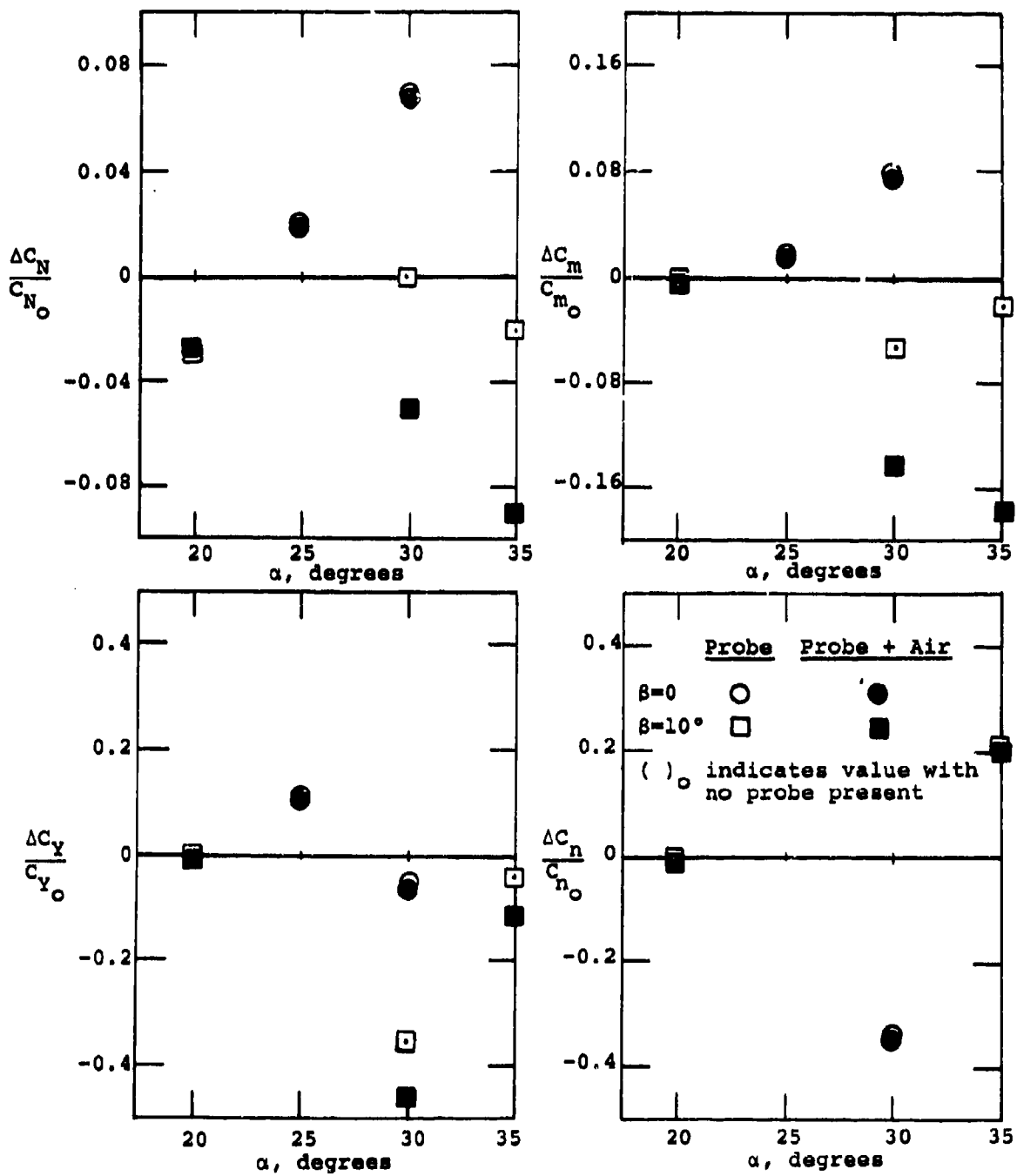
Figure B.17. Force and Moment Changes on V/STOL Nose Due to
Probe with and without Air.
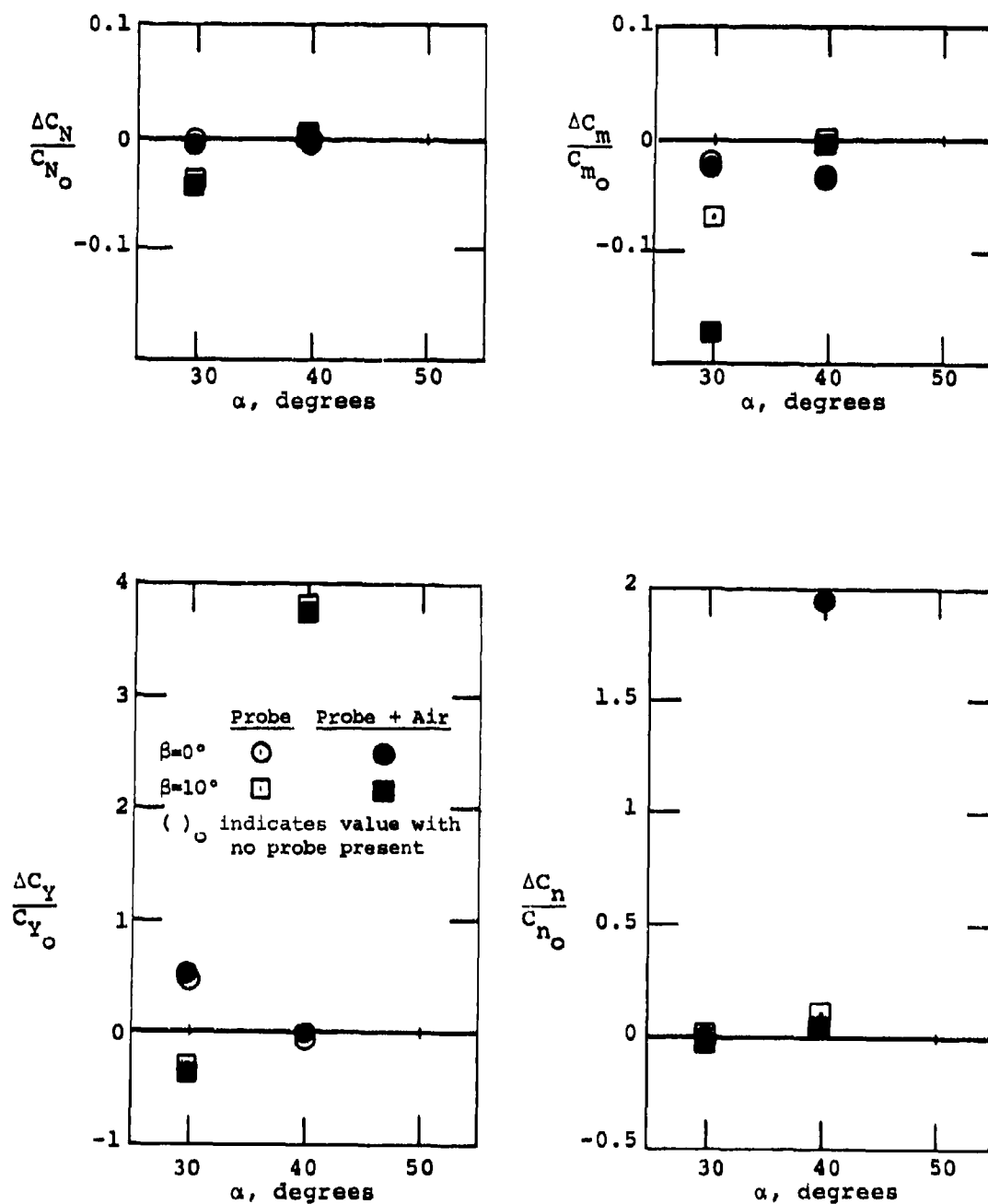
Figure B.18. Force and Moment Changes on Elliptic Ogive Nose. Major Axis Horizontal, Due to Probe with and without Air.
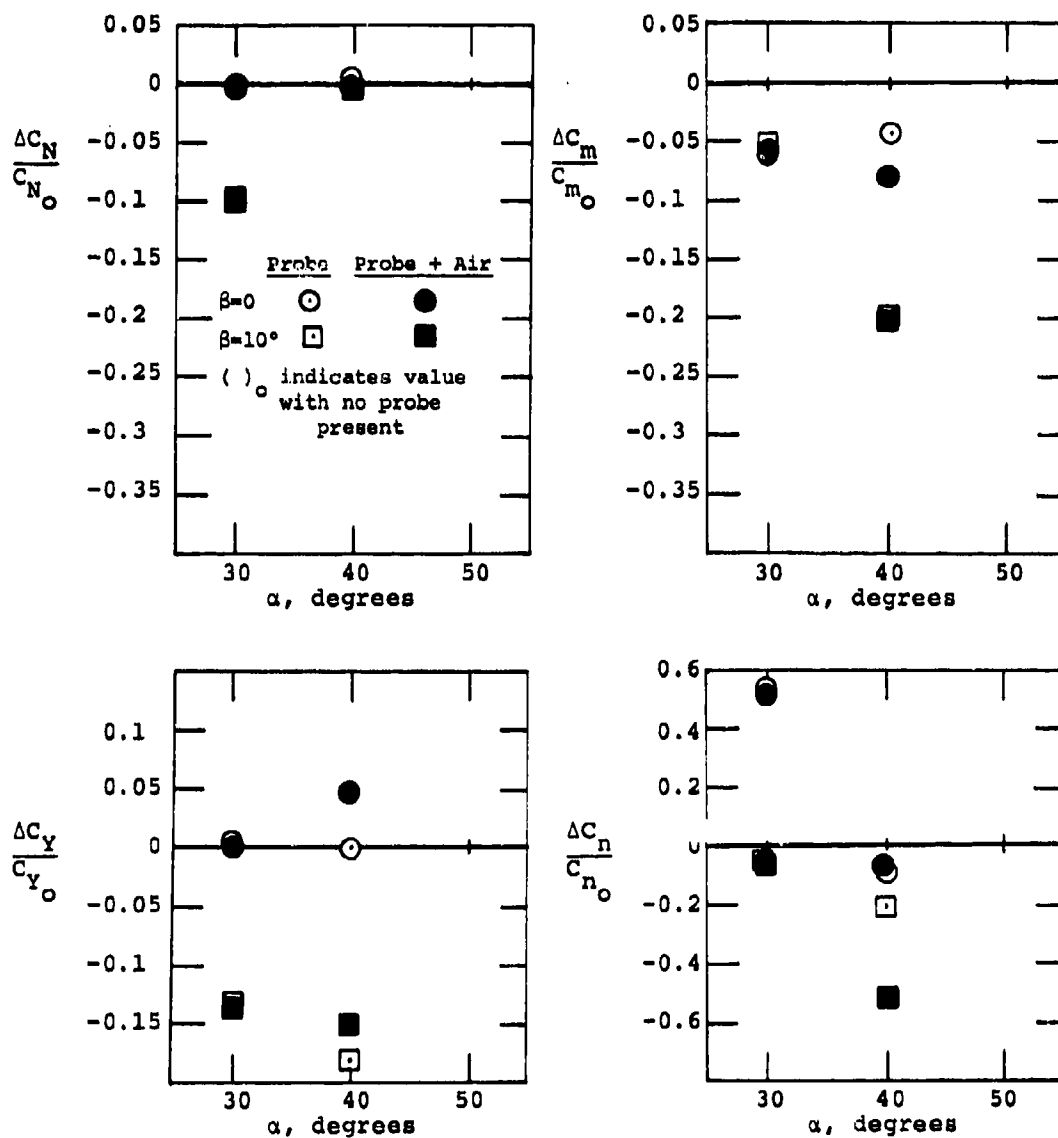
Figure B.19. Force and Moment Changes on Elliptic Ogive Nose.
Major Axis Vertical, Due to Probe with and without Air.

129
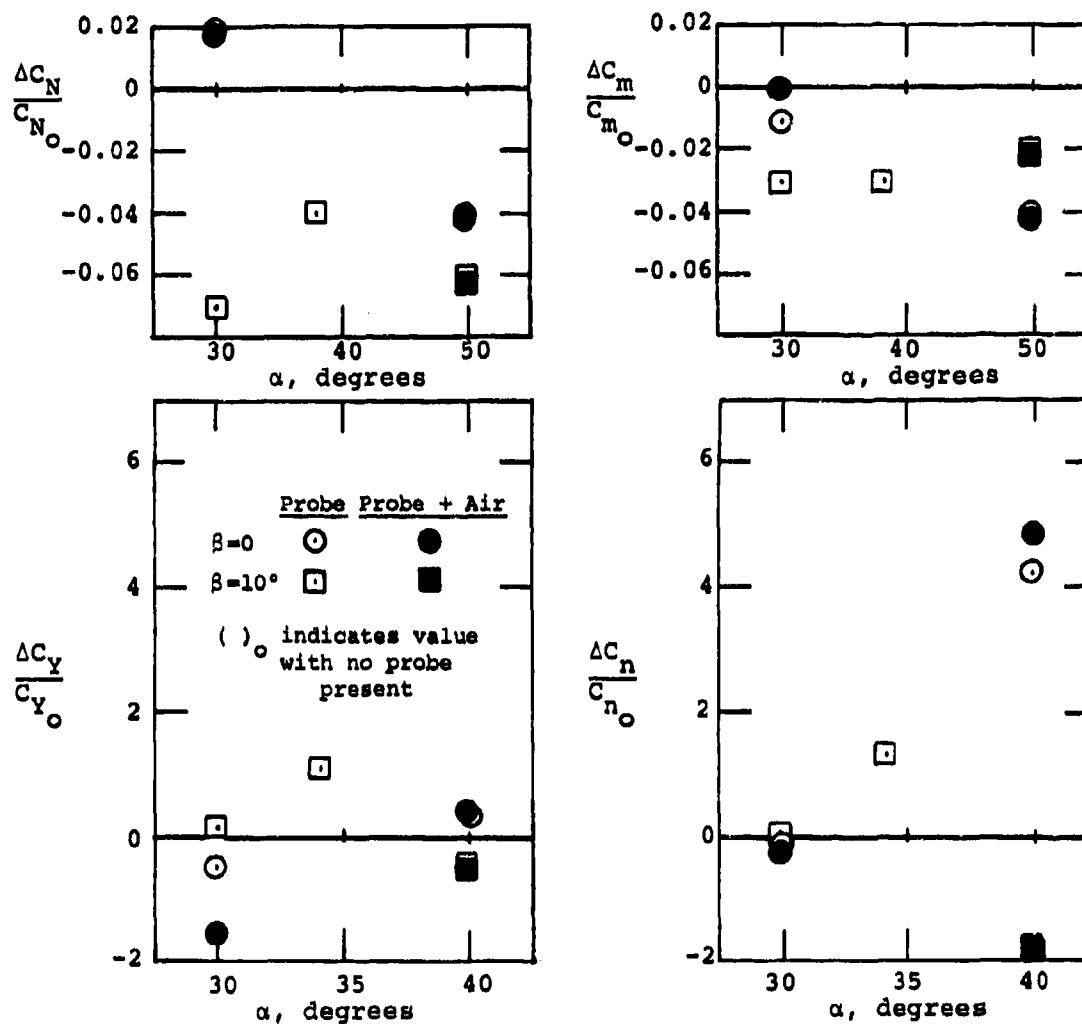
Figure B.20. Force and Moment Changes on F-5 Nose
Due to Probe with and without Air.
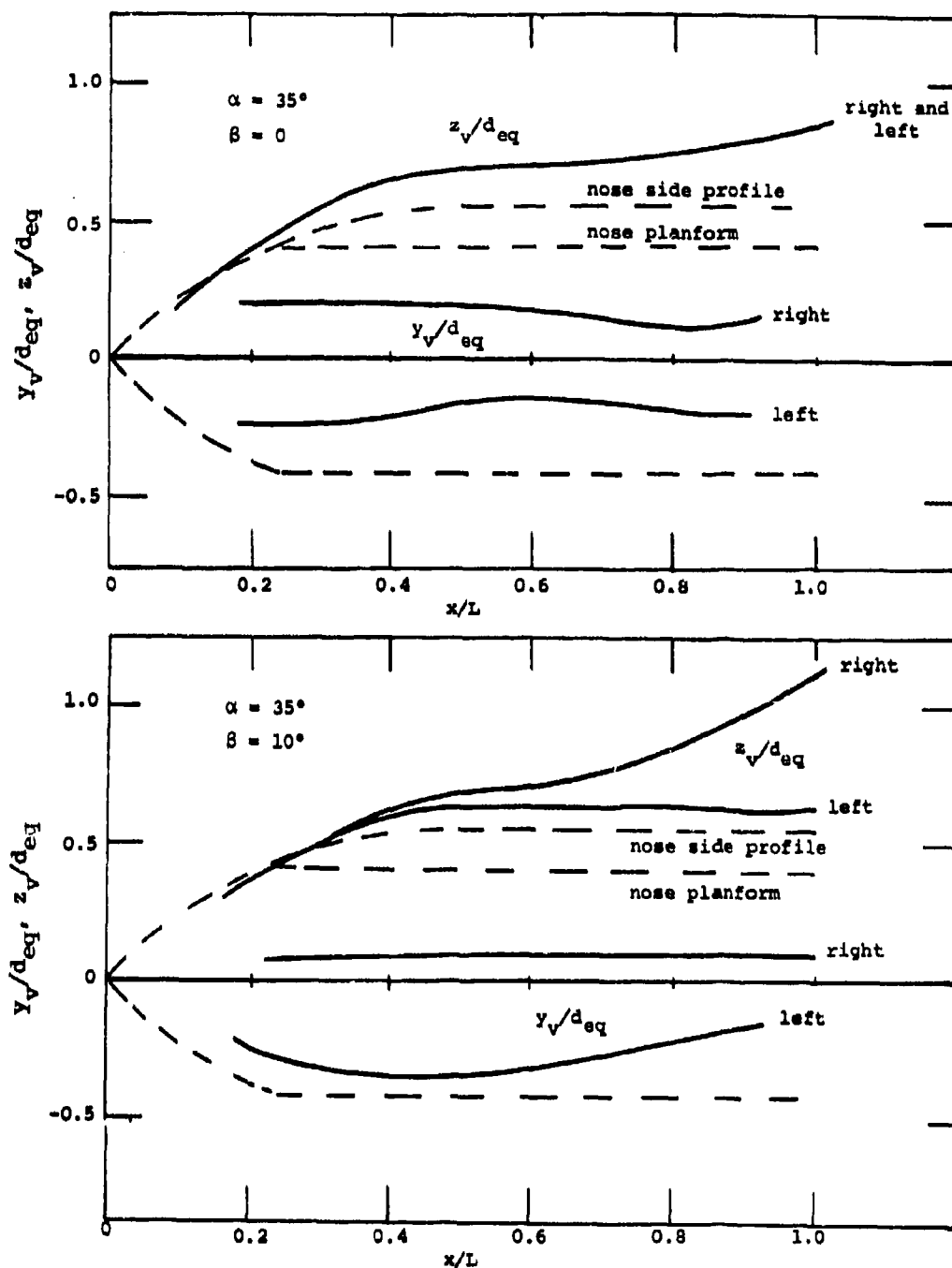
Figure B.21. Measured Vortex Positions on V/STOL Nose.
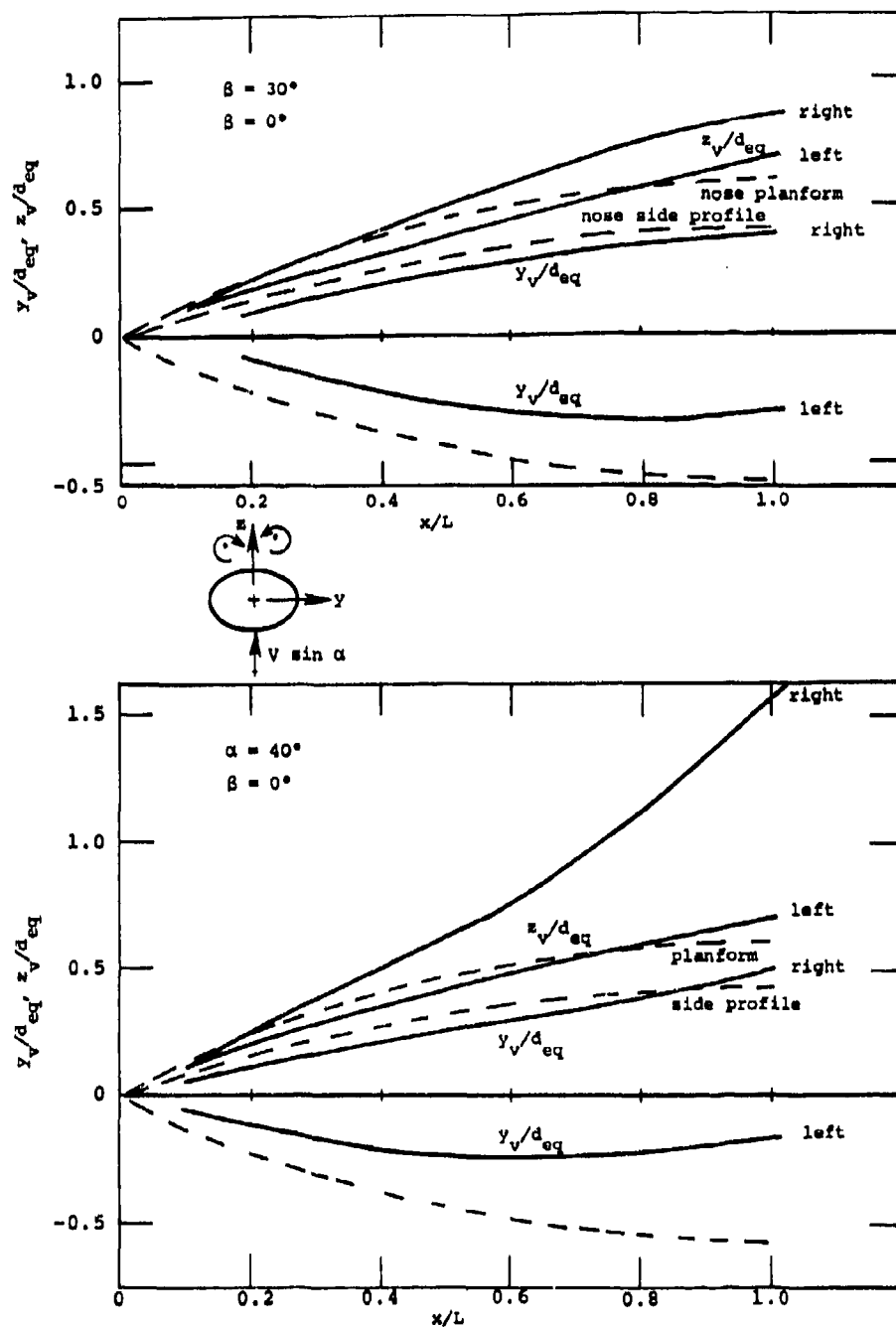
Figure B.22.   Measured Vortex Positions on Elliptic Ogive
with Major Axis Horizontal.

132
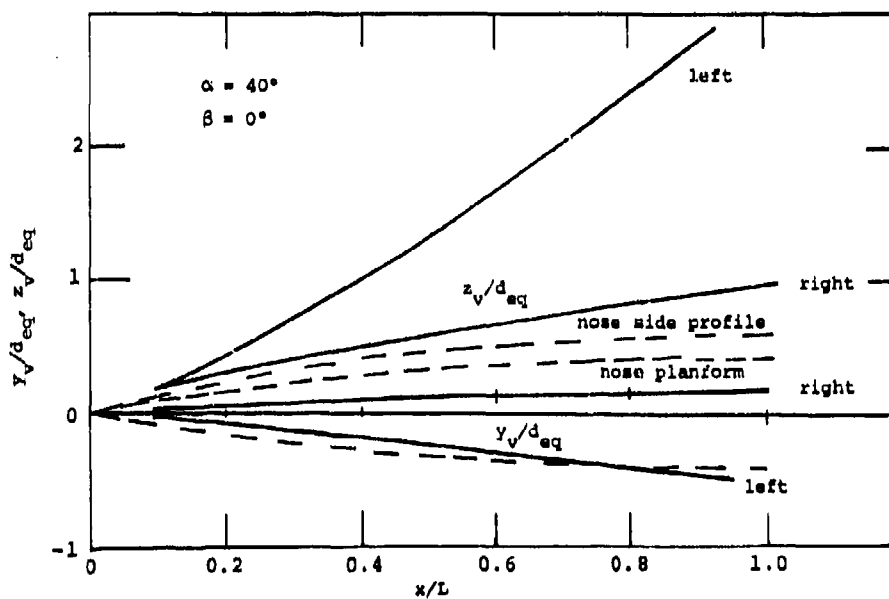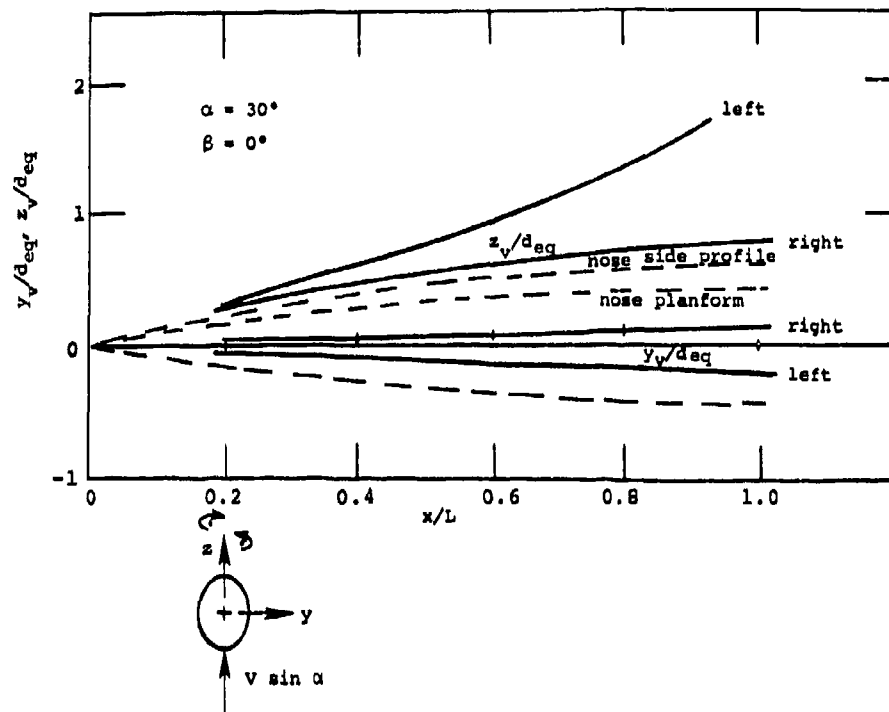
Figure B.23. Measured Vortex Positions on Elliptic Ogive
with Major Axis Vertical.
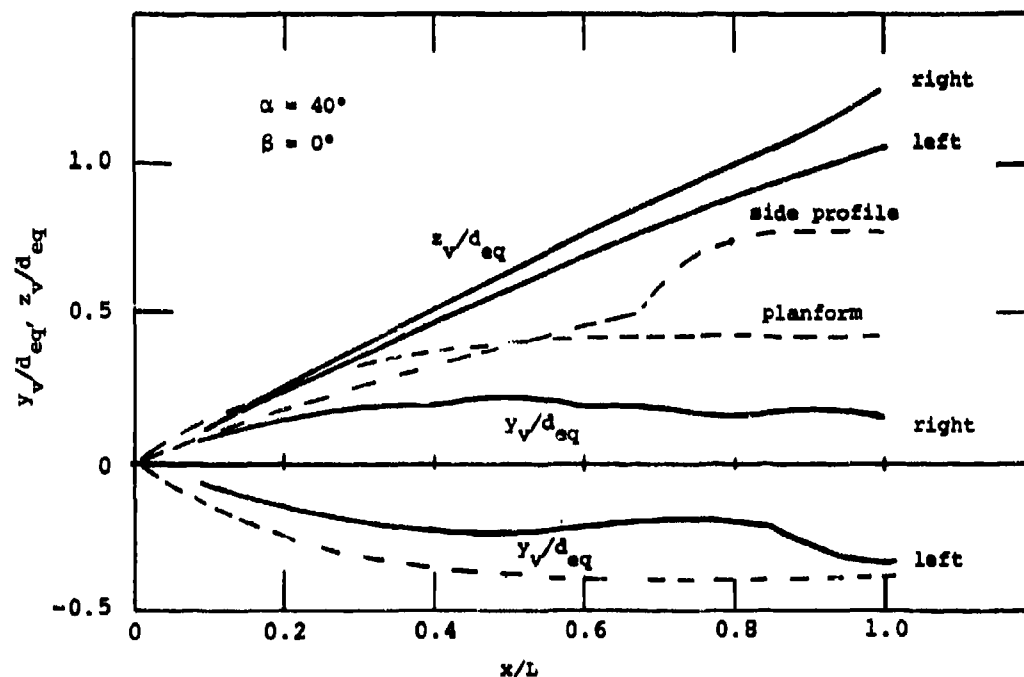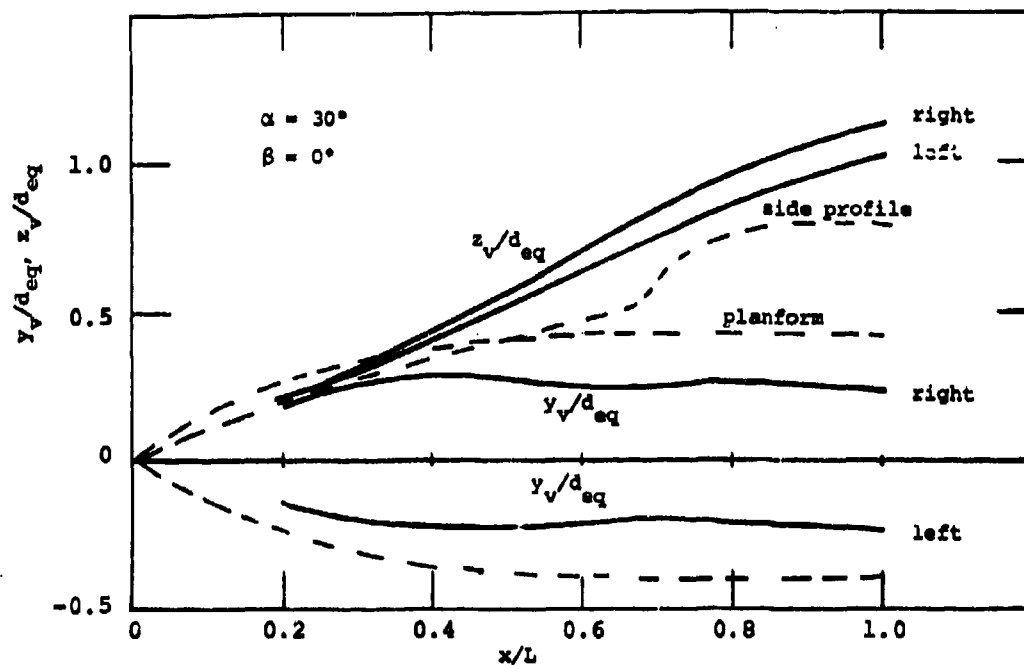
Figure B.24. Measured Vortex Positions on F-5 Nose.

134
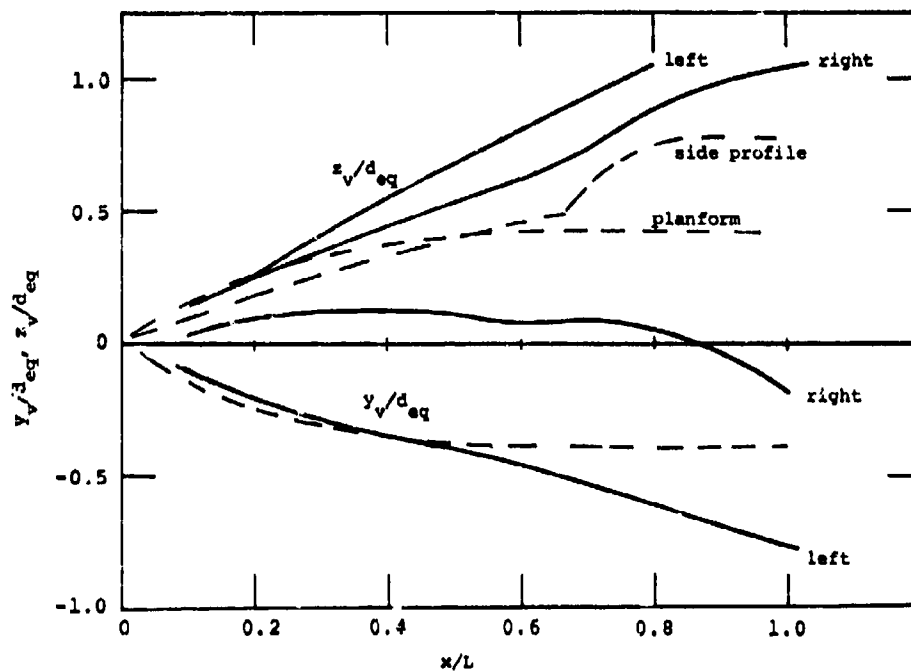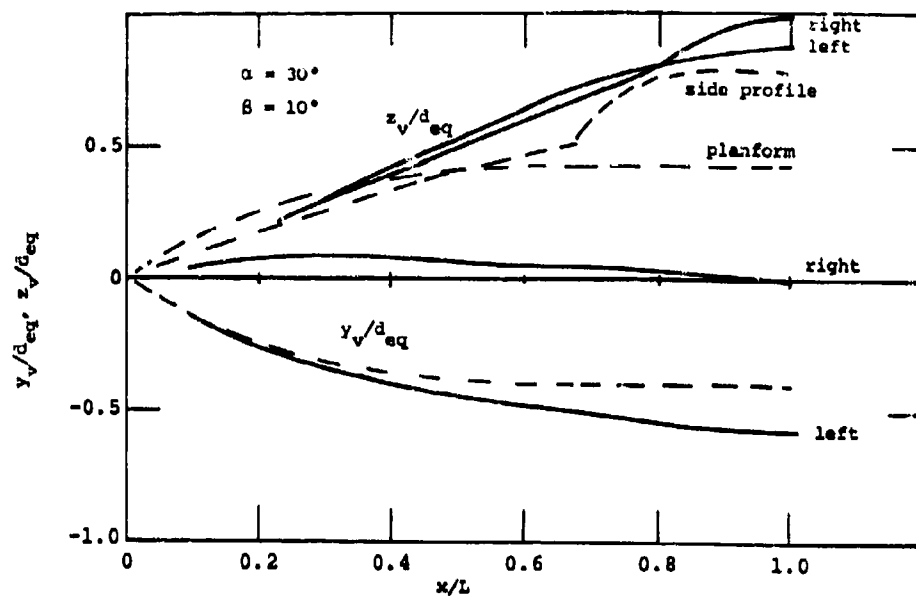
Figure B.25. Measured Vortex Positions on F-5 Nose.

135

APPENDIX C
MAPPING OF CORRESPONDING POINTS BETWEEN
THE REAL PLANE AND THE CIRCLE PLANE
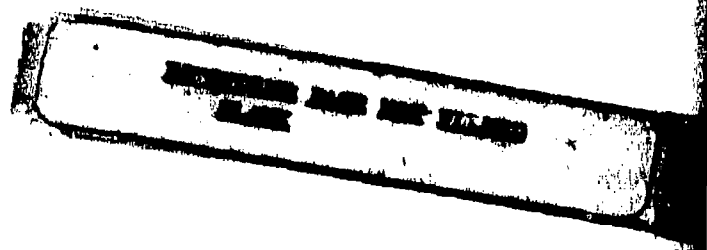
Introduction

Calculation of the potential flow field around an arbitrary shaped body and prediction of the motion of free vortices in the vicinity of the body require that corresponding points in each plane be readily obtainable. From Figure 11, the position vectors in each plane are written as

$$\nu = \tau + i\lambda$$
$$= r_o e^{-i\theta} \tag{C.1}$$

and

$$\sigma = y + iz$$
$$= -ise^{i\beta} \tag{C.2}$$

Given the transformation from equation (1),

$$\frac{d\sigma}{d\nu} = \exp\left(\sum_{n=0}^{N} \frac{A_n - iB_n}{\nu^n} \right) \tag{C.3}$$

where

$$\nu^n = r_o^n e^{-in\theta} \tag{C.4}$$

and assuming that corresponding points σ_o and ν_o are known, the various required mapping procedures are carried out as follows.

Map Known Points on the Circle to the Corresponding Points on Body

Given the point ν_1 on the circle (Fig. 11), determine the corresponding point σ_1 on the body as follows. From equations (C.1) and (C.2)

$$d\nu = -r_o i e^{-i\theta} d\theta \tag{C.5}$$

$$d\sigma = -i \, ds \, e^{i\beta} + s \, d\beta \, e^{i\beta}$$
$$= (s \, d\beta \cos \beta + ds \sin \beta)$$
$$+ i(s \, d\beta \sin \beta - ds \cos \beta) \tag{C.6}$$
$$= dy + i \, dz \tag{C.6a}$$

138

Rewrite (C.3) using (C.5) and (C.6)

$$\frac{d\sigma}{d\nu} = \frac{s\ d\beta\ e^{i\beta} - i\ ds\ e^{i\beta}}{-i\ r_0 e^{-i\theta} d\theta} \tag{C.7}$$

$$\frac{d\sigma}{d\nu} = \left[\frac{ds}{r_0 d\theta} \cos(\theta + \beta) - \frac{s}{r_0} \frac{d\beta}{d\theta} \sin(\theta + \beta) \right]$$

$$+ i \left[\frac{ds}{r_0 d\theta} \sin(\theta + \beta) + \frac{s}{r_0} \frac{d\beta}{d\theta} \cos(\theta + \beta) \right] \tag{C.8}$$

From (C.3), define

$$R = \text{Real} \left[\exp\left(\sum_{n=0}^{N} \frac{A_n - iB_n}{\nu^n} \right) \right] \tag{C.9}$$

$$I = \text{Imag} \left[\exp\left(\sum_{n=0}^{N} \frac{A_n - iB_n}{\nu^n} \right) \right] \tag{C.10}$$

Therefore,

$$R = \frac{ds}{r_0 d\theta} \cos(\theta + \beta) - \frac{s}{r_0} \frac{d\beta}{d\theta} \sin(\theta + \beta) \tag{C.11}$$

$$I = \frac{ds}{r_0 d\theta} \sin(\theta + \beta) + \frac{s}{r_0} \frac{d\beta}{d\theta} \cos(\theta + \beta) \tag{C.12}$$

Since R and I are functions only of the known point on the circle, solve (C.11) and (C.12) to get

$$\frac{ds}{r_0 d\theta} = R \cos(\theta + \beta) + I \sin(\theta + \beta) \tag{C.13}$$

$$\frac{s}{r_0} \frac{d\beta}{d\theta} = I \cos(\theta + \beta) - R \sin(\theta + \beta) \tag{C.14}$$

From (C.6),

139

$$dy = \left[\left(\frac{s}{r_0}\frac{d\beta}{d\theta}\right)\cos\beta + \left(\frac{ds}{r_0 d\theta}\right)\sin\beta\right]r_0 d\theta \qquad (C.15)$$

$$dz = \left[\left(\frac{s}{r_0}\frac{d\beta}{d\theta}\right)\sin\beta - \left(\frac{ds}{r_0 d\theta}\right)\cos\beta\right]r_0 d\theta \qquad (C.16)$$

The coordinates on the body are

$$y_1 = y_0 + \int_{\theta_0}^{\theta_1}(dy)\,r_0 d\theta \qquad (C.17)$$

$$z_1 = z_0 + \int_{\theta_0}^{\theta_1}(dz)\,r_0 d\theta \qquad (C.18)$$

Map a Specified Point Near the Body to Its Corresponding Point Near the Circle

Considering the following sketch, given σ_2, find ν_2.

$$\sigma = y + iz \qquad\qquad\qquad \nu = \tau + i\lambda$$
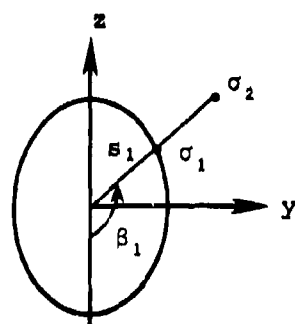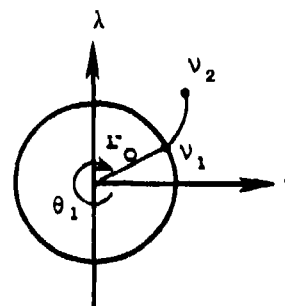
The position of σ_2 uniquely determines the point, σ_1, on the body. From the previous mapping, the corresponding point on the circle, ν_1, can be found either from a table lookup or a stepwise application of the previous mapping. The procedure to locate ν_2 is to integrate along the straight line $\overline{\sigma_1\sigma_2}$ (β = constant) and determine the corresponding curved line, $\overline{\nu_1\nu_2}$. From (C.2),

$$\sigma = -is\,e^{i\beta} \qquad (C.19)$$

140

and holding β constant,

$$d\sigma = -i \; ds \; e^{i\beta}$$
$$= dy + i \; dz \tag{C.20}$$

From (C.1),

$$\nu = re^{-i\theta} \tag{C.21}$$

and

$$dv = -ir \; d\theta \; e^{-i\theta} + dr \; e^{-i\theta}$$
$$= d\tau + i \; d\lambda \tag{C.22}$$

Expanding (C.22) results in

$$dv = (dr \cos \theta - r \; d\theta \sin \theta) - i(r \; d\theta \cos \theta + dr \sin \theta) \tag{C.23}$$

Combining (C.3) with (C.9) and (C.10),

$$\frac{d\sigma}{d\nu} = \exp\left(\sum_{n=0}^{N} \frac{A_n - iB_n}{\nu^n}\right) = R + iI \tag{C.24}$$

From (C.20) and (C.22),

$$\frac{d\nu}{d\sigma} = \frac{(dr - ir \; d\theta)e^{-i\theta}}{-i \; ds \; e^{i\beta}}$$

$$= \left(r \; \frac{d\theta}{ds} + i \; \frac{dr}{ds}\right) e^{-i(\theta+\beta)}$$

$$= \left[r \; \frac{d\theta}{ds} \cos(\theta + \beta) + \frac{dr}{ds} \sin(\theta + \beta)\right]$$

$$+ i\left[\frac{dr}{ds} \cos(\theta + \beta) - r \; \frac{d\theta}{ds} \sin(\theta + \beta)\right] \tag{C.25}$$

Let

$$\frac{d\nu}{d\sigma} = \left(\frac{1}{\frac{d\sigma}{d\nu}}\right) = P + iQ = \frac{1}{R + iI} \tag{C.26}$$

141

where

$$P = \frac{dr}{ds} \sin(\theta + \beta) + r \frac{d\theta}{ds} \cos(\theta + \beta) \qquad (C.27)$$

$$Q = \frac{dr}{ds} \cos(\theta + \beta) - r \frac{d\theta}{ds} \sin(\theta + \beta) \qquad (C.28)$$

Note that P and Q are functions of ν, but in each interval ds, ν can be treated as constant. In the numerical integration, some error is introduced, but the results will converge as ds is smaller. Solving (C.27) and (C.28), we get

$$\frac{dr}{ds} = P \sin(\theta + \beta) + Q \cos(\theta + \beta) \qquad (C.29)$$

$$r \frac{d\theta}{ds} = P \cos(\theta + \beta) - Q \sin(\theta + \beta) \qquad (C.30)$$

Combining (C.22), (C.23), (C.29), and (C.30), we get

$$d\tau = \Big(\Big[P \sin(\theta + \beta) + Q \cos(\theta + \beta) \Big] \cos \theta$$
$$- \Big[P \cos(\theta + \beta) - Q \sin(\theta + \beta) \Big] \sin \theta \Big) ds \qquad (C.31)$$

$$d\lambda = \Big(\Big[-P \sin(\theta + \beta) - Q \cos(\theta + \beta) \Big] \sin \theta$$
$$- \Big[P \cos(\theta + \beta) - Q \sin(\theta + \beta) \Big] \cos \theta \Big) ds \qquad (C.32)$$

The coordinates of ν_2 are

$$\tau_2 = \tau_2 + \int_{s_1}^{s_2} \frac{d\tau}{ds} \, ds \qquad (C.33)$$

$$\lambda_2 = \lambda_1 + \int_{s_2}^{s_1} \frac{d\lambda}{ds} \, ds \qquad (C.34)$$

142

For the limited number of noncircular bodies examined, convergence of the numerical integration of (C.33) and (C.34) occurs when ds is not greater than $0.1 s_1$.

Map a Specified Point Near the Circle to Its Corresponding Point Near the Body

Considering the following sketch, given v_2, find σ_2.

$$v = \tau + i\lambda \qquad\qquad\qquad \sigma = y + iz$$
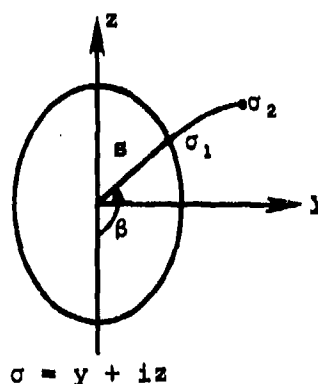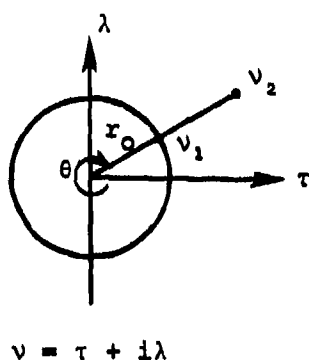
The position of v_2 uniquely determines the point v_1 on the circle. From a previous mapping, the corresponding point, σ_1, on the body is found from integration of equations (C.17) and (C.18). The procedure to locate σ_2 is to integrate along the straight line $\overline{v_1 v_2}$ (θ = constant) and determine the corresponding curve defined by $\overline{\sigma_1 \sigma_2}$. Let

$$v = r \, e^{-i\theta} \qquad\qquad\qquad\qquad (C.35)$$

and

$$dv = dr \, e^{-i\theta} \qquad\qquad\qquad\qquad (C.36)$$

143

From (C.2),

$$\sigma = -is\, e^{i\beta} \tag{C.37}$$

and from (C.6),

$$d\sigma = (s\, d\beta - i\, ds)e^{i\beta} \tag{C.38}$$

The transformation, from (C.3)

$$\frac{d\sigma}{d\nu} = \exp\left(\sum_{n=0}^{N} \frac{A_n - iB_n}{\nu^n}\right) = R + iI$$

where

$$\nu^n = r^n e^{-in\theta} \tag{C.40}$$

can also be written in terms of (C.36) and (C.38)

$$\frac{d\sigma}{d\nu} = \frac{(s\, d\beta - i\, ds)e^{i\beta}}{dr\, e^{-i\theta}}$$

$$= \left[s\frac{d\beta}{dr}\cos(\theta + \beta) + \frac{ds}{dr}\sin(\theta + \beta) \right]$$

$$+ i\left[s\frac{d\beta}{dr}\sin(\theta + \beta) - \frac{ds}{dr}\cos(\theta + \beta) \right] \tag{C.41}$$

From (C.39) and (C.41),

$$R = s\frac{d\beta}{dr}\cos(\theta + \beta) + \frac{ds}{dr}\sin(\theta + \beta) \tag{C.42}$$

$$I = s\frac{d\beta}{dr}\sin(\theta + \beta) - \frac{ds}{dr}\cos(\theta + \beta) \tag{C.43}$$

where R and I are functions of r only from (C.39). Solving (C.42)
and (C.43) results in

$$s \frac{d\beta}{dr} = R \cos(\theta + \beta) + I \sin(\theta + \beta) \qquad \text{(C.44)}$$

$$\frac{ds}{dr} = R \sin(\theta + \beta) - I \cos(\theta + \beta) \qquad \text{(C.45)}$$

From (C.38)

$$d\sigma = (s \, d\beta \cos \beta + ds \sin \beta)$$
$$+ i(s \, d\beta \sin \beta - ds \cos \beta)$$
$$= dy + i \, dz \qquad \text{(C.46)}$$

Therefore,

$$dy = s \, d\beta \cos \beta + ds \sin \beta \qquad \text{(C.47)}$$

$$dz = s \, d\beta \sin \beta - ds \cos \beta \qquad \text{(C.48)}$$

Combining (C.44), (C.45), (c.47), and (C.48)

$$dy = \left(\left[R \cos(\theta + \beta) + I \sin(\theta + \beta) \right] \cos \beta \right.$$
$$\left. + \left[R \sin(\theta + \beta) - I \cos(\theta + \beta) \right] \sin \beta \right) dr \qquad \text{(C.49)}$$

$$dz = \left(\left[R \cos(\theta + \beta) + I \sin(\theta + \beta) \right] \sin \beta \right.$$
$$\left. - \left[R \sin(\theta + \beta) - I \cos(\theta + \beta) \right] \cos \beta \right) dr \qquad \text{(C.50)}$$

Finally, the coordinates of the point σ_2 are

$$Y_2 = Y_1 + \int_{r_1}^{r_2} \left(\frac{dy}{dr} \right) dr \qquad \text{(C.51)}$$

$$z_2 = z_1 + \int_{r_1}^{r_2} \left(\frac{dz}{dr} \right) dr \qquad \text{(C.52)}$$

which are obtained by numerical integration. Note that dy and dz require values of β along the path of integration. It has been found that in integration in a stepwise fashion with small dr steps, the

145

value of β from the previous step can be used. This introduces only a small error in the final results.

146

APPENDIX D
THE UNSTEADY PRESSURE DISTRIBUTION ON
GROWING BODIES UNDER THE INFLUENCE OF
FREE VORTICES

The Bernoulli equation, written as

$$p_\infty + \frac{1}{2}\rho V_\infty^2 + \rho \left.\frac{d\phi}{dt}\right|_\infty = p + \frac{1}{2}\rho U^2 + \rho \left.\frac{d\phi}{dt}\right|_{r_o} \qquad \text{(D.1)}$$

requires evaluation of the unsteady pressure term at infinity and on the body surface. The velocity potential from equation (8) is

$$\phi = \text{Real } W(\sigma) \qquad \text{(D.2)}$$

where the complex potential from equation (17) is

$$W(\sigma) = -(V \sin \beta)\left(\nu + \frac{r_o^2}{\nu}\right) - i(V \sin \alpha)\left(\nu - \frac{r_o^2}{\nu}\right)$$

$$+ i \sum_{n=1}^{N} \frac{\Gamma_n}{2\pi} \ln \left(\frac{\nu - \dfrac{r_o^2}{\nu_n}}{\nu - \nu_n}\right) + (V \cos \alpha) r_o \frac{dr_o}{dx} \ln \nu \qquad \text{(D.3)}$$

Now we need

$$\frac{d\phi}{dt} = \frac{d}{dt} [\text{Real } W(\sigma)] \qquad \text{(D.4)}$$

Let

$$\nu = \tau + i\lambda \qquad \text{(D.5)}$$

and consider one term of (D.3) at a time. Starting with the β-crossflow term,

$$W(\sigma)_\beta = -V \sin \beta \left[\tau\left(1 + \frac{r_o^2}{\tau^2 + \lambda^2}\right) + i\lambda\left(1 - \frac{r_o^2}{\tau^2 + \lambda^2}\right)\right] \qquad \text{(D.6)}$$

applying equation (D.4) produces

$$\frac{d\phi_\beta}{dt} = -V \sin \beta \left(\frac{2\tau}{\tau^2 + \lambda^2} r_o \dot{r}_o\right) \qquad \text{(D.7)}$$

The α-crossflow term in (D.3) is

$$W(\sigma)_\alpha = -iV \sin \alpha \left[\tau\left(1 - \frac{r_o^2}{\tau^2 + \lambda^2}\right) + i\lambda\left(1 + \frac{r_o^2}{\tau^2 + \lambda^2}\right)\right] \qquad \text{(D.8)}$$

148

which results in

$$\frac{d\phi_\alpha}{dt} = V \sin \alpha \left(\frac{2\lambda}{\tau^2 + \lambda^2} \, r_o \dot{r}_o \right) \tag{D.9}$$

The Γ_n term in (D.3) is

$$W(\sigma)_\Gamma = i \sum_{n=1}^{N} \frac{\Gamma_n}{2\pi} \left\{ \ln\left[\left(\tau - \frac{r_o^2 \, \tau_n}{\tau_n^2 + \lambda_n^2} \right) + i\left(\lambda - \frac{r_o^2 \, \lambda_n}{\tau_n^2 + \lambda_n^2} \right) \right] \right.$$
$$\left. - \ln\left[\left(\tau - \tau_n \right) + i\left(\lambda - \lambda_n \right) \right] \right\} \tag{D.10}$$

Rewriting (D.10) as

$$W(\sigma)_\Gamma = i \sum_{n=1}^{N} \frac{\Gamma_n}{2\pi} \left[\ln(pe^{iq}) - \ln(re^{is}) \right] \tag{D.11}$$

where

$$p = \left[\left(\tau - \frac{r_o^2 \, \tau_n}{\tau_n^2 + \lambda_n^2} \right)^2 + \left(\lambda - \frac{r_o^2 \, \lambda_n}{\tau_n^2 + \lambda_n^2} \right)^2 \right]^{1/2} \tag{D.12}$$

$$q = \tan^{-1} \left[\frac{\lambda - \left(\dfrac{r_o^2 \, \lambda_n}{\tau_n^2 + \lambda_n^2} \right)}{\tau - \left(\dfrac{r_o^2 \, \lambda_n}{\tau_n^2 + \lambda_n^2} \right)} \right] \tag{D.13}$$

$$r = \left[\left(\tau - \tau_n \right)^2 + \left(\lambda - \lambda_n \right)^2 \right]^{1/2} \tag{D.14}$$

$$s = \tan^{-1} \left(\frac{\lambda - \lambda_n}{\tau - \tau_n} \right) \tag{D.15}$$

Therefore,

$$\text{Real } W(\sigma)_\Gamma = \sum_{n=1}^{N} \frac{\Gamma_n}{2\pi} \, (s - q) \tag{D.16}$$

149

Assuming Γ_n is constant,

$$\frac{d\phi_\Gamma}{dt} = \sum_{n=1}^{N} \frac{\Gamma_n}{2\pi} \left(\frac{ds}{dt} - \frac{d\sigma}{dt}\right) \tag{D.17}$$

which becomes

$$\frac{d\phi_\Gamma}{dt} = \sum_{n=1}^{N} \frac{\Gamma_n}{2\pi} \left\{ \left[\frac{-(\tau - \tau_n)\dot{\lambda}_n + (\lambda - \lambda_n)\dot{\tau}_n}{(\tau - \tau_n)^2 + (\lambda - \lambda_n)^2}\right] \right.$$

$$- \left[\frac{\{\tau(\tau_n^2 + \lambda_n^2) - r_o^2\tau_n\}\{2\lambda(\tau_n\dot{\tau}_n + \lambda_n\dot{\lambda}_n) - r_o^2\dot{\lambda}_n - 2r_o\lambda_n\dot{r}_o\}}{\{\tau(\tau_n^2 + \lambda_n^2) - r_o^2\lambda_n\}^2 + \{\lambda(\tau_n^2 + \lambda_n^2) - r_o^2\lambda_n\}^2}\right.$$

$$\left.\left. - \frac{\{\lambda(\tau_n^2 + \lambda_n^2) - r_o^2\lambda_n\}\{2\tau(\tau_n\dot{\tau}_n + \lambda_n\dot{\lambda}_n) - r_o^2\dot{\tau}_n - 2r_o\tau_n\dot{r}_o\}}{\{\tau(\tau_n^2 + \lambda_n^2) - r_o^2\tau_n\}^2 + \{\lambda(\tau_n^2 + \lambda_n^2) - r_o^2\lambda_n\}^2}\right]\right\} \tag{D.18}$$

The last term in (D.3) represents the expanding body radius

$$W(\sigma)\dot{r}_o = (V \cos \alpha) r_o \frac{dr_o}{dx} \ln(\tau + i\lambda) \tag{D.19}$$

Writing

$$\tau + i\lambda = \rho e^{i\gamma} \tag{D.20}$$

where

$$\ln(\tau + i\lambda) = \ln \rho + i\gamma \tag{D.21}$$

we get

$$\frac{d\phi_{\dot{r}_o}}{dt} = (V \cos \alpha)\ln \rho \left[\dot{r}_o \frac{dr_o}{dx} + r_o \frac{d}{dt}\left(\frac{dr_o}{dx}\right)\right] \tag{D.22}$$

It can be shown that each component of (D.4) given by (D.7), (D.9), (D.18), and (D.22) is finite at the body boundary, and all but (D.22) disappear as $\nu \to \infty$. Including (D.22) will not allow an absolute pressure coefficient on the body to be computed. The computed pressure distribution at any crossflow plane will be indeterminate by an additive constant factor. As done in reference 6, this factor can be computed

150

by comparing the predicted pressure distribution with a measured distribution and choosing a factor which produces good agreement between the curves.

An alternate approach to this difficulty is to choose a different singularity distribution to represent the growth of the body radius. A three-dimensional distribution of sources and sinks along the body axis to represent the body thickness distribution is described in reference 10. The procedure is to distribute sources and sinks along the body axis in such a manner that the body surface is a stream surface. This is carried out by matching body radius and slope at a large number of prescribed points.

Given such a distribution of sources, the velocity potential is

$$\phi(x) = \sum_{k=1}^{K} \frac{-Q_k}{4\pi\sqrt{(x - x_k)^2 + r^2}} \tag{D.23}$$

where

$$Q_k = 4\pi \ell^2 V \cos \alpha \, Q_n^* \tag{D.24}$$

ℓ = reference length

Q_n^* = dimensionless source strength

K = total number of singularities

$$\frac{d\phi(x)}{dt} = \frac{V \cos \alpha}{4\pi} \sum_{k=1}^{K} \frac{Q_k \left[(x - x_k) + r \frac{dr}{dx} \right]}{\left[(x - x_k)^2 + r^2 \right]^{3/2}} \tag{D.25}$$

It can be shown that

$$\lim_{r \to \infty} \frac{d\phi(x)}{dt} = 0 \tag{D.26}$$

and on the body surface,

$$\frac{d\phi(x)}{dt} = \frac{V \cos \alpha}{4\pi} \sum_{k=1}^{K} \frac{Q_k \left[(x - x_k) + r_o \frac{dr_o}{dx} \right]}{\left[(x - x_k)^2 + r_o^2 \right]^{3/2}} \tag{D.27}$$

151

Thus, replacing (D.22) with (D.27) provides a method of computing the absolute pressure coefficient on the body surface.

The complete unsteady term is the sum of (D.7), (D.9), (D.18), and (D.27). Since

$$t = \frac{x}{V \cos \alpha_c} \tag{D.28}$$

and

$$dt = \frac{dx}{V \cos \alpha_c} \tag{D.29}$$

we can write

$$\dot{r}_o = \frac{dr_o}{dx} \frac{dx}{dt} = V \cos \alpha_c \left(\frac{dr_o}{dx}\right) \tag{D.30}$$

and

$$\frac{d}{dt}\left(\frac{dr_o}{dx}\right) = \frac{d}{dx}\left(\frac{dr_o}{dx}\right)\frac{dx}{dt} = V \cos \alpha_c \left(\frac{d^2 r_o}{dx^2}\right)$$

Therefore, on the body surface

$$\frac{d\phi}{dt} = -V \sin \beta \left(\frac{2\tau}{r_o} V \cos \alpha_c \frac{dr_o}{dx}\right) + V \sin \alpha \left(\frac{2\lambda}{r_o} V \cos \alpha_c \frac{dr_o}{dx}\right)$$

$$+ \sum_{n=1}^{N} \frac{\Gamma_n}{2\pi V} V^2 \cos \alpha_c \left\{ -\left[\frac{(\tau - \tau_n)\frac{d\lambda_n}{dx} - (\lambda - \lambda_n)\frac{d\tau_n}{dx}}{(\tau - \tau_n)^2 + (\lambda - \lambda_n)^2}\right]\right.$$

$$-\left[\frac{\left(\tau r_n^2 - \tau_n r_o^2\right)\left(2\lambda\tau_n \frac{d\tau_n}{dx} + 2\lambda\lambda_n \frac{d\lambda_n}{dx} - r_o^2 \frac{d\lambda_n}{dx} - 2r_o\lambda_n \frac{dr_o}{dx}\right)}{\left(\tau r_n^2 - \tau_n r_o^2\right)^2 + \left(\lambda r_n^2 - \lambda_n r_o^2\right)^2}\right]$$

$$\left.-\frac{\left(\lambda r_n^2 - \lambda_n r_o^2\right)\left(2\tau\tau_n \frac{d\tau_n}{dx} + 2\tau\lambda_n \frac{d\lambda_n}{dx} - r_o^2 \frac{d\tau_n}{dx} - 2r_o\tau_n \frac{dr_o}{dx}\right)}{\left(\tau r_n^2 - \tau_n r_o^2\right)^2 + \left(\lambda r_n^2 - \lambda_n r_o^2\right)^2}\right]\right\}$$

$$+ V^2 \cos^2 \alpha \sum_{k=1}^{K} \frac{Q_k^* \left[(x - x_k) + r_o \dfrac{dr_o}{dx} \right]}{\left[(x - x_k)^2 + r_o^2 \right]^{3/2}} \qquad (D.32)$$

Finally, (D.32) can be simplified to

$$\frac{2}{V^2} \frac{d\phi}{dt} = - \frac{4\tau}{r_o} \sin \beta \cos \alpha_c \frac{dr_o}{dx} + \frac{4\lambda}{r_o} \sin \alpha \cos \alpha_c \frac{dr_o}{dx}$$

$$+ 2 \cos^2 \alpha_c \sum_{k=1}^{K} \frac{Q_k^* \left[(x - x_k) + r_o \dfrac{dr_o}{dx} \right]}{\left[(x - x_k)^2 + r_o^2 \right]^{3/2}}$$

$$+ 2 \cos \alpha_c \sum_{n=1}^{N} \frac{\Gamma_n}{2\pi V} \left\{ \text{----} \right\} \qquad (D.33)$$

and can be included in equation (38).

SYMBOLS

A_n, B_n	Fourier coefficients of transformation, equation (1)
c_n	normal force coefficient per unit length, equation (63)
c_y	sideforce coefficient per unit length, equation (67)
C_m	pitching moment coefficient, C_m = pitching moment/$qS_b d_{eq}$, positive nose up
C_n	yawing moment coefficient, C_n = yawing moment/$qS_b d_{eq}$, positive nose right
C_p	pressure coefficient, equation (37)
C_p'	modified pressure coefficient, equation (41)
C_N	normal force coefficient, C_N = normal force/qS_b, positive nose up
C_Y	side force coefficient, C_Y = side force/qS_b, positive nose to starboard
d	diameter
d_{eq}	diameter of circle having same area as base of model
F	separation parameter, equation (48)
F_D	diffusion term, equation (58)
ℓ_{ref}	reference length
L	total number of Fourier coefficients used to describe transformation, also model length
m_k	initial position of shed vortices, equation (54)
m_k'	initial image position of shed vortex, equation (55)
N	total number of shed vortices
p	local pressure
p_∞	free stream static pressure
q	free stream dynamic pressure, psf
Q	source strength
Q^*	dimensionless source strength
r	radial distance between two points
r_o	radius of circle

Re_d	free stream Reynolds number, based on d_{eq}
s	radial distance in σ-plane, equation (A.2)
S	reference area
S_b	base area
t	time
U	local velocity
V	free stream velocity
v,w	velocity components in real plane
v',w'	velocity components in circle plane
W	complex potential
x,y,z	body coordinate system with origin at the nose: x positive aft along the model axis, y positive to starboard, and z positive up
x_{c_p}	axial location of center of pressure
x_m	axial location of center of moments
α	angle of attack
α_c	angle between free stream velocity vector and body axis
β	angle of sideslip
γ	vorticity flux
Γ	vortex strength
δ^*	displacement thickness
Δt	time increment
Δx	axial length increment
θ	polar angle in ν-plane
ν	complex coordinate in circle plane, $\tau + i\lambda$ (figure 1), also kinematic viscosity
ν_e	effective kinematic viscosity
ξ	boundary layer run length along body surface
ρ	density

SYMBOLS (CONCLUDED)

σ complex coordinate in real plane, $y + iz$ (figure 11)

τ, λ lateral and vertical coordinates in crossflow plane of transformed body

ϕ velocity potential in circle plane, equation (5), also bank angle

Φ velocity potential in real plane, equation (8)

ψ stream function in circle plane, equation (5)

Ψ stream function in real plane, equation (8)

Subscripts

$(\dot{\ })$ derivative with time

$(\bar{\ })$ conjugate of complex quantity

$(\ )_v$ associated with a body vortex

DISTRIBUTION LIST

Office of Naval Research
800 N. Quincy Street
Arlington, VA 22217
   ONR-102IP   (6)
   ONR-211 (CDR P. R. Hite)   (6)
   ONR-430B (Mr. M. Cooper)   (1)

Defense Contract Administration
   Services Region San Francisco
866 Malcolm Road
Burlingame, CA 94010   (1)

Office of Naval Research Branch Office
1030 East Green St.
Pasadena, CA 91106   (1)

Naval Research Laboratory
Washington, D.C. 20375
   NRL-2627   (6)

Defense Documentation Center
Bldg 5, Cameron Station
Alexandria, VA 22314   (12)

U.S. Naval Postgraduate School
Monterey, CA 93940
   Code 57 (Dept of Aeronautics) (1)
   Library   (1)

Naval Weapons Center
China Lake, CA 93555
   NWC-3914 (Mr. W. H. Clark)   (1)

Naval Ship Research and Development
   Center
Bethesda, MD 20084
   NSRDC-16 (Dr. H. R. Chaplin) (1)
   NSRDC-522.3 (Library)   (1)

Air Force Flight Dynamics Laboratory
Wright Patterson AFB, Ohio 45433
   AFFDL/FGC (Mr. D. Bowser)   (1)
   AFFDL/FGC (Mr. E. Flinn)   (1)
   AFFDL/FGC (Mr. R. Woodcock) (1)
   AFFDL/ASD (Mr. R. Weissman) (1)
   AFFDL/FGL (Mr. P. Blatt)   (1)
   AFFDL/FXM (Mr. R. Jeffries) (1)
   AFFDL/FXM (Mr. R. Osborn)   (1)

Air Force Flight Test Center
Edwards AFB, CA 93523
   AFFTC/DOEEP (LCOL Jeglum)   (1)
   AFFTC/DOEEP (Mr. P. Sharp) (1)

Air Force Armament Laboratory
Eglin AFB, FL 32542
   AFAL/DLJC (LT J. Kincart)   (1)

Naval Material Command
Washington, D. C. 20362
   MAT-0331 (Mr. H. G. Moore)   (1)

Naval Air Test Center
NAS Patuxent River, MD 20670
   TPS (Mr. R. Bowes)   (1)
   SA-31 (LCDR Burgess)   (1)
   SA-43 (Mr. S. Porter)   (1)
   SA-60 (Mr. D. House)   (1)

Naval Air Systems Command
Washington, D. C. 20361
   NAIR-320D (Mr. R. F. Siewert) (1)
   NAIR-530A (Mr. H. Andrews)   (1)
   NAIR-53011 (Mr. R. C. A'Harrah) (1)
   NAIR-53011 (Mr. T. Lawrence) (1)

Naval Air Development Center
Warminster, PA 18974
   NADC-3015 (Mr. K. Mazza)   (1)
   NADC-3042 (Mr. A. Piranian) (1)

Naval Surface Weapons Center
White Oak Laboratory
Silver Spring, MD 20910
   WA-41 (Mr. W. J. Yanta)   (1)

U.S. Army Missile R&D Command
Redstone Arsenal, AL 35809
   DRDMI/TDK (Mr. D. J. Spring) (1)

Arnold Engineering Development Center
Arnold AFS, Tenn 37389
   Mr. R. Butler   (1)
   Mr. F. Langham   (1)
   Mr. T. Perkins   (1)
   Mr. A. Money   (1)

NASA Langley Research Center
Hampton, VA 23365
    MS 286 (Mr. R. Margasson)   (1)
    MS 287 (Dr. J. F. Campbell)   (1)
    MS 343 (Mr. J. Bowman)   (1)
    MS 355 (Mr. J. Chambers)   (1)
    MS 355 (Mr. W. Gilbert)   (1)
    MS 355 (Mr. E. Anglin)   (1)

NASA Ames Research Center
Moffett Field, CA 94035
    MS 227-8 (Mr. G. Chapman)   (1)
    MS 227-8 (Mr. G. Malcolm)   (1)
    MS 227-2 (Mr. T. Gregory)   (1)

NASA Dryden Flight Research Center
Edwards AFB, CA 93523
    Mr. P. Carr   (1)
    Mr. W. Dana   (1)
    Mr. E. Enevoldsen   (1)

Northrop Corporation
Aircraft Division
3901 W. Broadway
Hawthorne, CA 90250
    Attn: Mr. Gordon Hall   (1)

Northrop Corporation
Ventura Division
1550 Rancho CONEJO Blvd
Newport Park, CA 91320
    Attn: Dr. A. Wortman   (1)

General Dynamics
Fort Worth Division
P.O. Box 748
Fort Worth, TX 76101
    Attn: Mr. Charles Anderson
         (Zone 2833)   (1)

General Dynamics
Convair Division
P.O. Box 80847
San Diego, CA 92138
    Attn: Dr. E. Levinsky   (1)

McDonnell Aircraft
P.O. Box 516
St. Louis, MO 63166
    Dept 230 (Mr. R. W. McDonald) (1)
    Dept 241 (Mr. R. B. Jenny)   (1)

Boeing Aircraft
P.O. Box 3707
Seattle, Wash 98124
    Attn: Dr. P. Rubbert   (1)

V.P.I.
Engineering Science Dept
Blacksburg, VA 24061
    Attn: Dr. D. Mook   (1)